Mathematical Modelling of Metal Rolling

by

Mozhdeh Erfanian

Thesis

Submitted to the University of Warwick

for the degree of

Doctor of Philosophy

Mathematics of Real-World Systems CDT

May 2025

THE UNIVERSITY OF
WARWICK

Contents

List of Figures

List of Tables

Acknowledgments

The journey of completing this PhD has been shaped by the support, guidance, and encouragement of many wonderful people.

First and foremost, I would like to express my deepest gratitude to my supervisor, Dr Ed Brambley, for his unwavering support, insightful advice, constant encouragement, and patience throughout my PhD. Under his guidance, I have not only developed research skills and academic rigour, but I have also learned valuable etiquette, all of which will stay with me beyond my PhD. Working with him has been both inspiring and rewarding. I am also grateful to my second supervisor, Dr Sumit Hazra, for his helpful discussions, guidance, and continuous support.

I would also like to extend my appreciation to my collaborators, Dr Francis Flanagan, Dr Doireann O'Kiely, Dr Alison N. O'Connor, and Dr Carl Slater, whose help has played a crucial role in shaping my work.

I am grateful to the MathSys department and the Chancellor's International Scholarship for providing me with the opportunity to pursue my PhD at the University of Warwick.

Finally, I am deeply thankful to my family. To my parents, Mojgan and Kazem, and my sister, Bahareh—thank you for your unwavering belief in me, your encouragement, and your endless support. A special thanks to my husband, Amir, for his love, patience, and understanding, and for standing by my side through every challenge of the past few years. This journey would not have been possible without you.

Declarations

This thesis is submitted to the University of Warwick in support of my application for the degree of Doctor of Philosophy. It has been composed by myself and has not been submitted in any previous application for any degree.

List of publications including submitted papers:
A preliminary version of some of Chapter 3 was presented at the 2023 International Conference on the Technology of Plasticity in France (Erfanian, Brambley, Flanagan, O'Kiely, and O'Connor, 2023), and the majority of the work of this chapter has been submitted for publication in the European Journal of Mechanics - A/Solids (Erfanian, Brambley, Flanagan, O'Connor, and O'Kiely, 2025a).

A similar version of Chapter 5 is submitted for publication in the Journal of Materials Processing Technology after the viva (Erfanian, Slater, and Brambley, 2025c).

List of data provided by collaborators:
The results from the mathematical models in Chapters 2, 3, and 4 have been compared with finite element simulations conducted using the Abaqus software package. These simulations are performed by Dr Francis Flanagan from the University of Limerick, and an abridged version has been submitted for publication in the European Journal of Mechanics - A/Solids (Flanagan, O'Connor, Erfanian, Music, Brambley, and O'Kiely, 2024). Additionally, the results from the mathematical model presented in Chapter 5 have been compared with experimental data obtained by Dr Carl Slater at WMG labs, University of Warwick.

Abstract

This thesis presents a comprehensive study on the mathematical modelling of metal rolling processes. The development of robust, predictive models is critical for advancing industrial automation and control systems, thereby enhancing productivity, reducing material waste, and supporting the move toward sustainable, carbon-neutral manufacturing.

Drawing on the evolving theory of rolling, this work addresses the longstanding challenge of accurately resolving the complex deformation patterns inherent in rolling processes. Existing models often rely on simplified assumptions or single-length-scale approaches that fail to capture essential dynamics. By recreating the results of two simple asymptotic models, one of which is normally used for modelling sheet rolling, and by examining their limitations, it is demonstrated why a single-length scale fails to adequately capture the dynamics of the problem.

To overcome the limitations, an asymptotic model is developed that incorporates multiple scales, enabling the prediction of through-thickness effects. The model is initially formulated for rigid, perfectly plastic materials and later extended to account for material hardening. Validation against finite element simulations conducted using Abaqus demonstrates the model's accuracy and highlights the potential of analytical approaches to guide the development and validation of industrial FE simulations.

Building on the insights gained from sheet rolling, the framework is further extended to flat rolling of wire, illustrating the versatility of the approach.

Overall, the findings of this thesis not only enhance theoretical understanding of material deformation and flow during rolling but also provide a valuable tool for the design of advanced control algorithms in modern rolling mills.

Chapter 1

Introduction

Rolling is a process of manufacturing sheet metal in which two work rolls, rotating in opposite directions, draw the strip or plate into the roll gap and force it through to the exit (Lenard, 2013). This process causes a permanent reduction in the initial thickness and has been in use for centuries to produce flat products such as sheets and strips. A large proportion of all steel ($> 90\%$) and aluminium ($> 60\%$) products are rolled at some point during their manufacture (Allwood et al., 2012). With an annual global crude steel production of over 1,900 million tons in 2021 (World Steel Association et al., 2020), it is clear that even small process improvements, such as reductions in energy use or material waste, are of significant importance.

Studying the rolling process mathematically enhances the theoretical understanding of material deformation and flow, the knowledge of which is highly significant to industry as it provides the necessary data for advanced control algorithms. Automation driven by mathematical insights improves overall productivity and is a potential means of reducing material waste, and driving towards carbon neutrality and sustainability (Idzik et al., 2024). Modern set-up and control algorithms for rolling mills aspire to go beyond controlling only geometry, utilising models which, in addition to predicting how key quantities such as roll load and torque depend on the rolling parameters, also include microstructural modelling (Allwood et al., 2016).

Over the years, the theory of rolling has undergone significant development. Recent research has increasingly focused on examining the deformation inhomogeneity during rolling. However, a review of the relevant literature reveals that researchers studying the rolling process have offered differing perspectives, many of which lack solid theoretical or experimental support (Tarnovskii et al., 2013). As a result, creating fast and accurate rolling models with adequate through-thickness resolution remains an ongoing challenge.

Building upon this inspiration, the current work develops an asymptotic model capable of predicting inhomogeneous through-thickness shear effects, and results are validated against the commercial finite element (FE) package Abaqus. Chapter 2 regenerates the results of two simple asymptotic models, one of which is widely used for modelling sheet rolling, and by examining their limitations, demonstrates why a single-length scale fails to adequately capture the dynamics of the problem. A multiple-scales asymptotic model is developed in Chapter 3 and the results are validated against FE simulations. For the initial derivation, the material model in this chapter is considered to be rigid perfect-plastic, which is then modified in Chapter 4 to account for the hardening properties of metals. In Chapter 5, we introduce a mathematical model for the flat rolling of wire, building on the framework established in the sheet rolling model. Before delving into these topics, a general introduction to the rolling processes and their governing equations is provided in the rest of this chapter.

1.1 Sheet rolling process

The production of sheet metals involves several essential stages. It begins with the extraction of ores, which are then heated above their melting point (typically between 1,200 to 1,600°C) in the smelting process to produce liquefied metal. This molten metal is then poured into a rectangular mold in a process called casting. Once the metal cools and solidifies into an ingot, the surface impurities such as rust, scale, stains, and inorganic contaminants are removed in the pickling process through the application of a chemical mixture. The ingot is then sent through a rolling process where the thickness reduces by passing between two rolls separated by less than the current thickness. Sheet metal typically undergoes multiple rolling stages, each referred to as a “pass”. During each pass, the material is fed through at least one pair of rotating rolls, where it is simultaneously moved and deformed.

Rolling was first introduced to steel production in 1783 by Henry Cort in Titchfield, Hampshire, where he successfully refined earlier, more rudimentary attempts at using the technique. Cort’s rolling mill, which utilized grooved rollers, marked the beginning of continuous advancements in both the rolling process and mill design. Today, different types of mills are used to meet the specific requirements of various industries, from automotive to construction. Rolling mills can be classified by the number of rolls, the operating temperature, and the thickness and shape of the final product.

Rolling mills can feature a wide range of configurations. Two rollers with diameters that are relatively large are employed in the most simple two-roll configuration. Despite the simplicity, a major drawback is that the large diameters can cause rolls to bend which can lead to variations in the thickness of the workpiece. To ensure sufficient rigidity in the rolls and minimise span-wise deflection, two-roll configurations can be reinforced with backup rolls. This reinforcement can include a single set of backup rolls in a four-roll (four-high) configuration, two sets in a six-roll (six-high) configuration, or even more in cluster configurations (Figure 1.1). Smaller rolls with additional backup rolls offer the advantages of lower operating energy requirements and greater precision in maintaining strip dimension tolerances. Today, modern mills can feature up to five sets of 20-high close-coupled tandem rollers, where steel is rolled in a continuous process, passing from one set of rollers to the next, and also back again, until the desired shape is achieved (Lenard, 2013).

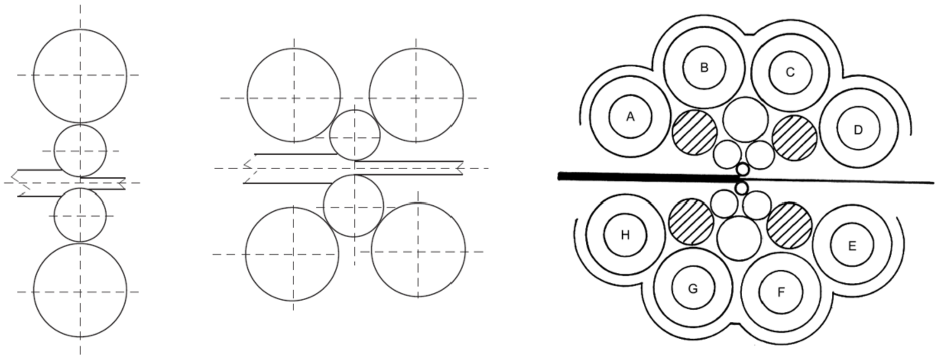

Four-high configuration Six-high configuration Cluster configuration

Figure 1.1: A diagram of different rolling configurations. Adapted from (Lenard, 2013).

The operating temperature of a rolling mill depends on the type of rolling process and the metal being processed. When the process is performed at a temperature below $0.5T_m$ (T_m is the melting point of the metal to be rolled), it is referred to as cold rolling, and above this temperature threshold, it is known as hot rolling (Figure 1.2). In addition to these definitions, there is also a process called warm rolling, which is not strictly defined but typically occurs at temperatures starting just below $0.5T_m$ and changes to hot rolling at some temperature above that (Lenard, 2013).

Hot rolling normally occurs during rough rolling; a process of reducing large workpieces, such as cast ingots, to an appropriate size for subsequent forming. Some finished products, such as thick-sheet metal, construction materials, vehicle frames, I-beams, and other items with simple cross-sections and rough surface finishes, are produced through hot rolling. The disadvantage of rolling at high temperatures is the development of a scale layer on the surface, which affects the quality of the resultant product and the process. Warm rolling is carried out for some grades of steel to tune metal strength and ductility. During warm rolling, some drawbacks of the hot rolling process are mitigated due to reduced scale formation. However, energy requirements increase, as the metal's resistance to deformation is higher in this temperature range (Lenard, 2013; Thakur et al., 2022).

In cold rolling, the metal undergoes additional processing to enhance its dimensional and mechanical properties. This process strengthens (or hardens) the metal by up to 20%, making it more suitable for high-stress applications. Parts and products made from cold-rolled steel typically feature a smooth and shiny surface free of rust and scale, while also maintaining tighter tolerances. Commonly cold-rolled products include metal furniture, computer hardware, metal drums and other thinner sheet metals. In this process, controlling dimensional consistency and surface quality is the primary objective. To ensure the product is commercially acceptable, strict tolerances for thickness and width must be maintained.

Figure 1.2: Hot rolling (TATA Steel, 2024) (top picture) and cold rolling (S Metals.co, 2024) (bottom picture).

1.1.1 Technical features

Before explaining the key dynamics of rolling, it is useful to introduce relevant terminology and geometry. A simplified 2D schematic of rolling with a pair of rollers is shown in Figure 1.3. The region in which the sheet is in contact with the rolls is referred to as the roll gap. In mathematical models, the length of the roll gap is calculated from the point where the leading end of the workpiece leaves the narrowest gap of the rolls. In reality, however, the workpiece remains in contact with the roll surface for a certain distance downstream after the narrowest section (Liu et al., 1985). This is due to elastic recovery and possibly some "post-deformation" plastic strain and has not been included in the current study as it requires including the unloading procedure and elasticity in the rolling analysis.

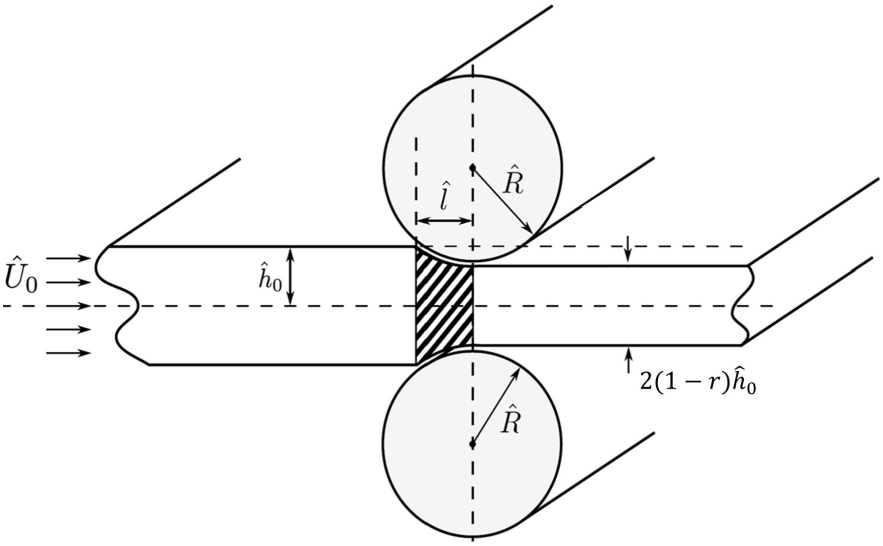

Figure 1.3: A diagram of rolling illustrates the relevant parameters of two-dimensional geometry. Adapted from Minton (2017).

The sheet has an initial thickness $2h_0$ and the reduction r reduces this thickness by rh_0 top and bottom, giving a final thickness of $2(1-r)h_0$. As the strip enters the roll gap, its surface velocity is initially lower than that of the roll. The friction force opposes the direction of relative motion, assisting the strip's movement as it enters. As compression continues, the strip's velocity increases until it matches the roll's surface velocity. At this point/region, known as the "neutral" or no-slip point/region, the strip and roll move together at the same speed, eliminating their relative velocity. If the neutral point lies between the entry and exit, the strip continues to compress beyond it, causing its surface velocity to exceed that of the roll. After the neutral point, up to the exit, friction shifts direction, now resisting the strip's motion. The area between the entry and the neutral point is commonly known as the entrance region or the region of backward slip, and the region between the neutral point and the exit is referred to as the exit region or the region of forward slip (Lenard, 2013).

Depending on the reduction ratio and sheet thickness, the deformation in the roll gap (including the area after the narrowest roll separation) can be elastic, plastic, or contained plastic. The elastic entrance and exit regions are the characteristics of the rolling process and can be seen in all rolling regimes. In the rolling of sheets with moderate thicknesses, plastic deformation is developed in most of the deformation zone. In this case, the change in frictional force causes the material to be squeezed toward the neutral point, creating a pressure peak with a pressure profile known as "pressure hill" (see graph (a) in pressure plot in Figure 1.4). This phenomenon has been consistently observed in experiments and validated by all rolling models in the literature.

The extended no-slip zone in foil rolling creates two distinct regions. Within this zone, the strip's thickness remains nearly uniform, and the contact pressure adapts the semi-elliptical Hertz pressure distribution (Fleck et al., 1992), flattening part of the elastic cylindrical roll. If the pressure increases steadily through the no-slip zone, the material yields, while any plastic strain in the strip is limited to an elastic order of magnitude. This phenomenon is known as contained plasticity (see the rising section in pressure with a negative gradient in graphs (b) and (c) in Figure 1.4). Conversely, a decreasing pressure in the no-slip zone leads to elastic unloading (see the fall in pressure in graph (c)). In this case, a sharp pressure peak that occurs just beyond the end of the neutral zone is explained to be associated with the rather sharp re-entrant corner in the roll deformation at the onset of plastic reduction at the exit (Fleck et al., 1992).

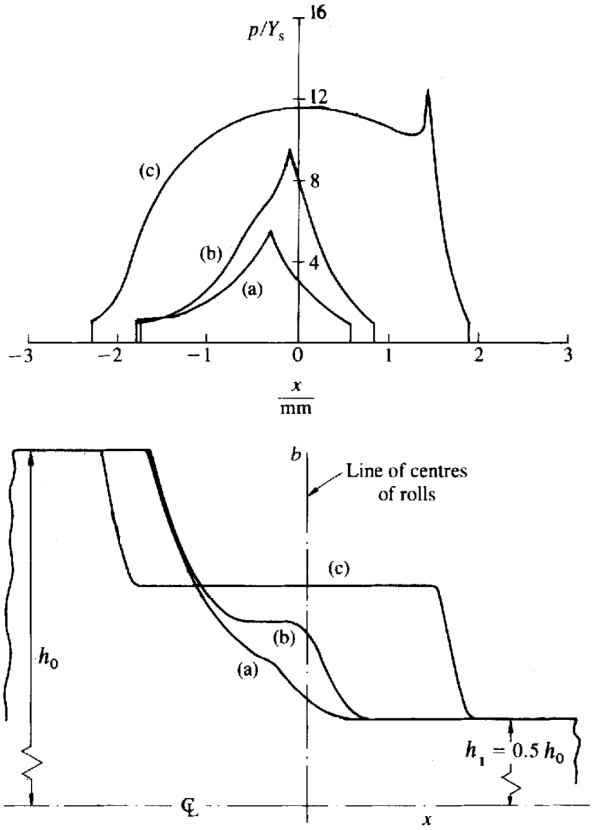

Figure 1.4: Effect of strip thickness upon pressure distribution and deformed shape of the strip (Fleck et al., 1992). (a) $h_0 = 0.03\,\text{mm}$, (b) $h_0 = 0.024\,\text{mm}$, (c) $h_0 = 0.01\,\text{mm}$. Top figure: pressure. Bottom figure: thickness.

In industrial rolling operations, front and back tensions are applied as an impact of both the preceding and subsequent mill stands, as well as the influence of loopers—devices positioned between mill stands that maintain tensile forces in the strips. These forces affect both the magnitude of roll separating forces and roll torques. In a laboratory setting, the common practice is to gently push the strip, placed on the delivery table, towards the work rolls and rely on friction forces to guide its entry.

With this introduction to the rolling process, the following sections summarise the fundamental knowledge required for modelling the process.

1.2 Plasticity

1.2.1 Stress state

Plasticity, or plastic deformation, is the capacity of a solid material to undergo a permanent change in shape when subjected to external forces. For instance, when a metal piece is bent or hammered into a new shape, it exhibits plasticity, as the material undergoes irreversible changes. In engineering, the transition from elastic to plastic behaviour is called yielding.

The so-called strain-stress curve (Figure 1.5) is a widely used reference graph for metals in material science and manufacturing. This curve is found experimentally in a lab by subjecting a rod of the test piece to the axial tension test. The metal begins to yield when the axial stress reaches the yield stress Y. If the applied stress is below Y, the material exhibits elastic behaviour, potentially nonlinear, and returns to its original shape once the load is removed. However, if the applied stress exceeds Y and is then removed, a residual permanent strain remains in the material. The metal is said to be undergoing work hardening (the part of the loading curve in Figure 1.5 above the dotted line), which means the metal becomes more difficult to deform and increasing stress is required to produce additional plastic deformation.

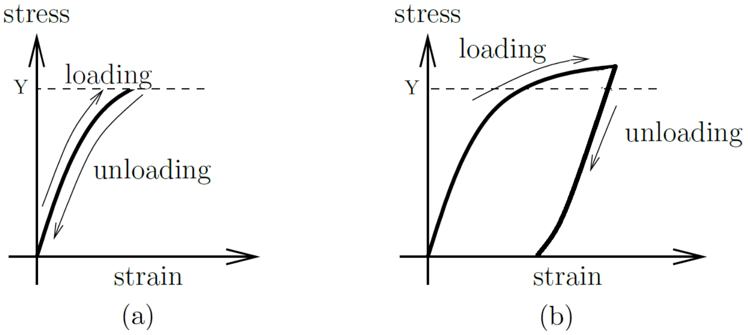

Figure 1.5: A typical stress-strain curve: (a) below the yield stress Y (Howell et al., 2008); (b) when the yield stress is exceeded.

In perfect plasticity, the stress is restricted from exceeding the yielding point, meaning the material can only exist in two distinct states. Below the yield stress, it acts as an elastic solid, but at and beyond the yield point, it transitions into a plastic state (Figure 1.6(a)). In many practical problems with large plastic deformation, the elastic component of strain is often disregarded due to mathematical complexities. As a result, the material is treated as rigid when stressed below the yield point, with an infinitely large elastic modulus. This theoretical material is known as a rigid plastic material, as opposed to an elastic plastic material (Figure 1.6(b)). According to Hill (1948, page 128) “in many technological forming processes (e.g. rolling, drawing, forging) experience shows that the assumption of a plastic-rigid material does not lead to any significant errors”.

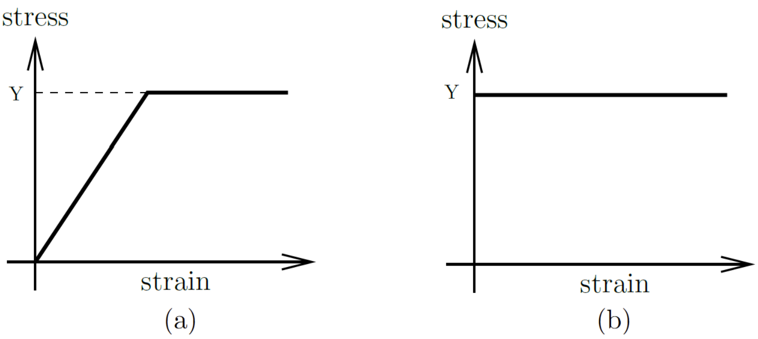

Figure 1.6: Simplified stress-strain relationship for a plastic material: (a) elastic perfectly plastic behaviour (Howell et al., 2008); (b) rigid perfectly plastic behaviour.

In general, for elastic and plastic deformations, an inequality of the following form is imposed:

$$f(\sigma_{ij}) \leq Y, \tag{1.1}$$

where f is the yield function. In 1.1, equality represents the plastic state, while the less-than sign corresponds to elastic deformation. If the metal is assumed to be isotropic, then f depends only on the magnitudes of the three principal applied stresses but not on their directions. This follows that f can be written as a function of the three stress invariants, J_1, J_2 and J_3 where

$$\begin{aligned} J_1 &= \sigma_1 + \sigma_2 + \sigma_3, \\ J_2 &= -(\sigma_1\sigma_2 + \sigma_2\sigma_3 + \sigma_3\sigma_1), \\ J_3 &= \sigma_1\sigma_2\sigma_3, \end{aligned} \tag{1.2}$$

written in terms of principle stresses (eigenvalues of stress tensor), σ_1, σ_2 and σ_3. It is important to note that only functions that are symmetrical in the three principal stresses can serve as a valid yield criterion, rather than any arbitrary function of the principal stresses. From experiments, it is widely accepted that the yielding of a metal is unaffected by moderate hydrostatic pressure or tension. Assuming this holds true for an ideal plastic body, it follows that yielding is dependent only on the principal components of the deviatoric stress tensor, defined as,

$$s_{ij} = \sigma_{ij} - p\delta_{ij}, \tag{1.3}$$

where $p = \sigma_{kk}/3 = J_1/3$ is the hydrostatic component of stress. The yield criterion now reduces to the form

$$f(J_2', J_3') = Y, \tag{1.4}$$

where,

$$\begin{aligned} J_2' &= -(s_1s_2 + s_2s_3 + s_3s_1), \\ J_3' &= s_1s_2s_3. \end{aligned} \tag{1.5}$$

von Mises suggested that yielding occurred when $\sqrt{3J_2'}$ reached a critical value, or, in other words, that the function f in equation (1.5) did not depend on J_3'. It can be shown that this is equivalent to,

$$\frac{1}{2}\left[(\sigma_1-\sigma_2)^2+(\sigma_2-\sigma_3)^2+(\sigma_3-\sigma_1)^2\right]=Y^2, \tag{1.6}$$

where the left-hand side of equation (1.6) is equivalent to $3J_2'$. This equation may be written in terms of σ_{ij} as

$$\frac{1}{2}\left[(\sigma_{xx}-\sigma_{yy})^2+(\sigma_{yy}-\sigma_{zz})^2+(\sigma_{zz}-\sigma_{xx})^2+6(\sigma_{xy}^2+\sigma_{yz}^2+\sigma_{zx}^2)\right]=Y^2. \tag{1.7}$$

From this equation, it is evident that Y denotes the critical value or yield strength under uniaxial loading (where only σ_{xx} is nonzero), corresponding to the value observed in the stress-strain curve in Figure 1.5. A different but frequently encountered loading condition is “pure shear”, characterised by $\sigma_{xy}=\kappa$ while all other stress components are zero. In such a case, the yield strength in pure shear is κ, and from the von Mises equation (1.7) it can be seen that

$$\kappa=\frac{Y}{\sqrt{3}}, \tag{1.8}$$

where highlights that material typically yields under lower stresses in shear compared to uniaxial tension. This equality has been shown to align well with experimental results for steels. However, for aluminium, the relation $\kappa=Y/2$ appears to offer a better fit, suggesting that the Tresca yield criterion expressed as, $|\sigma_{\max}-\sigma_{\min}|=Y$, might be a more suitable alternative for aluminium. Here, $\sigma_{\max}$ and $\sigma_{\min}$ refer to maximum and minimum principal stresses, respectively, considering the sign. von Mises and Tresca yield stress are shown in Figure 1.7.

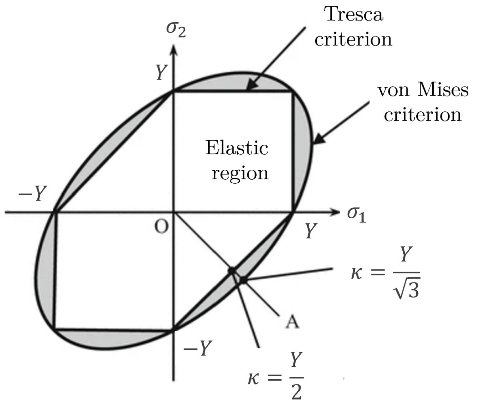

Figure 1.7: A diagram of von Mises and Tresca yield functions in $\sigma_1-\sigma_2$ plane with $\sigma_3=0$.

Two common stress conditions in materials under external forces are “plane stress” and “plane strain”. In these scenarios, either stress or strain in one direction is assumed negligible, effectively transforming three-dimensional problems into simplified two-dimensional ones. This simplification not only reduces the complexity of model construction but also significantly lowers computational costs.

Plane strain

A state of plane strain is defined by the properties (i) that the flow is everywhere parallel to a given plane, say the (x, y) plane, and (ii) that the motion is independent of z (Hill, 1998). We are then dealing with a two-dimensional system, in which the non-vanishing velocity components are v_x, and v_y, and the stress normal to the planes of flow is equal $\sigma_{zz} = (\sigma_{xx} + \sigma_{yy})/2$. von Mises equation (1.7) for plane-stress is simplified to

$$\frac{1}{4}(\sigma_{xx} - \sigma_{yy})^2 + \sigma_{xy}^2 = \kappa^2. \tag{1.9}$$

Plane strain condition can be realised in a specimen confined between (effectively) rigid blocks with faces parallel to the planes of flow. In technological processes, if the percentage lateral spread is small in comparison with the percentage reduction in thickness (width-to-thickness ratio > 10 (Lenard, 2013), such as in rolling of a wide sheet), the sheet is deformed under approximately plane strain condition.

Plane stress

In continuum mechanics, a material is considered to be under plane stress loading when the stress vector across a particular plane is zero. This assumption is commonly applied to thin flat plates subjected to in-plane loading forces, where stresses perpendicular to the plate are negligible compared to the in-plane stresses. Similar to the case of plane strain, this simplification significantly reduces the complexity of stress analysis, allowing the stress state to be represented by a 2×2 matrix instead of a 3×3 matrix. If thickness in z-direction is much smaller than the in-plane dimensions (x- and y-directions), the equation (1.7) is simplified to

$$\frac{1}{3}\left(\sigma_{xx}^2 + \sigma_{yy}^2 - \sigma_{xx}\sigma_{yy}\right) + \sigma_{xy}^2 = \kappa^2. \tag{1.10}$$

1.2.2 Inertia and force balance

In the Eulerian form, the Cauchy momentum equation is written as

$$\rho\left(\frac{\partial \boldsymbol{v}}{\partial t} + (\boldsymbol{v} \cdot \boldsymbol{\nabla})\boldsymbol{v}\right) = \boldsymbol{\nabla} \cdot \boldsymbol{\sigma} + \rho \mathbf{b}, \tag{1.11}$$

where ρ is the density at a given point of the continuum and $\boldsymbol{v}$ and $\boldsymbol{b}$ are the flow velocity and body force vector field, respectively. In plasticity, the term “flow” is commonly used to describe the permanent deformation that occurs at the yield stress. It is typically assumed that the flow is slow enough for the inertia of the particles to be negligible compared to the frictional forces between them. This assumption is generally valid in practice and permits the neglect of the acceleration terms in Cauchy's momentum equation, simplifying equation (1.11) to

$$\frac{\partial \sigma_{ij}}{\partial x_j} = 0. \tag{1.12}$$

Therefore in 2D, yield criterion (1.9) (or (1.10) in plane-stress) and force balance (1.12) in both directions, give three equations sufficient for solving the three stress components σ_{xx}, σ_{yy} and σ_{xy}.

1.2.3 Rigid plastic stress-strain relationship

In plasticity, it is helpful to express mathematical models in terms of the velocity of the medium rather than displacement. The velocity vector $\boldsymbol{v}(\boldsymbol{x}, t)$ is introduced as

$$\boldsymbol{v} = \frac{\mathrm{D}\boldsymbol{u}}{\mathrm{D}t} = \frac{\partial \boldsymbol{u}}{\partial t} + (\boldsymbol{v} \cdot \boldsymbol{\nabla})\boldsymbol{u}, \tag{1.13}$$

using the Eulerian frame, where $\boldsymbol{u}$ is the displacement vector. If the displacement gradient is small, $\boldsymbol{v}$ may simply be approximated as the Eulerian time derivative of $\boldsymbol{u}$. While this assumption is typically appropriate for small displacements in elastic materials, plastic behaviour is defined by the ability to experience significant permanent displacements without failure. Consequently, it is essential to retain the nonlinear terms in (1.13) and to make a clear distinction between Lagrangian and Eulerian time derivatives (Howell et al., 2008).

The deformation of a flowing material is described using the concept of the rate-of-strain, which quantifies how the material's shape changes over time under the influence of stress. The rate-of-strain tensor is defined by

$$\dot{\varepsilon}_{ij} = \frac{1}{2}\left(\frac{\partial v_i}{\partial x_j} + \frac{\partial v_j}{\partial x_i}\right). \tag{1.14}$$

With all the necessary prerequisites established, we can finally formulate a constitutive relation for the stress $\boldsymbol{\sigma}$ associated with a given velocity $\boldsymbol{v}$. The net mechanical energy, i.e. the sum of the kinetic and strain energies, is conserved in a linear elastic and non-linear hyperelastic material. However, irreversible plastic flow involves a loss of mechanical energy, which is dissipated as heat. This dissipation reflects the rate at which mechanical energy is converted into heat during the process (Howell et al., 2008). The dissipation function is defined by

$$\Phi = \dot{\varepsilon}_{ij}\sigma_{ij}. \tag{1.15}$$

If we assume that the material flows in such a way as to “maximise” the rate at which it dissipates energy, then we wish to solve (Howell et al., 2008),

$$\begin{aligned} &\text{maximise} \quad \Phi \\ &\text{subject to} \quad f(\sigma_{ij}) = \kappa. \end{aligned} \tag{1.16}$$

The solution to this optimisation problem is

$$\dot{\varepsilon}_{ij} = \lambda \frac{\partial f}{\partial \sigma_{ij}}\,, \tag{1.17}$$

where λ is a plastic multiplier (Howell et al., 2008). Equation (1.17) represents the “flow rule” associated with the yield function f (called the associated flow rule). The associated flow rule typically aligns well with experimental observations and ensures that the flow exhibits the same symmetry properties as the yield function. A geometrical interpretation of (1.17) is that the rate-of-strain is perpendicular to the yield surface. It should be pointed out that in general, it is not necessary for the dissipation to be maximised for loading, and it only needs to be positive. Indeed, there are several alternative non-associated flow rules which are not derived from the yield function (Howell et al., 2008).

From any yield criterion, it can be seen that,

$$\frac{\partial f}{\partial \sigma_{kk}} = 0, \tag{1.18}$$

which also implies that the yield criterion is insensitive to isotropic stress (Howell et al., 2008). Equation (1.17) then implies that

$$\dot{\varepsilon}_{kk} = 0, \tag{1.19}$$

thus ensures that the flow is incompressible. This is consistent with experimental evidence, which shows that plastic deformation does not significantly change the density of a metal (Howell et al., 2008).

In summary, therefore in 2D, the force balance equation (1.12), the yield condition (1.7) and the flow rule (1.17) together constitute ten scalar equations, forming a closed system for σ_{ij}, v_i and λ (Howell et al., 2008).

1.2.4 Hardening

Hardening is the process of strengthening the material in response to a range of factors. When hardening occurs, increasing stress is required to produce additional plastic deformation, and metal becomes stronger and more difficult to deform. One hardening mechanism is hardening beyond the yield point (the part of the loading curve in Figure 1.5 above the dotted line) called work/strain hardening.

The hardening law governs the variation of material strength. The change in the material strength can also be envisaged as a change in the geometry and/or the location of the yield surface as a function of effective plastic strain. We may write

$$f\left(\sigma_{ij}\right) = H\left(\int \dot{\varepsilon}_{\mathrm{eq}}\right), \tag{1.20}$$

where f is the yield function, H is the hardening law and the integral is taken over the actual strain-path from some initial state of metal. The effective equivalent plastic strain $\varepsilon_{\mathrm{eq}}$ which controls the hardening, can be defined as the accumulated plastic strain according to the state of stress,

$$\dot{\varepsilon}_{\mathrm{eq}} = \sqrt{\frac{2}{3}\dot{\varepsilon}_{ij}\dot{\varepsilon}_{ij}}\,, \tag{1.21}$$

where the dot is the time differentiation. Similarly, $\varepsilon_{\mathrm{eq}}$ can also be described using the plastic work per unit volume

$$\dot{W}_{\mathrm{p}} = \dot{\varepsilon}_{\mathrm{eq}}\sigma_{\mathrm{eq}} = \dot{\varepsilon}_{ij}s_{ij}\,, \tag{1.22}$$

where σ_{eq} is the effective stress defined based on the loading surface. For von Mises yield creation

$$\sigma_{\mathrm{eq}} = \sqrt{3j_2'} \qquad \Rightarrow \qquad \sigma_{\mathrm{eq}} = \sqrt{\frac{3}{2}s_{ij}s_{ij}}\,. \tag{1.23}$$

The evolved yield surface is commonly called the loading surface. The evolution of the loading surface may follow a combination of isotropic and kinematic hardening rules to capture both loading surface expansion and translation. In isotropic hardening, the yield surface expands uniformly in all directions with the plastic flow (Figure 1.8(a)).

In the case of monotonically increasing loading, it is often reasonable to assume that any hardening that occurs is isotropic, however, this is often not appropriate for the case of reversed loading. If after plastic deformation the loading is reversed so that the material deforms elastically, the experimental observations show that the elastic region is significantly reduced compared to the previous loading (compare the height of load point (1) with point (2) in Figure 1.8(b)). Consequently, the material undergoes plastic deformation under much smaller forces. This behaviour is known as kinematic hardening, where the centre of the yield surface moves but its surface does not expand. This is shown in Figure 1.8(b).

In the previous loading case, if elastic deformation continues and material deforms plastically until the next force reversal at point D (Figure 1.8(c)) and subsequently reloaded in the opposite direction, the resulting stress–strain loop, BCDB, is referred to as a hysteresis loop. If, in addition to the kinematic hardening, the material also

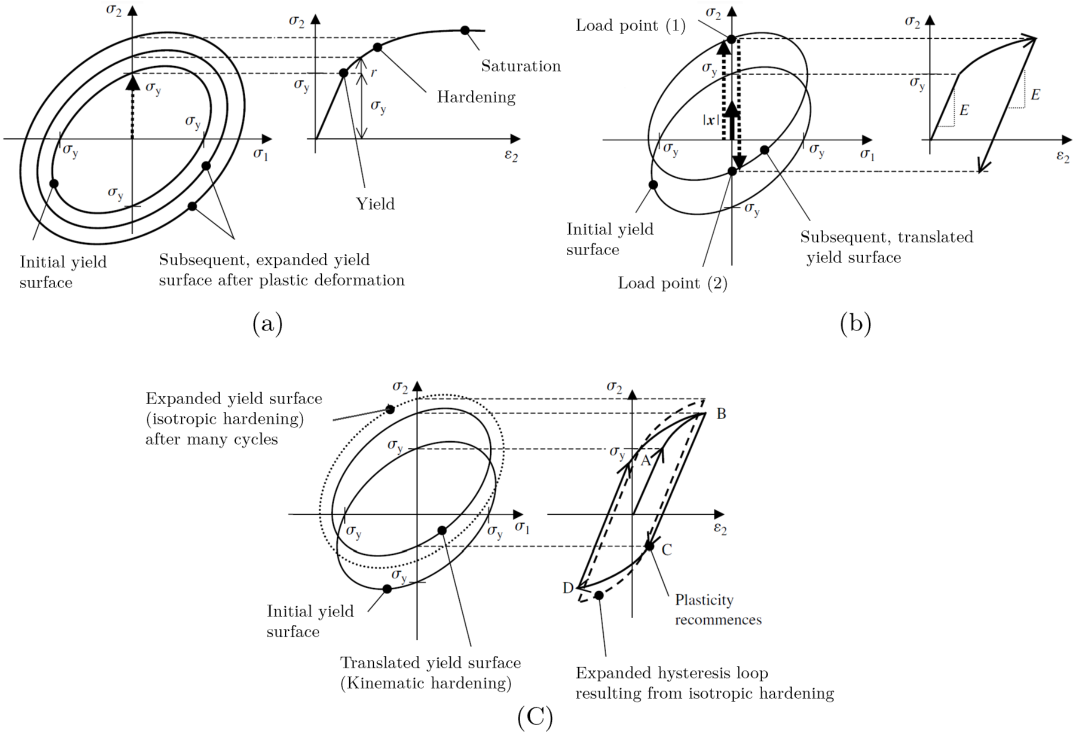

Figure 1.8: A diagram of different hardening rules (Dunne and Petrinic, 2005): (a) isotropic hardening; (b) kinematic hardening; (c) combined kinematic and isotropic hardening.

isotropically hardens, then along with the translation of the yield surface, there is a gradual expansion of the surface. This is illustrated by the broken line hysteresis loop in Figure 1.8(c). This process, in which the peak stress and strain in a hysteresis loop increase due to isotropic hardening, is often called cyclic hardening, as it typically takes place from cycle to cycle over multiple cycles. Kinematic hardening, in contrast, occurs within each individual cycle (Dunne and Petrinic, 2005).

1.3 Friction boundary condition

With the full set of governing equations established, the next step is to define the boundary conditions to close the system. Normal forces are governed by a no-penetration condition, while traction forces are more complex and remain an active area of research in tribology and related fields. Various traction models have been developed with different levels of complexity, particularly for high-temperature and lubricated conditions.

Coulomb friction is widely applied to the slipping regime in rolling problems and assumes that the friction force is proportional to the normal pressure,

$$\boldsymbol{\tau} = -\mu \boldsymbol{\sigma}_n \frac{\Delta \boldsymbol{v}}{|\Delta \boldsymbol{v}|} \qquad \text{for} \qquad |\Delta \boldsymbol{v}| \neq 0. \tag{1.24}$$

Here, $\boldsymbol{\tau}$ represents the tangential surface traction, μ is the dimensionless friction coefficient, $\boldsymbol{\sigma}_n$ is the normal stress to the contact surface, and $\Delta\boldsymbol{v}$ is the relative-slip velocity vector of the two moving bodies across the surface. If the contact loads are high, which is the case in bulk-forming processes, the slipping threshold is assumed to be fixed (Beyer et al., 2015). In such a case, Tresca's friction law is an alternative to Coulomb law, in which friction stress is expressed in dependency on the shear yield stress,

$$\boldsymbol{\tau} = -m\kappa\frac{\Delta\boldsymbol{v}}{|\Delta\boldsymbol{v}|} \qquad \text{for} \qquad |\Delta\boldsymbol{v}| \neq 0, \tag{1.25}$$

where m is the Tresca's friction coefficient.

In the initial layout calculations for a strip rolling mill, it is common to assume that the friction coefficient between the work roll and the strip remains constant. In general, factors such as temperature, strip and work roll roughness, work roll diameter, reduction, and lubricant viscosity influence the friction coefficient, leading to friction inhomogeneities both over time and across the surface during the rolling process (Lenard, 2013).

A distinctive aspect of the rolling problem is the presence of a point (or region) along the roll-workpiece interface where the relative velocity of the deforming material with respect to the roll becomes zero. The position of this point (or region) is influenced by the magnitude of the frictional stress itself. In this case, rather than providing an estimate of the actual frictional force, the Coulomb law provides a threshold value for this force, above which motion would commence;

$$\boldsymbol{\tau} < \mu\boldsymbol{\sigma}_n \qquad \text{for} \qquad |\Delta\boldsymbol{v}| = 0. \tag{1.26}$$

Some approximations smoothen the Coulomb friction law by assuming that the coefficient of friction is a highly nonlinear function of the relative velocity (Wojtyra, 2017). As a consequence, equation (1.24) takes the form

$$\boldsymbol{\tau} = \mu(\Delta\boldsymbol{v})\boldsymbol{\sigma}_n. \tag{1.27}$$

For instance, using a hyperbolic tangent function,

$$\boldsymbol{\tau} = \mu \tanh\left(\Delta\boldsymbol{v}\right)\boldsymbol{\sigma}_n. \tag{1.28}$$

Different functions of the slipping velocity are used; for example, hyperbolic tangent, arctangent or trigonometric functions, with all predicting zero friction force at zero relative velocity.

Various alternative models have been proposed that treat friction as an internal state-dependent process rather than an instantaneous function of velocity. These models capture stick-slip motion by incorporating the internal dynamics of surface interactions.

However, they require the specification of multiple parameters and are often highly sensitive to them, making their implementation challenging (Pennestrì et al., 2016). An alternative approach is to define the boundary condition by enforcing equal velocities at the interface instead of specifying surface forces. However, this method leaves the stress distribution indeterminate (Minton, 2017).

1.4 Modelling approaches in rolling

Simulation models play a critical role in the design and optimisation of flat rolling processes. These models can be broadly categorised based on their computational time and complexity. The first category includes detailed and computationally intensive models that deliver high accuracy. FE simulations are widely regarded as the "gold standard" for analysing rolling processes (Trzepiecinski and Lemu, 2017; Prabhu et al., 2020; Kumar et al., 2021). However, the significant computational time limits their feasibility for real-time applications. Models from the second category are often based on equations drawn from physical principles, with some simplifying assumptions that enable analytical or semi-analytical solutions. Mathematical models, when sufficiently accurate, not only deepen the theoretical understanding of the process but also offer fast computational solutions suitable for integration into control algorithms. This section reviews various techniques employed to develop fast models.

1.4.1 Slab method

In the slab model, a sheet in the rolling process is represented as a series of vertical slabs undergoing homogeneous through-thickness compression. Combined with the assumption of plane-strain plastic flow, this reduces the problem to a single independent variable: the distance along the rolling direction, x, or the angular position from the exit, ϕ (see Figure 1.9). Consequently, the static force equilibrium within a slab results in an ordinary differential equation (ODE), which is far simpler to solve than the partial differential equation (PDE) that would otherwise arise (Lenard, 2013).

The equilibrium of the forces exerted upon a thin vertical segment situated between x and $x + \mathrm{d}x$ leads to

$$\frac{\mathrm{d}(h\sigma_{xx})}{\mathrm{d}x}\mathrm{d}x + p_r\frac{\mathrm{d}x}{\cos(\phi)}\sin(\phi) \mp \mu p_r\frac{\mathrm{d}x}{\cos(\phi)}\cos(\phi) = 0, \tag{1.29}$$

where σ_{xx} is the resulting horizontal stress due to the roll pressure, p_r, and the frictional drag, $\tau = \mu p_r$ (note the subscript r to differentiate the hydrostatic pressure from the roll pressure). The negative sign in $\mp$ describes the conditions of equilibrium between the neutral point and the entry and the positive sign is for between the neutral point

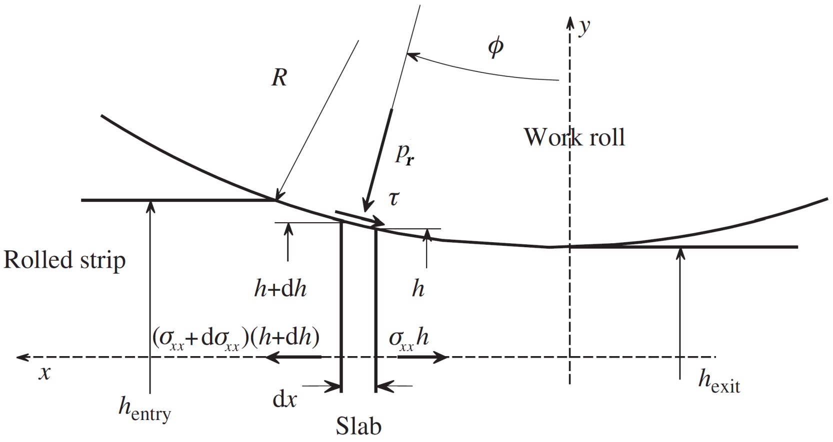

Figure 1.9: A diagram of the rolled strip and the roll, showing the forces acting on a slab of the deforming material before the neutral point. Adapted from Lenard (2013)

and the exit. The force balance in y direction results in

$$\sigma_{yy} = -p_r(-1 \mp \mu \tan(\phi)). \tag{1.30}$$

The additional necessary independent equation is the yielding criterion. Using Tresca criterion, we get,

$$\sigma_{xx} - \sigma_{yy} = 2\kappa. \tag{1.31}$$

Substituting equation (1.30) and (1.31) into equation (1.29) we obtain,

$$-\frac{\mathrm{d}}{\mathrm{d}x}[hp_r\ (-1 \mp \mu \tan(\phi)) - 2\kappa h] + p_r\ \tan(\phi) \mp \mu p_r = 0, \tag{1.32}$$

where $x = R\sin(\phi)$. By neglecting $\mu \tan\phi$ term, and setting, $\tan\phi = -\mathrm{d}h/\mathrm{d}x$, we get

$$h\frac{\mathrm{d}p_r}{\mathrm{d}x} \mp \mu p_r + 2\kappa\frac{\mathrm{d}h}{\mathrm{d}x} = 0. \tag{1.33}$$

Equation (1.33) is the equilibrium equation for roll pressure, p_r. Using the appropriate boundary conditions at the entrance and the $-$ve sign of $\mp$, integration leads to a curve for the roll pressure starting at the entrance. A different solution is derived by integrating from the exit, using an appropriate boundary condition, and now the $+$ sign. Two solutions thus produced give the pressure hill exerted by the rolled strip on the roll, with the location of the intersection of the two curves defining the neutral point, as illustrated schematically in Figure 1.10.

In equation (1.29), by treating σ_{xx} only as a function of ϕ (or equivalently x), the assumption of homogeneous compression is imposed. In reality, σ_{xx} varies from the surface of the slab to its interior, meaning this equation is not suitable for determining the through-thickness stress distribution. Orowan (1943) generalised the thin vertical segment of the rolled stock, considered a wedge element forming from two straight lines

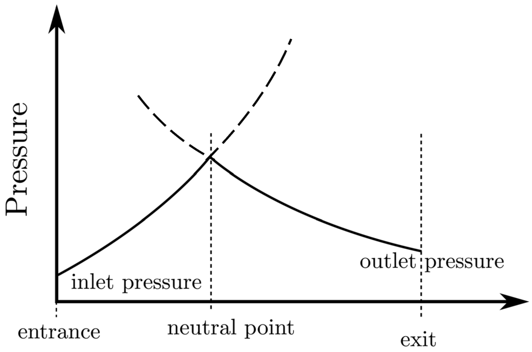

Figure 1.10: A diagram of the pressure hill profile with defined inlet and outlet pressure; the location of the intersection of the two curves defines the neutral point. Adapted from Minton (2017)

parallel to the roll axes whose angular coordinates are ϕ. He used the Hencky-Prandtl theorem to calculate the variation of stress within a cross-section of the rolled stock, and in this way developed a modified version of the equation where p_r varies with ϕ but also through thickness.

Some works since then extended Orowan's original work or simplified the calculation process with additional assumptions. Sims (1954) leveraged the small angles present in the roll gap and made the assumption that the product of the shear stress and the angular variable is negligible compared to other factors. He also used the Tresca friction law at the contact between the roll and strip. These assumptions simplified the problem, allowing for a closed-form solution to the equilibrium equation.

In addition to the small angle assumption, Bland and Ford (1948) assumed that the roll pressure equals the stress in the vertical direction. As with the model of Sims (1954), this allowed a closed-form solution to be obtained. The model of Bland and Ford (1948) is often used in the rolling industry in the analysis and control of the cold rolling process.

1.4.2 Slip-line fields

Slip-line theory offers a solution for plane strain boundary value problems by simplifying the governing equations for rigid-perfectly plastic solids, assuming quasi-static loading and no temperature variations. In the state of pure shear, the stress tensor is

$$\begin{bmatrix} -p & \kappa \\ \kappa & -p \end{bmatrix}. \tag{1.34}$$

The terms σ_{xx}, σ_{yy} and σ_{xy} can be written in terms of hydrostatic pressure and angle with respect to maximum shear. Under rotation of the coordinate system by θ degrees from the positive x-axis in the anticlockwise direction, the stress state σ may be rewritten as

$$\begin{bmatrix} -p-\kappa\sin(2\theta) & \kappa\cos(2\theta) \\ \kappa\cos(2\theta) & -p+\kappa\sin(2\theta) \end{bmatrix}. \tag{1.35}$$

Substituting these expressions into the equilibrium equations (1.12) leads to

$$-\frac{\partial p}{\partial x} - 2k\cos(2\theta)\,\frac{\partial\theta}{\partial x} - 2k\sin(2\theta)\,\frac{\partial\theta}{\partial y} = 0, \tag{1.36a}$$

$$-\frac{\partial p}{\partial y} - 2k\sin(2\theta)\,\frac{\partial\theta}{\partial x} + 2k\cos(2\theta)\,\frac{\partial\theta}{\partial y} = 0. \tag{1.36b}$$

Equation (1.36a) and (1.36b) are hyperbolic PDEs and can be solved by the method of characteristics (Johnson et al., 2013). The characteristic directions of each of these equations are given by

$$\frac{\mathrm{d}y}{\mathrm{d}x} = \tan\theta, \tag{1.37a}$$

$$\frac{\mathrm{d}y}{\mathrm{d}x} = \tan(\theta + \frac{\pi}{2}), \tag{1.37b}$$

respectively, which show the two families of characteristics form an orthogonal network. The family of characteristics aligned with the θ are called the α-lines and those aligned with the $\theta + \frac{\pi}{2}$ are called β-lines. It can be shown that

$$\begin{aligned} p + 2\kappa\theta &= \text{constant along an } \alpha \text{ line}, \\ p - 2\kappa\theta &= \text{constant along an } \beta \text{ line}. \end{aligned} \tag{1.38}$$

The characteristic lines are trajectories of maximum shear. For this reason, the characteristics are termed slip lines as the material slips (deforms in shear) along these lines (Johnson et al., 2013). Experimentally, these lines can be seen in a realistic plastic deformation situation.

Slip-line theory has been applied to symmetric rolling in some publications (Firbank and Lancaster, 1965; Johnson et al., 2013; Collins, 1969; Alexander, 1955) These are mostly limited to a qualitative discussion of the results due to no computation having been attempted on account of the model's complexity. The slip-line field and the corresponding stress states of material points in the $\tau - \sigma$ plane, as predicted by Firbank and Lancaster (1965) for cold rolling of a sheet, are shown in Figure 1.11. The sheet has an initial thickness of 6 mm and undergoes a 20% reduction, resulting in a roll-gap length of 8 mm. The friction is modelled as Tresca friction law, with the coefficient of friction depending on the angle at which the slip lines intersect the material surface.

At point **A** in Figure 1.11, all lines of one family converge at a single location. This configuration is referred to as an expansion fan (or centred fan) field and is commonly encountered in solutions to plane-strain problems. Singular points often occur at die corners or locations with abrupt cross-sectional changes, where stress, velocity, and strain rate experience rapid transitions. These regions present challenges for FE

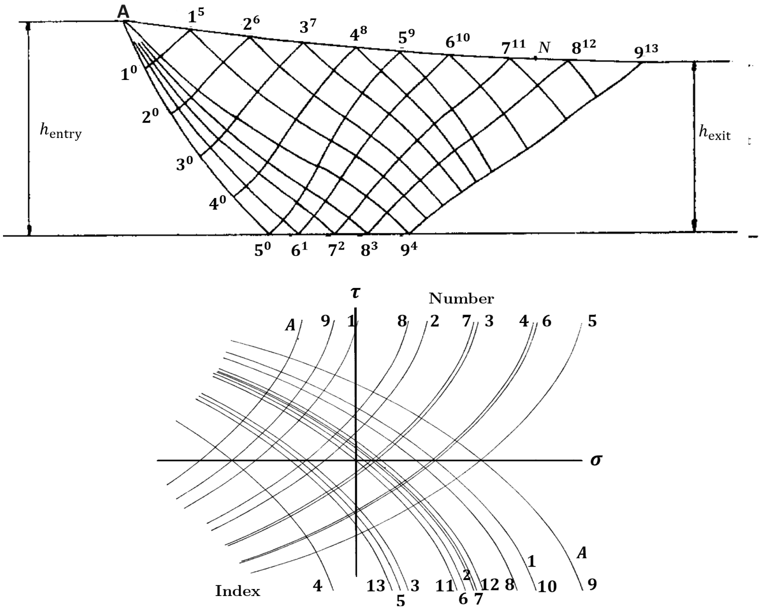

Figure 1.11: Slip-line field for cold rolling (top), and the corresponding stress states of material points in $\sigma - \tau$ space (bottom) (Firbank and Lancaster, 1965).

simulations, as they are difficult to accurately capture due to their localised nature.

1.4.3 Asymptotic models

When solving a continuum mechanics problem, scaling and asymptotic analysis play an important role in eliminating unwanted or unimportant modes of motion. By scaling the equations, meaning choosing an appropriate system of reference units, the parameters governing the system's behaviour become explicit. Asymptotic analysis proves valuable in cases where some of these parameters approach zero or infinity. It is important to note that formal asymptotic analysis with respect to a small parameter indicates only that certain quantities may be negligible in specific regimes, as they still represent higher-order terms in the (formal) asymptotic expansion.

$\sum_{n=1}^{\infty} a_n \phi_n(x)$ is an asymptotic expansion (or asymptotic approximation) of $f(x)$, as $x \to x_0$, if for each N

$$f(x) = \sum_{n=1}^{N} a_n \phi_n(x) + \mathrm{o}(\phi_N(x)), \tag{1.39}$$

as $x \to x_0$, where a_n here are constants and ϕ_n are the gauge functions. Small o notation indicates the order of the error in the approximate solution and reads as the remainder is asymptotically smaller than, or more colloquially, is of "order little o" of $\phi_N(x)$. As such, $\mathrm{o}(\phi_N(x))$ in (1.39) means the error is asymptotically smaller than the last term in the expansion. The other notation which is frequently used in the subsequent chapters is "big O" which means the function is asymptotically bounded in magnitude. The term with the largest order of magnitude is called the leading-order term and the additional terms beyond the leading-order approximation that refine the accuracy of the solution are called the correction terms.

It is important to note that a convergent series does not necessarily have to be asymptotic, and similarly, an asymptotic series does not need to converge. For each value of x, a convergent series has a unique limiting sum $F_\infty(x)$ but it does not provide any information on how well $F_N(x)$ approximates $F_\infty(x)$ for fixed N or on how fast it converges. An asymptotic series, contrarily, does not define a unique function $f(x)$, but rather a whole class of asymptotically equivalent functions. Hence, it does not provide an arbitrarily accurate approximation to $f(x)$ when $x \neq x_0$, whereas it only provides a good approximation for values of the function when x is sufficiently close to x_0. An example of this is the error function. For all values of x,

$$\operatorname{erf}(x) = \frac{2}{\sqrt{\pi}} \sum_{n=0}^{\infty} \frac{(-1)^n}{(2n+1)(n)!} x^{2n+1}, \tag{1.40}$$

which is convergent, but the convergence is very slow as the value of x increases. The asymptotic approximation for $\operatorname{erf}(x)$ as $x \to \infty$ is

$$\operatorname{erf}(x) \approx 1 - \sum_{n=2}^{\infty} \frac{e^{-x^2}}{x\sqrt{\pi}} (-1)^n \frac{(2(n-2))!}{(2x)^{2(n-2)}\,(n-2)!}, \tag{1.41}$$

which is not a convergent series; for any particular value of x there are a fixed number of terms that improve accuracy, after which accuracy worsens. By computation, it can be demonstrated that achieving an accuracy of 10^{-5} for $\operatorname{erf}(3)$ requires including only the first two terms of the asymptotic expansion 1.41, while the same level of accuracy would necessitate summing over thirty terms in equation (1.40).

The asymptotic technique was first utilised in metal forming in 1987 by Robert E. Johnson (Johnson, 1987) to study the conical extrusion of metal followed by a series of papers applying the same techniques to sheet rolling with Johnson as a common author (Smet and Johnson, 1989; Johnson, 1991; Johnson and Smelser, 1992). Considering the wide variety of rolling conditions, numerous non-dimensional groups, derived from parameters such as the aspect ratio, friction coefficient, sheet reduction, the ratio of maximum pressure to yield stress, and the ratio of reduction to roll-bite length, are commonly found in the literature on symmetric rolling of sheet metal. These parameters are assumed to be small or large depending on the specific focus of the study. A more detailed review of these considerations will be provided in the next chapter.

1.5 Thesis outline

Chapter 2 regenerates the results of two different asymptotic models for sheet rolling and, after analysing their shortcomings, suggests an alternative asymptotic model of sheet rolling. It is developed for rigid perfect-plastic material by exploiting an assumption: that the reduction is small and that the effect of friction is weak. While the scaling approach presented in Chapter 2 proves effective in addressing the limitations of asymptotic models discussed in the literature, it is acknowledged that this method cannot be applied to long and thin roll gaps typically seen in industrial cold rolling processes. In Chapter 3, a multiple-scales asymptotic approach is introduced to broaden the applicability of the model, while maintaining the same material model. In Chapter 4, the material model is modified to incorporate the hardening properties of metals. In Chapter 5 a mathematical model for the flat rolling of wire is introduced, building on the framework established in the sheet rolling model.

In each of these chapters, results are compared against either FE simulations or experimental results, although the numerical and experimental work was performed by collaborators and does not in itself form part of this thesis.

Chapter 2

Deficiencies in simple models of sheet rolling

Two mathematical models for symmetric rolling of a rigid, perfectly-plastic sheet are reviewed. Both models share the same assumptions: the ratio of half thickness to the length of roll gap and the friction coefficient are small. However, the key difference lies in the length scale considered. We demonstrate that this difference plays a crucial role and briefly describe its characteristic features. Yet, neither model is able to capture critical aspects of the problem. This limitation highlights that the problem extends beyond the reach of standard methods based on formal asymptotic expansions, as indicated by the title of this chapter.

The global model in its dimensional form is formulated in Section 2.2. The asymptotic model using roll gap length $\hat{\ell}$ as the scaling parameter for horizontal distance is reviewed in Section 2.3 and the deficiencies are discussed. In Section 2.4 the horizontal distance is scaled with sheet initial half thickness $\hat{h}_0$. To show the shortcomings of the latter model, the model is compared with FE simulations. Therefore, we first outline the FE simulation, conducted by the collborators Flanagan et al. (2024), in Section 2.5, and then discuss the deficiencies of the model in Section 2.6.

It should be noted that similar asymptotic models can be found in the literature. The first case is used by Minton et al. (2016) for antisymmetric thin sheet rolling and by Cawthorn et al. (2016) for sandwich rolling, where the solution is asymptotically expanded in terms of δ. The second case is used by Minton (2017) for thick sheet rolling, where the solution is expanded in terms of the reduction ratio r.

2.1 Introduction

Asymptotics utilises systematic assumptions of scale, as opposed to ad-hoc assumptions of unknown error and limitation (Minton, 2017). Asymptotics is especially effective in situations where parameters are not of the same magnitude (i.e., one parameter is notably smaller compared to the others). As such, asymptotics has found successful application in the modelling of rolling, where the presence of a small parameter is readily identifiable. Johnson and Smelser (1992) developed the first asymptotic formulation of the sheet metal rolling process with a weak shear stress effect, arising from a comparatively small friction coefficient in a long and thin roll gap (large aspect ratio, $1/\delta$). Under the same conditions as those assumed in the slab method, their leading-order solution was found to be vertically homogeneous. In their analysis, major simplifications were achieved by adopting the Tresca friction law ($\hat{\tau}_s = \pm\beta\hat{Y}_0$), which enabled analytical approximations for both the leading-order and first-order stress distributions. In a joint study with Cherukuri et al. (1997), the same authors explored an alternative friction condition, given by velocity as $\hat{\tau}_s = \hat{\kappa}\Delta\hat{u}$, where $\Delta\hat{u}$ denotes the relative slip between the rolls and the sheet. Unlike the earlier work, this study allowed for large, moderate, and small shear effects. The formulation in Smet and Johnson (1989) reintroduced Coulomb friction to study rolling with a large aspect ratio involving significant inhomogeneous effects, particularly in two different cases; in one, the reduction was assumed to be large, and in the other, the roll pressure substantially exceeded the yield stress. In their model, the location of the neutral point and the roll pressure at that point, $|\hat{\sigma}_{yy}|_{\max}$, were treated as input parameters, from which the corresponding front and back tensions were determined. Domanti and McElwain (1995) studied rolling similarly for the case of large aspect ratios, where friction causes the roll pressure to significantly exceed the flow stress. In their analysis, the reduction, friction coefficient, and the ratio of half-thickness to length were assumed to be of the same order. Minton et al. (2016) studied asymmetric rolling, and Cawthorn et al. (2016) investigated sandwich rolling using the asymptotic method, both rely on the assumption that the friction coefficient and the ratio of half-thickness to length are small.

A key element of asymptotic analysis is the selection of appropriate scalings for the problem being modelled. By scaling the equations—choosing a suitable system of reference units—the parameters governing the system's behaviour become explicit. In the cold rolling system, three fundamental physical dimensions are identified: stress, length, and velocity. Each physical quantity can be expressed in the units derived from these fundamental dimensions. However, given the wide range of possible rolling conditions, the choice of characteristic unit for these dimensions is not unique. The various scaling parameters used for non-dimensionalising quantities in rolling problems, as adopted in the studies reviewed here, are summarised in Table 2.1 (The equations relating these parameters to one another will be introduced in the following section).

Despite variations in non-dimensionalised factors and small parameters, the reviewed asymptotic models share a common feature: the use of a single horizontal length scale. This approach, as will be argued in the current chapter, does not yield accurate through-thickness predictions. In this work, similar to many asymptotic models for rolling (Domanti and McElwain, 1995; Minton et al., 2016; Cherukuri et al., 1997), the

Table 2.1: Different scaling factors used in literature. For symbols, refer to the following section 2.2.

Reference	$\hat{x}$	$\hat{y}$	$\hat{s}_{xx}$ $\hat{s}_{yy}$	$\hat{s}_{xy}$	$\hat{p}$	$\hat{u}$	$\hat{v}$	$\hat{\lambda}$	non-dimensionalised parameters
Johnson and Smelser and Cherukuri et al.	$\hat{\ell}$	$\hat{h}_0$	$\hat{Y}_0$	$\hat{\tau}_0$	$\frac{\hat{\tau}_0}{\delta}$	$\hat{U}_0$	$\hat{U}_0$	$\frac{\hat{U}_0}{\hat{Y}_0\hat{\ell}}$	$\delta = \frac{\hat{h}_0}{\hat{\ell}} << 1$, $\beta = \frac{\hat{\tau}_0}{\hat{Y}_0}$
Smet and Johnson	$\hat{\ell}$	$\Delta\hat{h}_0$	$\hat{Y}_0$	$\lvert\hat{\sigma}_{yy}\rvert_{\max}$ (also for $\hat{\sigma}_{xx}$ and $\hat{\sigma}_{yy}$)	$-$	$\hat{U}_0$	$\hat{U}_0$	$\frac{\hat{U}_0}{\hat{Y}_0\Delta\hat{h}}$	$\delta = \frac{\Delta\hat{h}_0}{\hat{\ell}} << 1$, $\tau = \frac{\hat{Y}_0}{\lvert\hat{\sigma}_{yy}\rvert_{\max}}$
Domanti and McElwain	$\hat{\ell}$	$\hat{h}_0$	$\hat{\kappa}$	$\mu\lvert\hat{\sigma}_{yy}\rvert_{\max}$	$\lvert\hat{\sigma}_{yy}\rvert_{\max}$	$\hat{U}_0$	$\mu r\hat{U}_0$	$\frac{r\hat{U}_0}{\hat{\kappa}\hat{\ell}}$	$\delta = \frac{\hat{h}_0}{\hat{\ell}} << 1$, $\tau = \frac{\hat{\kappa}}{\lvert\hat{\sigma}_{yy}\rvert_{\max}} << 1$, r and μ
Minton et al.	$\hat{\ell}$	$\hat{h}_0$	$\hat{\kappa}$	$\delta\beta\hat{\kappa}$	$\beta\kappa$	$\hat{U}_0$	$\delta\hat{U}_0$	$\frac{\hat{U}_0}{\hat{\kappa}\hat{\ell}}$	$\delta = \frac{\hat{h}_0}{\hat{\ell}} << 1$, $\beta = \frac{\mu}{\delta}$

focus is on cold rolling, where the contact length with the roller is significantly larger than the sheet thickness. In a typical sheet-rolling schedule, the sheet passes through a sequence of roll stands with the roll-gap thickness:length ratio typically varying between 1:10 and 3:10. In cold rolling steel strips, the coefficient of friction typically ranges from 0.15 to 0.4 without lubrication and decreases to 0.05–0.15 when effective lubricants or emulsions are applied. This study specifically examines the well-lubricated case with small friction values. Consequently, we may assume that both the roll-gap thickness-to-length ratio and the friction coefficient are small, although due to the asymptotic framework, they are not neglected entirely.

2.2 Governing equations

The governing equations in their dimensional form remain the same for this chapter as well as Chapters 3 and 4. Therefore, the model is reviewed here to avoid repetition in the subsequent chapters. Figure 2.1 captures the extent of the model. The lateral spread is assumed to be minimal, reducing the problem to 2D plane strain, which is valid away from the workpiece edges for sufficiently wide workpieces. Also, the system considered in this thesis is symmetric about the sheet centre so only a half thickness is shown. The sheet has initial thickness $2\hat{h}_0$ and goes through the reduction r as it passes through the roll gap. Attention is restricted to the region between $\hat{x} = 0$ to $\hat{x} = \hat{\ell}$ in which the sheet is in contact with the rolls, referred to as the roll gap. With the circular roll and the exit point being the location of the narrowest rolls' separation (see Figure 2.1), the length of the roll gap is $\hat{\ell} = \sqrt{2r\hat{h}_0\hat{R} - r^2\hat{h}_0^2}$ in terms of the roll radius

$\hat{R}$, and the reduction ratio r.

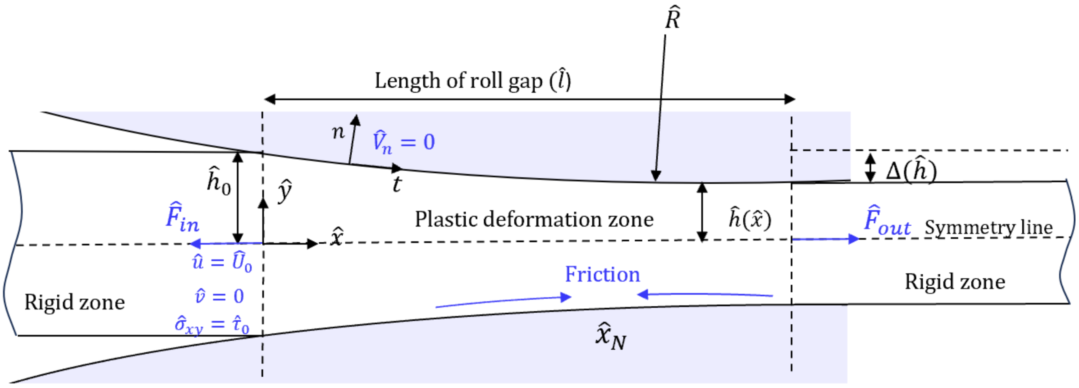

Figure 2.1: A diagram of symmetric rolling with the domain of interest and the boundary conditions. The sheet, which is wide in the direction into the page, enters the roll gap between the two rolls from the left and exits as a thinner sheet to the right.

With the goal of capturing the dynamic of the problem resulting from the geometry, a material model is simplified in the first attempt and will be improved by considering the hardening effect in Chapter 4. Thus, the material is assumed to be perfectly plastic (no hardening), and elastic effects are ignored both in the workpiece and roller. This result in the same set of equations is solved by Minton et al. (2016). The unknown normal and shear Cauchy stresses, $\hat{\sigma}_{xx}$, $\hat{\sigma}_{yy}$ and $\hat{\sigma}_{xy}$, follow von Mises yield criteria and local balances,

$$\frac{1}{4}\left(\hat{\sigma}_{xx} - \hat{\sigma}_{yy}\right)^2 + \hat{\sigma}_{xy}^2 = \hat{\kappa}^2 \quad , \quad \frac{\partial \hat{\sigma}_{xx}}{\partial \hat{x}} + \frac{\partial \hat{\sigma}_{xy}}{\partial \hat{y}} = 0 \quad \text{and} \quad \frac{\partial \hat{\sigma}_{xy}}{\partial \hat{x}} + \frac{\partial \hat{\sigma}_{yy}}{\partial \hat{y}} = 0, \tag{2.1}$$

where the carets denote dimensional quantities. The interface between the workpiece and the rollers is assumed to be slipping throughout the roll gap, and is modelled using Coulomb friction as $\boldsymbol{t} \cdot \hat{\boldsymbol{\sigma}} \cdot \boldsymbol{n} = \mp \mu \boldsymbol{n} \cdot \hat{\boldsymbol{\sigma}} \cdot \boldsymbol{n}$, where $\boldsymbol{n}$ and $\boldsymbol{t}$ are the normal and tangent vectors to the rolls. μ is the friction coefficient which is also assumed to be a known constant parameter. The ± sign accounts for the direction of slip of the sheet over the rolls, as shown in Figure 2.1. The unknown horizontal and vertical velocities and plastic multiplier, $\hat{u}$, $\hat{v}$ and $\hat{\lambda}$, solve mass conservation and flow rule equations,

$$\frac{\partial \hat{u}}{\partial \hat{x}} + \frac{\partial \hat{v}}{\partial \hat{y}} = 0 \quad , \quad \frac{\partial \hat{u}}{\partial \hat{x}} = \frac{1}{2}\hat{\lambda}(\hat{\sigma}_{xx} - \hat{\sigma}_{yy}) \quad \text{and} \quad \frac{1}{2}\left(\frac{\partial \hat{u}}{\partial \hat{y}} + \frac{\partial \hat{v}}{\partial \hat{x}}\right) = \hat{\lambda}\hat{\sigma}_{xy}. \tag{2.2}$$

(Note that we use $\hat{u}$ for the horizontal velocity, and not for the displacement; in what follows, we will always be dealing with velocities and never with displacements.) The velocity on the roll surfaces is restricted by the no-penetration condition $\hat{V}_n = 0$, where $\hat{V}_n$ is the normal component of sheet velocity.

It is sometimes convenient to write Cauchy stresses in terms of deviatoric ones.

The following relation exists between $\hat{\sigma}$ and $\hat{s}$ and $\hat{p}$:

$$\hat{\sigma}_{ij} = \hat{s}_{ij} - \delta_{ij}\hat{p}, \tag{2.3}$$

where $\hat{s}_{ij}$ is the ij^{th} deviatoric stress, and $-\hat{p}$ is a hydrostatic pressure. Compressive stresses are conventionally denoted with a negative sign, and defining the hydrostatic pressure as $-\hat{p}$ serves the same purpose. In plane-strain condition, $-\hat{p}$ is defined as:

$$-\hat{p} = \frac{1}{2}(\hat{\sigma}_{xx} + \hat{\sigma}_{yy}). \tag{2.4}$$

It will also be useful in the analysis below to use a thickness-averaged description of mass conservation, describing the mass balance in each through-thickness slice. Integrating the mass conservation law in (2.2) from $\hat{y} = -\hat{h}$ to $\hat{y} = +\hat{h}$ and applying the no-penetration rule $\hat{v} = \hat{u}\mathrm{d}\hat{h}/\mathrm{d}\hat{x}$ yields

$$\int_{-\hat{h}(\hat{x})}^{\hat{h}(\hat{x})} \hat{u}\ \mathrm{d}\hat{y} = 2\hat{U}_0\hat{h}_0. \tag{2.5}$$

2.3 Scaling the horizontal coordinate with the length of roll gap

In what follows, the horizontal distance is measured in multiples of the roll gap length $\hat{\ell}$. For consistency with the notation in the next chapter, the non-dimensinalised length, scaled with $\hat{\ell}$ is denoted by z. Therefore, the roll gap extends horizontally from $z = 0$ to $z = 1$. The vertical distances are scaled with the initial workpiece half-thickness $\hat{h}_0$, therefore, the vertical gap between the rolls is from $y = -h(z)$ to $y = h(z)$ due to symmetry, where $\hat{h}(\hat{x}) = \hat{h}_0 h(z)$ is a function describing roll shape. The deviatoric and Cauchy stress components and the hydrostatic pressure are equally non-dimensionalised with $\hat{\kappa}$, and correspondingly the entrance and end tensions per unit width with $\hat{\kappa}\hat{h}_0$. In this study, small values of $\delta = \hat{h}_0/\hat{\ell}$ are of interest, corresponding to roll gaps with a narrow roll gap. Another small parameter in this model is the friction coefficient, μ, which is typically of the same order of magnitude as δ. Following previous asymptotic studies (Minton et al., 2016; Cawthorn et al., 2016), we formally encoded this here by setting $\mu = \delta\beta$, where β may be thought of as the normalised friction coefficient. Velocities are scaled by the upstream workpiece velocity denoted as $\hat{U}_0 = \hat{u}(0, \hat{h})$. It should be noted that $\hat{U}_0$ is taken as an undefined characteristic velocity for the purpose of non-dimensionalisation and its value is determined later from the roll velocities. Finally, the plastic parameter, $\hat{\lambda}$, is non-dimensionalised with $\frac{\hat{U}_0}{\hat{\ell}\hat{\kappa}}$, so that it complies with the flow rules equation units. Armed with these definitions,

$$\begin{aligned}
&\hat{x} = \hat{\ell} z, && \hat{h}(\hat{x}) = \hat{h}_0 h(z) = \delta \hat{\ell} h(z), && y = \delta \hat{l} y, \\
&\hat{\sigma}_{ij} = \hat{\kappa} \sigma_{ij}, && \hat{s}_{ij} = \hat{\kappa} s_{ij}, && \hat{p} = \hat{\kappa} p, \\
&\hat{u} = \hat{U}_0 u, && \hat{v} = \hat{U}_0 v, && \hat{\lambda} = \frac{\hat{U}_0}{\hat{\ell}\hat{\kappa}} \lambda,
\end{aligned} \tag{2.6}$$

the non-dimensional governing equations will be,

$$\delta \frac{\partial \sigma_{xx}}{\partial z} + \frac{\partial \sigma_{xy}}{\partial y} = 0, \qquad \frac{\partial \sigma_{yy}}{\partial y} + \delta \frac{\partial \sigma_{xy}}{\partial z} = 0, \tag{2.7}$$

$$\delta \frac{\partial u}{\partial z} + \frac{\partial v}{\partial y} = 0, \qquad \frac{\partial u}{\partial z} = \frac{1}{2} \lambda \left(\sigma_{xx} - \sigma_{yy} \right), \qquad \frac{\partial u}{\partial y} + \delta \frac{\partial v}{\partial z} = 2 \delta \lambda \sigma_{xy}, \tag{2.8}$$

$$\frac{1}{4} \left(\sigma_{xx} - \sigma_{yy} \right)^2 + \sigma_{xy}^2 = 1, \qquad \sigma_{xx} + \sigma_{yy} = -2p. \tag{2.9}$$

The boundary conditions on the surface are the Coulomb friction and the no-flux condition constraining the flow of material on the surface, which are expressed respectively as

$$\delta \frac{\mathrm{d}h}{\mathrm{d}z} \left(\sigma_{yy} - \sigma_{xx} \right) + \left(1 - \delta^2 (\frac{\mathrm{d}h}{\mathrm{d}z})^2 \right) \sigma_{xy} = \mp \delta \beta \left(\sigma_{yy} - 2\delta \frac{\mathrm{d}h}{\mathrm{d}z} \sigma_{xy} + \delta^2 (\frac{\mathrm{d}h}{\mathrm{d}z})^2 \sigma_{xx} \right), \tag{2.10}$$

$$v = \delta \frac{\mathrm{d}h}{\mathrm{d}z} u, \tag{2.11}$$

where based on the surface boundary condition (2.10), the surface is assumed to slip along the roll throughout the roll gap unless a single point $\hat{x}_{\mathrm{N}}$, which is the neutral point, and $\mp = \mathrm{sgn}(\hat{x} - \hat{x}_{\mathrm{N}})$ in (2.10) gives the correct direction of the friction force; for the rest of this thesis, we use the convention that the $-$ sign in $\mp$ refers to the zone before the neutral point ($\hat{x} < \hat{x}_{\mathrm{N}}$), and the $+$ sign refers to the zone after the neutral point ($\hat{x} > \hat{x}_{\mathrm{N}}$).

Assuming non-dimensionalised tensions per unit width $F_{\mathrm{in/out}}$ are applied at the entrance and exit,

$$F_{\mathrm{in/out}} = \int_{-h_{\mathrm{in/out}}}^{h_{\mathrm{in/out}}} \sigma_{xx} \Big|_{\mathrm{in/out}} \mathrm{d}y, \tag{2.12}$$

where $h_{\mathrm{in}} = 1$ by our non-dimensionalization, and h_{out} is half of the final thickness imposed by the rolls. Horizontal velocity is also assumed to be prescribed at the entrance as,

$$u(z = 0) = 1. \tag{2.13}$$

The averaged mass balance (2.5) becomes

$$v = \delta \frac{\mathrm{d}h}{\mathrm{d}z} u \qquad \text{and} \qquad \int_{-h(z)}^{h(z)} u \ \mathrm{d}y = 2. \tag{2.14}$$

Finally, symmetry about the centre line ($y = 0$) is applied;

$$\sigma_{xy}(y = 0) = 0 \qquad \text{and} \qquad v(y = 0) = 0. \tag{2.15}$$

In order to solve equations (2.7)-(2.15), the stress components, velocity components, and plastic parameter are expanded as asymptotic series in the small parameter δ,

$$\phi = \phi^{(0)}(z, y) + \delta\phi^{(1)}(z, y) + O(\delta^2), \tag{2.16}$$

where ϕ represents any of the mentioned variables. Under the assumption that δ is small, each power of δ represents a small correction to the terms preceding it. The expanded versions of equations can be obtained by substituting a provided expansion into the non-dimensionalized governing equations. Like terms can then be collected and solved successively starting from low orders of δ, assuming δ is sufficiently small.

2.3.1 Solution

At leading order, the friction equation (2.10) implies that $\sigma_{xy}^{(0)}$ is zero on the roll surface, and the local balance equation (2.7) implies that it is independent of y. Hence, $\sigma_{xy}^{(0)} \equiv 0$ everywhere; i.e. the shear stress σ_{xy} is small and of order at most $O(\delta)$ throughout the roll gap. It is important to to highlight that scaling is generally carried out to ensure a non-zero leading-order solution, necessitating the shear stress to be scaled with δ. However, this convention has not been followed here, as the shear stress is considered a part of the stress tensor, with the entire tensor being scaled using $\hat{\kappa}$. With zero shear stress at leading order, the yield equation (2.9) is reduced to

$$\frac{1}{4}\left(\sigma_{xx}^{(0)} - \sigma_{yy}^{(0)}\right)^2 = 1. \tag{2.17}$$

Substituting for the leading-order hydrostatic pressure $-2p^{(0)} = \sigma_{xx}^{(0)} + \sigma_{yy}^{(0)}$, we therefore have

$$\sigma_{xx}^{(0)} = 1 - p^{(0)} \qquad \text{and} \qquad \sigma_{yy}^{(0)} = -1 - p^{(0)}, \tag{2.18}$$

where we have asserted that σ_{yy} is more compressive than σ_{xx}, which can be explained by the deformation mechanism in the roll gap with the sheet getting longer and thinner, forced by the rolls rather than extensive horizontal forces at the entrance and exit. From local balance equation (2.7) at leading order, $\sigma_{yy}^{(0)}$ is independent of y, and so consequently are $p^{(0)}$ and $\sigma_{xx}^{(0)}$. This implies that both normal stress components are vertically homogeneous at this order. The solution for $p^{(0)}(z)$ will be dictated by satisfying the friction expression (2.10) at $O(\delta)$ on the surface, although this involves the as-yet-unknown $\sigma_{xy}^{(1)}$, and so we must first solve the first-order equations before $p^{(0)}$ can be fully determined.

At first-order correction, $p^{(1)}$, $\sigma_{xx}^{(1)}$ and $\sigma_{yy}^{(1)}$ solved to be identically zero. Therefore, from the local balance equation (2.7) at first order, we have

$$\sigma_{xy}^{(1)} = y\frac{\mathrm{d}p^{(0)}}{\mathrm{d}z}. \tag{2.19}$$

Substituting this into the friction equation (2.10) at first order, an ODE for $p^{(0)}$ is derived.

$$-2\frac{\mathrm{d}h}{\mathrm{d}z} \mp \beta\left(1 + p^{(0)}\right) + h\frac{\mathrm{d}p^{(0)}}{\mathrm{d}z} = 0. \tag{2.20}$$

Boundary conditions for $p^{(0)}$ are the prescribed front and back tension at the entrance and exit (2.12),

$$p^{(0)}(z=0) = 1 - \frac{F_{\text{in}}}{2} \qquad \text{and} \qquad p^{(0)}(z=1) = 1 - \frac{F_{\text{out}}}{2h(1)}, \tag{2.21}$$

which gives the complete solution to $p^{(0)}$. This is the same solution as the slab method and the two curves thus produced are the friction hill, with the location of the intersection of the curves defining the location of the neutral point at leading order (see Figure 1.10). The solution is extended to determine the velocity fields. Evaluating (2.8) at leading order yields

$$\frac{\partial u^{(0)}}{\partial y} = 0, \tag{2.22}$$

indicating $u^{(0)}$ is uniform across the sheet thickness, as was found for the stress components at this order. Evaluating the averaged mass equation (2.14) at leading order then yields

$$u^{(0)}(z) = \frac{1}{h(z)}. \tag{2.23}$$

Based on the tension flow rule equation (2.8), the leading-order plastic multiplier $\lambda^{(0)}$ is also found to be

$$\lambda^{(0)} = -\frac{1}{h^2}\frac{\mathrm{d}h}{\mathrm{d}z} \tag{2.24}$$

The vertical velocity at leading order, $v^{(0)}$, is identically zero. This can be determined by evaluating the continuity equation (2.8) at leading order to show that $v^{(0)}$ is independent of y, and using the no-penetration boundary condition (2.13), which imposes zero vertical velocity $v^{(0)}$ on the surface.

At first-order correction, $u^{(1)}$ and $\lambda^{(1)}$ are solved to be identically zero, and $v^{(1)}$

is found from the continuity equation (2.8) at first order as

$$v^{(1)} = \frac{y}{h^2}\frac{\mathrm{d}h}{\mathrm{d}z} \tag{2.25}$$

In this way, the solution can be summarised as,

$$p = p^{(0)}(z) + O(\delta^2), \qquad 2\frac{\mathrm{d}h}{\mathrm{d}z} \mp \beta\left(1 + p^{(0)}\right) + h\frac{\mathrm{d}p^{(0)}}{\mathrm{d}z} = 0, \tag{2.26a}$$

$$\sigma_{xx} = \left(1 - p^{(0)}\right) + O(\delta^2), \qquad \sigma_{yy} = -\left(1 + p^{(0)}\right) + O(\delta^2), \tag{2.26b}$$

$$\sigma_{xy} = \delta y\frac{\mathrm{d}p^{(0)}}{\mathrm{d}z} + O(\delta^3), \tag{2.26c}$$

$$u = \frac{1}{h(z)} + O(\delta^2), \qquad v = \delta\frac{y}{h^2}\frac{\mathrm{d}h}{\mathrm{d}z} + O(\delta^3), \tag{2.26d}$$

$$\lambda = -\frac{1}{h^2}\frac{\mathrm{d}h}{\mathrm{d}z} + O(\delta^2) \tag{2.26e}$$

In the set of equations (2.26a), the leading-order terms for all variables are vertically homogenous, consistent with the predictions of the slab method. Further accuracy can still be achieved by repeating this process with terms of higher orders. In practice, each variable raises an order as a polynomial in y in each correction. As a result, horizontal velocity, pressure, longitudinal stresses, and the flow parameter become quadratic in y and vertical velocity and shear stress become cubic. The solution is derived for antisymmetric rolling by Minton et al. (2016) and for sandwich rolling by Cawthorn et al. (2016). The same procedure can be applied to obtain the $O(\delta^2)$ terms, therefore, the derivation is omitted here for brevity.

2.3.2 Deficiencies

2.3.2.1 Contradicting force balance at the neutral point

The results for p considering the second-order correction and σ_{xy} considering the third-order correction are plotted in Figure 2.2, using the supplementary code from Minton et al. (2016). The contour plots of pressure, along with the results on the surface, are plotted in the left panel. In the absence of the first-order correction for pressure, the solution is almost approximated by the leading-order solution, while the second-order correction slightly increases the through-thickness resolution of the solution (see the curved contour lines instead of vertical ones in p). In such a case, the solution for p on the surface recovers the pressure hill. The contour plots of shear stress, along with the profile on the surface, are plotted in the right panel of Figure 2.2. The term $y\mathrm{d}p^{(0)}/\mathrm{d}z$ in shear stress causes a sudden change at the neutral point, as illustrated in the right panel of Figure 2.2, which hypothetically causes a discontinuity in shear stress across a straight line running vertically through the thickness of the sheet. Physically, the sudden change in the sign of the shear stress at the surface is a natural outcome of

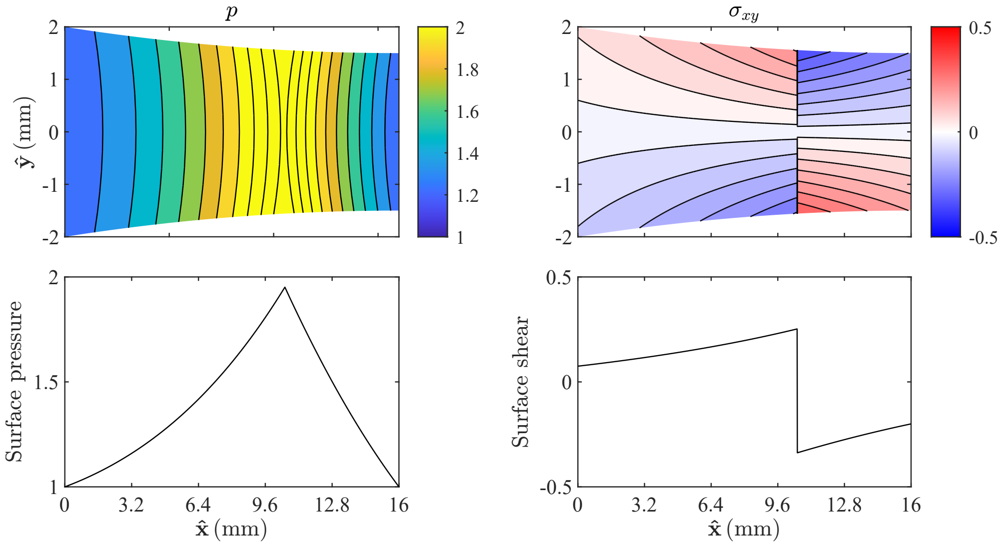

Figure 2.2: Results for $\delta = 0.125$ calculated from the first asymptotic model in Section 2.3 up to the second-order correction for pressure (left panel) and shear (right panel). Top: contour plots; Bottom: results on the surface. Results are shown in dimensionless form, i.e. scaled with $\hat{\kappa}$, the yield stress in shear. Parameters used are $(\hat{h}_0, r, \mu, \hat{\kappa}) = (2\,\mathrm{mm}, 25\%, 0.1, 275.51\,\mathrm{MPa})$.

Coulomb friction. However, any vertical discontinuity through the thickness must be artificial, as it would otherwise violate the balance of vertical forces on a thin vertical slice of material at the neutral point. This is illustrated in Figure 2.3, where the forces acting on three slabs at different locations are demonstrated. The slab I represents the material before the neutral point, slab II after the neutral point, and slab N at the location of the neutral point.

The direction of the surface shear stress is dictated by the direction of friction, which opposes the relative velocity. Since the sheet velocity is lower than the roll velocity in the entrance region and higher in the exit region, the shear stress direction reverses before and after the neutral point, always pointing toward this point. The vertical component of the shear stress then adjusts to ensure rotational equilibrium, which is upwards before the neutral point and downwards after it, as depicted in Figure 2.3. The sudden change in the direction of shear stress through the thickness at the neutral point, as required by the current asymptotic model, causes the vertical component of shear stress to align in the same direction on both sides of the element. This alignment leads to a mismatch in the force balance in the vertical direction on half of slab N, extending from the symmetry line to the surface, as the thickness approaches zero. To avoid this force balance violation, the shear stress σ_{xy} at the location of the neutral point must be continuous. Of course, this excludes the surface, which is compelled to be discontinuous due to the Coulomb friction boundary condition.

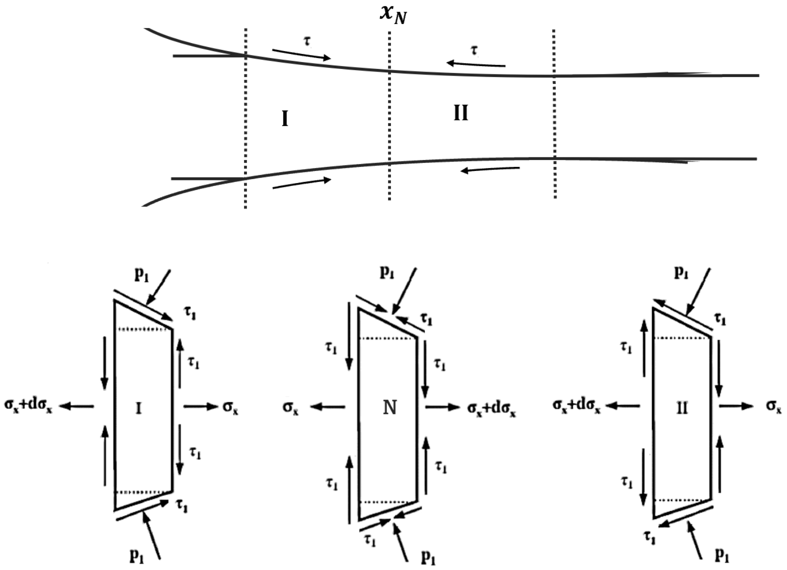

Figure 2.3: A diagram of the entrance (I), neutral (N) and exit region (II), with forces acting on representative slabs in each region. The shear stress prediction based on the first asymptotic model in Section 2.3 leads to the contradiction of vertical components of shear stress being the same on both sides of slabs at the neutral point.

2.3.2.2 Inaccurate through-thickness prediction

One of the consequences of the slab method, and likewise this asymptotic model, is precluding the possibility of more than one pressure peak. However, further published data indicate that this assumption may not always hold: The wave-like roll pressure was first reported experimentally by MacGregor and Palme (1959) and subsequent researchers further confirmed this observation.

MacGregor and Palme (1959) observed two distinct pressure peaks during rolling: one in the entry zone and another at the exit. They attributed the entrance peak to the yielding restriction caused by the adjacent more rigid elastic regions, and the exit peak to the deformation hardening of the material. Similarly, using the method of slip lines, for a sheet with comparable half thickness and length, Firbank and Lancaster (1965) also found two pressure peaks with a marked drop in pressure between them. Subsequently, Al-Salehi et al. (1973) conducted a series of experiments with different materials and aspect ratios and measured multiple pressure peaks.

The oscilations were subsequently confirmed through FE analyses (Yarita et al., 1985; Prakash et al., 1995; Minton, 2017; Flanagan et al., 2024), including the study by Montmitonnet (2006). He observed the transition between single and multiple peaks at $\hat{\ell}/2\hat{h}_0 \approx 3$. Figure 2.4 illustrates the pressure and shear on the surface for varying values of $\hat{\ell}/2\hat{h}_0$, along with contour plots of strain rates derived from Abaqus simulations. Montmitonnet (2006) explained these oscillations using the concept of slip bands: at low $\hat{\ell}/2\hat{h}_0$, a small number of concentrated strain rate bands results in distinct pressure peaks. As $\hat{\ell}/2\hat{h}_0$ increases, numerous faint strain rate concentration bands emerge, causing small stress oscillations that merge into the broader friction hill. Higher-resolution FE simulations from Minton (2017), however, reveal that stress oscillations persist even at larger values of $\hat{\ell}/2\hat{h}_0$, indicating that the pressure hill is merely an approximation of pressure. Figure 2.5 presents contour plots of shear stress for varying values of $\hat{\ell}/2\hat{h}_0$ in which the oscillatory pattern is still evident at $\hat{\ell}/2\hat{h}_0 = 5$ and only begins to diminish at $\hat{\ell}/2\hat{h}_0 = 10$.

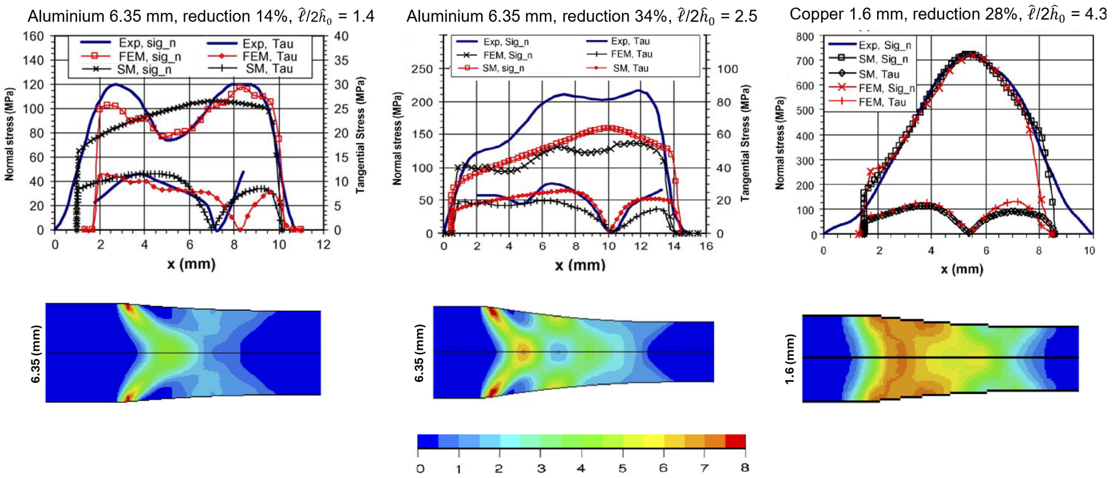

Figure 2.4: Oscillations in stress and strain for different $\hat{\ell}/2\hat{h}_0$ from Montmitonnet (2006). Top row: contact stress (sig_n) and shear on surface (Tau) recorded with three different methods, experimental results (Exp), slab method (SM) and 2D FEM (FEM). Bottom row: generalised strain-rate contour plots from FEM.

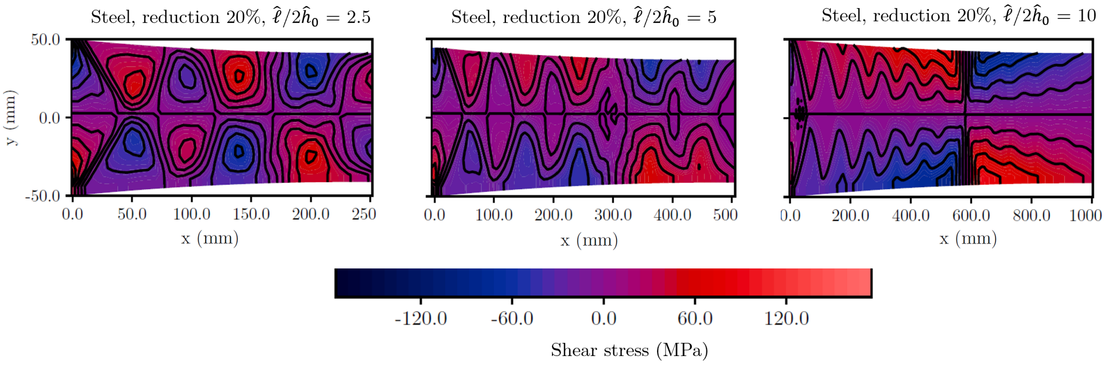

Figure 2.5: Contourplots of shear stress for different $\hat{\ell}/2\hat{h}_0$ using Abaqus simulation from Minton (2017)

The wave-like roll pressure observed in both experiments and FE simulations arises from complex through-thickness behaviour, which neither the slab method nor this asymptotic model adequately captures. The noted shortcomings, including inaccuracies in force balance, incorrect through-thickness predictions, and unclear characterisation of the oscillation patterns, underscore the need for a different modelling approach. Unlike the pressure hill, which varies across the roll-gap length, these oscillations repeat over a smaller length scale. This observation suggests a revised asymptotic model where the horizontal distance is scaled by the initial half-thickness of the sheet rather than the roll-gap length.

2.4 Scaling the horizontal distance with the initial half thickness

In what follows, we choose to measure the horizontal distance in multiples of the strip's initial half-thickness $\hat{h}_0$ instead of $\hat{\ell}$. We therefore adopt a distinct notation for the non-dimensionalised horizontal length, differing from that used in the previous section; here, we define $\hat{x} = \hat{h}_0 x$. With this definition, the roll gap extends horizontally from $x = 0$ at the roll gap entrance to $x = 1/\delta$ at the roll gap exit, where $\delta = \hat{h}_0/\hat{\ell}$ is still the small parameter. The $\hat{\lambda}$ necessarily varies over the length of the roll gap and therefore must be scaled by $\hat{\ell}$ and not $\hat{h}_0$. Therefore, we write $\hat{\lambda} = \lambda \frac{\hat{U}_0}{\hat{\ell}\hat{\kappa}} = \delta\lambda \frac{\hat{U}_0}{\hat{h}_0\hat{\kappa}}$, and use $\delta\lambda$ in the following equations to show this dependancy. Other parameters are scaled the same as written in (2.6). It should be emphasised that, under the same small parameters in the current asymptotic model (δ and μ), we ascertain that $\mathrm{d}\hat{h}/\mathrm{d}\hat{x}$, $\hat{v}$, and $\hat{\sigma}_{xy}$ are all $O(\delta)$, consistent with the asymptotic model presented in the previous section. Hence, there are many similarities between the equations in this section and those in the previous one, with the only differences arising in the equations that include $\frac{\partial}{\partial z}$. The set of equations (2.7) and (2.8) with the new scaling for $\hat{x}$ are written as

$$\frac{\partial \sigma_{xx}}{\partial x} + \frac{\partial \sigma_{xy}}{\partial y} = 0, \qquad \frac{\partial \sigma_{yy}}{\partial y} + \frac{\partial \sigma_{xy}}{\partial x} = 0, \tag{2.27}$$

and

$$\frac{\partial u}{\partial x} + \frac{\partial v}{\partial y} = 0, \qquad \frac{\partial u}{\partial x} = \frac{1}{2}\delta\lambda(\sigma_{xx} - \sigma_{yy}), \qquad \frac{\partial u}{\partial y} + \frac{\partial v}{\partial x} = 2\delta\lambda\sigma_{xy}, \tag{2.28}$$

respectively. Unlike eqation (2.7), where the shear stress at each order depended on the known normal stress from the previous order, equation 2.27 requires normal and shear stresses to be solved simultaneously. The same applies to the horizontal and vertical velocity components. The remaining governing equations, from (2.9) to (2.15), are applied without any changes.

With $\sigma_{xy}^{(0)} = 0$, we recover the same expressions for $\sigma_{xx}^{(0)} = 1 - p^{(0)}$ and $\sigma_{yy}^{(0)} = -1 - p^{(0)}$ from the yield criterion as in the previous asymptotic model. However, the pressure depends on the local balance equations, which are different in this model. From local balance equations (2.27) at leading order,

$$\frac{\partial \sigma_{xx}^{(0)}}{\partial x} = 0 \qquad \text{and} \qquad \frac{\partial \sigma_{yy}^{(0)}}{\partial y} = 0, \tag{2.29}$$

This coupled with the solution for $\sigma_{xx}^{(0)}$ and $\sigma_{yy}^{(0)}$ results in $p^{(0)}$ being constant, which can be found from boundary condition (2.12) as

$$p^{(0)} = 1 - \frac{F_{\text{in}}}{2} \tag{2.30}$$

Similarly, form flow rule equations (2.28), $u^{(0)}$ is found to be a constant (recall that we set $v^{(0)} = 0$). Therefore, due to our scaling

$$u^{(0)} = 1. \tag{2.31}$$

At first-order correction, the solution for $\sigma_{xy}^{(1)}$ is coupled with $\sigma_{xx}^{(1)}$ and $\sigma_{yy}^{(1)}$ through local balance equations (2.27) as

$$\frac{\partial \sigma_{xy}^{(1)}}{\partial y} - \frac{\partial p^{(1)}}{\partial x} = 0 \qquad \text{and} \qquad \frac{\partial \sigma_{xy}^{(1)}}{\partial x} - \frac{\partial p^{(1)}}{\partial y} = 0, \tag{2.32}$$

when applying $\sigma_{xx}^{(1)} = \sigma_{yy}^{(1)} = -p^{(1)}$. The two above equations are the wave equations for $p^{(1)}$ and $\sigma_{xy}^{(1)}$. Thus

$$p^{(1)} = A\left(x+y\right) + A\left(x-y\right) + D \tag{2.33}$$

$$\sigma_{xy}^{(1)} = A\left(x+y\right) - A\left(x-y\right), \tag{2.34}$$

where we have made use of p being symmetric about the centre line and σ_{xy} being antisymmetric. The function $A(\xi)$ here is the as-yet-unknown wave solution and D is a constant of integration. The Coulomb friction on the surface (2.10) at this order is

$$-2\frac{dh}{dz} + \sigma_{xy}^{(1)} \mp \beta(1 + p^{(0)}) = 0. \tag{2.35}$$

Substituting $\sigma_{xy}^{(1)}$ into (2.35) results in

$$A\left(x+h\right) - A\left(x-h\right) = 2\frac{dh}{dx} \mp \beta(-1 - p^{(0)}), \tag{2.36}$$

with $\mp$ being minus for the entrance and plus for the exit side. This equation is used for solving $A(\xi + 2h)$ in terms of $A(\xi)$. To drive a solution, the initial condition must be defined. Since F_{in} has already been satisfied at leading order in (2.30), the first-order correction to it must be zero. Hence, according to equation (2.12) we may write,

$$\int_{-h_0}^{h_0} \sigma_{xx}^{(1)}(0,y)\mathrm{d}y = -\int_{-1}^{1}[A(y)+A(-y)]\mathrm{d}y - 2D = 0, \tag{2.37}$$

which defines D in terms of $A(y)$, but does not solve them. Unlike the asymptotic model discussed in the previous section, knowing the forward and backward tension alone is insufficient to determine p and σ_{xy}. Additional information is required to solve for the unknowns $A(\xi)$ and D. The simplest assumption is setting $A(\xi)$ to vary linearly with y, represented as ay. This assumption disregards the initial distribution of $\sigma_{xx}^{(1)}$ and imposes a linear distribution of shear stress as the initial condition and results in $D \equiv 0$. The factor a must be adjusted to achieve the best match for the shear stress. With this, we are able to find $A(\xi)$ from the entrance up to the neutral point with $\mp$ being minus and after that with a plus sign. Unlike the asymptotic model in Section 2.3, the neutral point cannot be found from the leading-order solution ($p^{(0)}$ is constant here). Instead, the location of the neutral point is dictated by the force F_{out} at the exit. From equation (2.12),

$$F_{\text{out}} = \int_{-h(1/\delta)}^{h(1/\delta)} \left(\sigma_{xx}^{(0)}(1/\delta) + \delta\sigma_{xx}^{(1)}(1/\delta,y)\right)\mathrm{d}y, \tag{2.38}$$

where F_{out} is assumed to be $F_{\text{out}}^{(0)} + \delta F_{\text{out}}^{(1)}$. From (2.30) and (2.33) we therefore get

$$F_{\text{out}} - h(1/\delta)F_{\text{in}} = -\delta\int_{-h(1/\delta)}^{h(1/\delta)} \left[A\left(x(1/\delta)+y\right) + A\left(x(1/\delta)-y\right)\right] dy. \tag{2.39}$$

This condition must be satisfied at the exit by selecting the right location for the neutral point. When both forward and backward tensions are zero, this requirement simplifies to $p^{(1)}$ averaging to zero at the exit. Having solved for $A(\xi)$, $p^{(1)}$ and all the components of the Cauchy stress, $\sigma_{xx}^{(1)}$, $\sigma_{yy}^{(1)}$ and $\sigma_{xy}^{(0)}$, can be calculated.

We proceed with the solution by solving $u^{(1)}$ and $v^{(1)}$. By taking terms of order δ, the continuity equation and the shear flow-rule equation in (2.28) are reduced to the following expressions:

$$\frac{\partial u^{(1)}}{\partial x} + \frac{\partial v^{(1)}}{\partial y} = 0, \qquad \frac{\partial v^{(1)}}{\partial x} + \frac{\partial u^{(1)}}{\partial y} = 0. \tag{2.40}$$

Therefore, similar to stresses at this order of correction, $u^{(1)}$ and $v^{(1)}$ follow the wave equation with the general solution of

$$u^{(1)} = B\left(x+y\right) + B\left(x-y\right), \tag{2.41}$$

$$v^{(1)} = -\left[B\left(x+y\right) - B\left(x-y\right)\right], \tag{2.42}$$

where B is an unknown function. The solution above has accounted for the symmetry of u and asymmetry of v with respect to $y = 0$. As a result of the no-penetration boundary condition on the surface

$$v^{(1)} = \frac{\mathrm{d}h}{\mathrm{d}x} u^{(0)} \qquad \Rightarrow \qquad B\left(x+h\right) - B\left(x-h\right) = -\frac{\mathrm{d}h}{\mathrm{d}x}, \tag{2.43}$$

which can be fully solved for $B(\xi)$ using the initial condition that $u^{(1)}$ and $v^{(1)}$ are zero at the entrance. Having solved for $B(\xi)$, $u^{(1)}$ and $v^{(1)}$, can be calculated by evaluating (2.41) and (2.42) respectively.

The contour plots of pressure and shear stress, along with the results on the surface, are plotted with zero forward/backward tension in Figure 2.6. Here, the leading-order pressure remains constant, and the variation in pressure is incorporated into the first-order correction term. $A(\xi)$ increases in average up to the neutral point according to $2\mathrm{d}h/\mathrm{d}x + 2\beta$, and changes with $2\mathrm{d}h/\mathrm{d}x - 2\beta$ after the neutral point, as described by equation (2.36). Since the friction coefficient, μ, must be greater than $\mathrm{d}\hat{h}/\mathrm{d}\hat{x}$ (necessary for successful sheet entry (Lenard, 2013)), it follows that β is also larger than $\mathrm{d}h/\mathrm{d}x$. Consequently, $2\frac{\mathrm{d}h}{\mathrm{d}x} - 2\beta$ becomes negative, indicating that $A(\xi)$ ceases to grow on average after the neutral point. This sudden shift in the behaviour of $A(\xi)$ shows itself as the emergence of another wave originating from the neutral point. As a result, in the pressure and shear contour plot in Figure 2.6, the jagged pattern starting at the neutral point overlays the wave pattern originating from the entrance (In the parameter set used for Figure 2.6, the neutral point occurs at $\hat{x} = 10.75$).

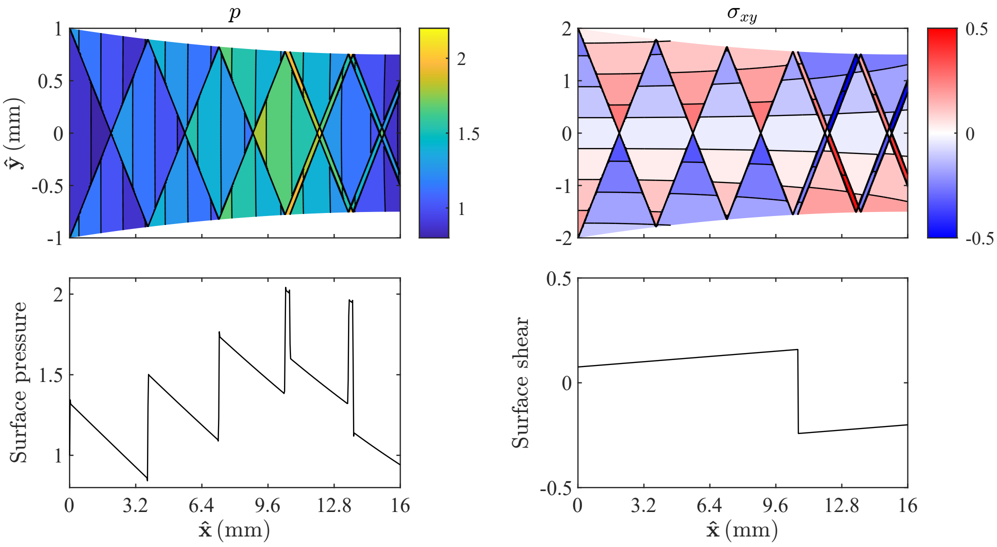

Figure 2.6: Results for $\delta = 0.125$ calculated from the first asymptotic model in Section 2.4 up to the first-order correction for pressure (left panel) and shear (right panel). Top: contour plots; Bottom: results on the surface. Results are shown in dimensionless form, i.e. scaled with $\hat{\kappa}$, the yield stress in shear. Parameters used are $(\hat{h}_0, r, \mu, \hat{\kappa}) = (2\,\mathrm{mm}, 25\%, 0.1, 275.51\,\mathrm{MPa})$.

The shear stress distribution calculated from (2.34) is shown in the right panel of Figure 2.6. While the through-thickness distribution is influenced by the wave equation, the shear on the surface exhibits a trend similar to that derived from the slab method, and the oscillations on the surface are captured through the second-order correction term, which is not included here.

Clearly, the latter asymptotic model has been able to capture the rapid through-thickness stress and strain oscillations. Since it is extremely difficult to experimentally observe the stress pattern through thickness during the rolling process, the predictions of the asymptotic model are compared with carefully conducted FE simulations using the Abaqus package.

2.5 Finite element simulations

All the FE simulations in the rest of this thesis (unless otherwise stated) are conducted by Flanagan et. al., and full details are given in (Flanagan et al., 2024). In summary, simulations are made in Abaqus/Standard with an implicit solver. Only one roll and half the sheet are simulated following the assumption of symmetry about the sheet's horizontal centre plane. To comply with the plane-strain assumption, the sheet metal is modelled as a two-dimensional deformable part and the rolls as a two-dimensional analytical rigid geometry. The contact between the roll and sheet is discretised using the surface-to-surface method. Since a mesh sensitivity study confirmed that under-resolution through-thickness strongly affects the results (Flanagan et al., 2024), here, 30 CPE4R elements were used through the half-thickness of the sheet; this showed the best trade-off between accuracy and computation time (Flanagan et al., 2024). The simulation consists of two steps: the bite step, where the roll is slowly translated vertically to indent the sheet; and the rolling step, where the sheet is horizontally displaced due to rotation of the roll.

By carefully initiating the simulation with this separate bite step, initial transients and numerical oscillations commonly observed in this type of FE calculation are minimised. The model is then run for a sufficiently long time to attain a steady state, as measured by obtaining steady through-thickness stress and strain distributions, rather than simply by observing roll force and torque (Flanagan et al., 2024). For static Abaqus/Standard simulations, although stresses are generated directly, velocity must be calculated from the displacement change between time frames. The computation time for these simulations depends on the aspect ratio, and an example of $\delta = 0.125$ requires a computation time of 15.89 CPU hours.

The sheet material is chosen to be mild steel (grade DC04), a common material used in cold metal forming (Spittel and Spittel, 2009). A realistic Young's modulus of $E = 206.3\,\mathrm{GPa}$ and a Poisson ratio $\nu = 0.3$ are used for all FE simulations. The yield stress is fixed at $\hat{\kappa} = 288.67\,\mathrm{MPa}$, so that the simulation is close to the perfectly-plastic material assumed in the mathematical model. The rolls rotate with a surface speed of $1.28\,\mathrm{ms}^{-1}$, the sheet has an initial full thickness $2\hat{h}_0 = 4\,\mathrm{mm}$, and the size and position of the rolls are varied to give the required roll-gap aspect ratios and reduction ratios. The friction coefficient between the workpiece and the rolls is chosen to be 0.1, except for short roll gaps with $\delta = 0.3$ and 0.5, for which $\mu = \delta/2$ is chosen to guarantee the initial bite. These choices of material, friction coefficient, initial thickness, reduction, and roll speed are purely illustrative, and solutions may be found for any values of these parameters.

2.6 Comparison of two models with FE simulations

In this section, the two asymptotic models are compared with the results from FE simulations. Figure 2.7 shows the prediction for different stress and velocity components from three different methods. The first column is the asymptotic model solved to the first order where the horizontal distance is scaled with the initial half thickness, $\hat{x} = \hat{h}_0 x$, the second is results from Abaqus simulation, and the last column is the asymptotic model solved to the second order where the horizontal distance is scaled with the length of roll gap, $\hat{x} = \hat{\ell} x$. The results in the first column show the oscillatory distribution in all stress and velocity components, which agrees with the Abaqus simulation, whereas the results in the last column are just approximations. In fact, employing the large length scale $\hat{\ell}$ prevents the results from capturing the oscillations that are repeated on the small length scale $\hat{h}_0$.

σ_{xx} increases on average up to the neutral point and declines after that up to the exit point. Nevertheless, unlike the results in the last column, this trend is not continuous. In fact, each momentary increase in σ_{xx} is followed by a subsequent decrease resulting from $A(\xi)$. Pressure differs from σ_{xx} only by an amount of -1 for both asymptotic models. As a result, σ_{xx} and p exhibit the same field pattern, which is confirmed by FE results.

In shear contour plots, the FE results exhibit a smooth transition from positive to negative shear at the surface, along with a neutral region where the roll and sheet share the same tangential velocity (the latter is not immediately apparent in Figure 2.7, but it will be more clearly illustrated in the next chapter in Figure 3.4). This behaviour is not captured in either asymptotic model due to the assumption of Coulomb friction without sticktion. As a result, both asymptotic models show a sudden change in shear direction at the neutral point, leading to a discontinuity. The difference, however, is how the discontinuity runs into the thickness. The diagonal line in the first column is the effect of the sudden change in the trend of $A(\xi)$ due to a change in the direction of friction in equation (2.36). However, in the third column, a vertical discontinuity is due to $y\mathrm{d}p^{(0)}/\mathrm{d}x$. Unlike the vertical discontinuity, the diagonal discontinuity does not violate force balance because both the normal and tangential forces on a thin sliver of material along the discontinuity balance.

The oscillations are also observed in both velocity components, u and v. In the

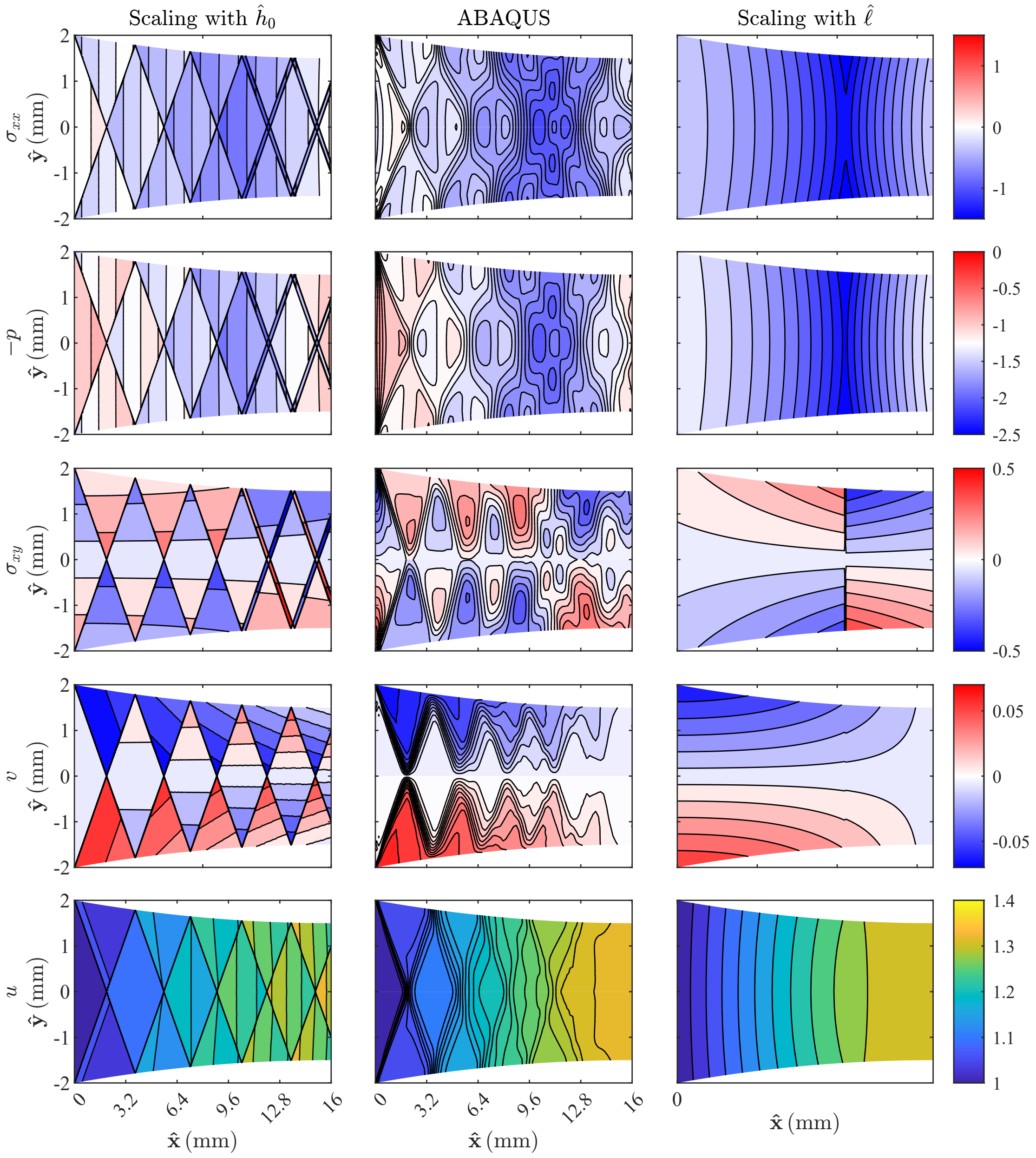

Figure 2.7: Comparison of shear stress (σ_{xy}), Horizontal stress (σ_{xx}), pressure ($-p$), vertical (v) and horizontal (u) velocities from three different methods. The second asymptotic model in Section 2.4 (left panel), FE simulation (Flanagan et al., 2024) (middle panel), and the first asymptotic model in Section 2.3 (right panel). Results are shown in dimensionless form. Parameters used are $(\delta, \hat{h}_0, r, \mu, \hat{\kappa}) = (0.125, 2\,\text{mm}, 25\%, 0.1, 275.51\,\text{MPa})$.

FE simulation, the vertical velocity reveals a distinct distribution; material points are pushed toward the centerline due to the roll effect, but only in certain regions, while the areas in between experience no vertical displacement. This behaviour is not captured by either asymptotic model. Similarly, neither model reproduces the horizontal velocity trends observed in the FE simulation. In the simulation, the horizontal velocity increases from the entrance to near the exit, characterized by a series of incremental steps, and remains nearly constant just before the exit. The result in the first column exhibits oscillations but predicts a velocity drop in each separate zone and fails to capture the constant velocity near the exit. Contrarily, the third-column result correctly predicts the constant velocity near the exit but shows a continuous rise instead of the step-like growth observed in simulations. Moreover, it inaccurately predicts that the surface velocity is lower than the centre velocity at the entrance.

2.6.1 Deficiencies

Although the latter asymptotic model in Section 2.4 successfully predicts oscillations in the stress and velocity fields by scaling the horizontal distance with the initial half thickness, it fails to account for variations that evolve over the long length of the roll gap, such as the pressure hill. As a result, some aspects of the solution are better predicted by the first asymptotic model in Section 2.3.

Another limitation lies in the predicted stress and velocity lobes. While the diagonal lines predicted by the model resemble the oscillations observed in ABAQUS simulations, the contour lines from simulations soon change shape, whereas the model predicts unchanging patterns that persist up to the exit. Furthermore, in simulations, the fields at the entrance feature concentrated contour lines near the surface, followed by a spread. This behaviour (the expansion fan) reflects the evolution of the discontinuity in the initial condition, as explained in Section 1.4.2, and is evident across all stress and velocity components in the simulations but remains unaccounted for in the model.

2.7 Conclusion

Two simple mathematical models for symmetric rolling of rigid-perfect plastic sheets under Coulomb friction have been reviewed based on the models from literature (Minton et al., 2016; Minton, 2017; Cawthorn et al., 2016). While the same assumptions of small δ, and the friction coefficient, μ are adopted, different scaling leads to two completely different solutions. In the first model, the horizontal distance is scaled with the roll gap length, $\hat{\ell}$, leading to a first-order pressure solution recovering the pressure hill and the shear stress depending on the pressure gradient. In the absence of the first-order correction for pressure, the solution is pretty much approximated by the leading-order solution, while the second-order correction slightly increases the through-thickness resolution of the solution. In this model, the significant shortcomings include a contradiction in force balance at the neutral point and an inability to capture the oscillations in stress and velocity fields.

In the second model, the horizontal distance is scaled with the sheet's initial half-thickness, $\hat{h}_0$. This approach results in constant leading-order pressure, while the first-order corrections to all stress and velocity components satisfy the wave equation. Consequently, the model predicts through-thickness oscillations. Yet, comparisons with FE simulations reveal several limitations of this model. Scaling the horizontal length with $\hat{h}_0$ prevents the model from capturing variations that develop over the long length of the roll gap, such as the pressure hill. Moreover, the linear wave pattern predicted by the model, which remains unchanged from the entrance to the exit, only loosely resembles the stress and velocity lobes observed in FE simulations.

The limitations of models based on single small or large length scales underscore the importance of considering the effective interaction of these scales. In fact, while the large length scale captures gradual changes in background parameters, the small length scale addresses the rapid propagation of waves. This interaction not only resolves the issue of fixed lobe shapes but also accounts for the expansion fan. Such interaction represents a fundamental physical characteristic of the problem and necessitates advanced mathematical techniques, which will be discussed in detail in the next chapter.

Chapter 3

Asymptotic model of perfectly plastic sheet rolling

Inaccuracies around simple models motivated considering an alternative model. With the same assumptions of a long thin roll gap and a comparably small Coulomb friction coefficient as the previous chapter, here we incorporate both a long length scale corresponding to the roll gap length and a short length scale associated with the workpiece thickness. The existence of effects on two different length scales in the same axial direction requires a different type of asymptotic analysis, termed multiple scales (Hinch, 1991), in which a fast scale provides rapid small variations about a solution which slowly evolves on the slow scale. The slowly varying solution is sometimes referred to as a slow manifold, invariant manifold, or centre manifold, and is a more general concept that is not unique to asymptotics (see, e.g. Roberts, 2015). These techniques of fast variation on a slowly changing solution have been applied to elastic beams (Valéry Roy et al., 2002), lubricating flows (Roberts, 1993), and acoustics (Brambley and Peake, 2008), but to our knowledge have not previously been used in the modelling of rolling.

In Section 3.1, the equations are scaled using the method of multiple scales. The equations are then solved in Section 3.2 by performing asymptotic analysis on the governing equations, and the solution is provided at different asymptotic orders. The assumption of a perfectly plastic material allows for solving the stress field independent of strain, and therefore the solutions for the stress and velocity fields are provided in separate subsections 3.2.1 and 3.2.2. In Section 3.3, the solutions are summarised and the computation methods are explained for stress and velocities in sections 3.3.1 and 3.3.2, respectively. Finally, these outputs are validated against FE simulation results for a range of parameters in Section 3.4, including against FE simulations using realistic material hardening parameters in Section 3.4.4. Implications of this work, and possibilities for future research, are then discussed in Section 3.5.

3.1 Scaling and non-dimensionalisation

3.1.1 Multiple scales

The large length scale, $z = \delta x$ (or equivalently, $z = \hat{x}/\hat{\ell}$), enables the representation of slowly-varying features. The shape of the rolls necessarily varies on this length scale only. The short length scale is the sheet thickness, which is not constant. The behaviour associated with this is expected to be localised, depending only on the local properties, and therefore on the local thickness. We therefore define the short-scale horizontal coordinate, n, using the current thickness rather than the initial thickness by making a WKB (Wenzel–Kramers–Brillouin, sometimes WKBJ or Liouville–Green) approximation (see, e.g. Hinch, 1991, section 7.5)

$$\frac{\mathrm{d}\hat{x}}{\mathrm{d}n} = \hat{h}(\hat{x}) \qquad \Rightarrow \qquad n = \int_0^{\hat{x}} \frac{\mathrm{d}\hat{X}}{\hat{h}(\hat{X})} = \int_0^{z} \frac{\mathrm{d}Z}{\delta h(Z)}. \tag{3.1}$$

We can now think of the roll gap being measured in terms of two lengths; one extending from $n = 0$ to $n \sim O(1/\delta)$, and the other, from $z = 0$ to $z = 1$. If the solution $\phi(x, y)$ is assumed to depend on the short length scale through n and the long length scale through z, then formally $\phi(x, y) = \phi(n, z, y)$, and

$$\frac{\partial \phi}{\partial x} = \frac{1}{h}\frac{\partial \phi}{\partial n} + \delta \frac{\partial \phi}{\partial z}. \tag{3.2}$$

To summarise, non-dimensionalised horizontal distances x, n and z are defined as

$$x = \hat{x}/\hat{h}_0 \tag{3.3a}$$

$$n = \int_0^{\hat{x}} \frac{\mathrm{d}\hat{X}}{\hat{h}(\hat{X})} \qquad \text{— the rapidly-changing variable} \tag{3.3b}$$

$$z = \hat{x}/\hat{\ell} = \delta x \qquad \text{— the slowly-changing variable.} \tag{3.3c}$$

3.1.2 Non-dimensional governing equations

Based on the non-dimensionalisation and the multiple-scales variables described above, the governing equations (2.1) and (2.2) become

$$\frac{1}{4}(\sigma_{xx}-\sigma_{yy})^2+\sigma_{xy}^2=1, \tag{3.4a}$$

$$\frac{1}{h(z)}\frac{\partial\sigma_{xx}}{\partial n}+\delta\frac{\partial\sigma_{xx}}{\partial z}+\frac{\partial\sigma_{xy}}{\partial y}=0, \tag{3.4b}$$

$$\frac{\partial\sigma_{yy}}{\partial y}+\frac{1}{h(z)}\frac{\partial\sigma_{xy}}{\partial n}+\delta\frac{\partial\sigma_{xy}}{\partial z}=0, \tag{3.4c}$$

$$\frac{1}{h(z)}\frac{\partial u}{\partial n}+\delta\frac{\partial u}{\partial z}+\frac{\partial v}{\partial y}=0, \tag{3.4d}$$

$$\frac{1}{h(z)}\frac{\partial u}{\partial n}+\delta\frac{\partial u}{\partial z}=\frac{1}{2}\lambda(\sigma_{xx}-\sigma_{yy}), \tag{3.4e}$$

$$\frac{\partial u}{\partial y}+\frac{1}{h(z)}\frac{\partial v}{\partial n}+\delta\frac{\partial v}{\partial z}=2\lambda\sigma_{xy}. \tag{3.4f}$$

The Coulomb friction condition applied on the roll surface $y=h(z)$ is expressed as

$$\delta\frac{\mathrm{d}h}{\mathrm{d}z}(\sigma_{yy}-\sigma_{xx})+\left(1-\delta^2\left(\frac{\mathrm{d}h}{\mathrm{d}z}\right)^2\right)\sigma_{xy}=\mp\delta\beta\left(\sigma_{yy}-2\delta\frac{\mathrm{d}h}{\mathrm{d}z}\sigma_{xy}+\delta^2\left(\frac{\mathrm{d}h}{\mathrm{d}z}\right)^2\sigma_{xx}\right), \tag{3.5}$$

In equation (3.5), the gradient of thickness is written as $\mathrm{d}h/\mathrm{d}x=\delta\mathrm{d}h/\mathrm{d}z$, indicating, firstly, that the shape of the rolls, h, necessarily varies on the large length scale z, and correspondingly, that the rate of change in thickness is small which is the result of a long and thin roll gap.

Assuming non-dimensionalised tensions per unit width $F_{\text{in/out}}$ are applied at the entrance and exit, the horizontal stress must satisfy

$$F_{\text{in/out}}=\int_{-h_{\text{in/out}}}^{h_{\text{in/out}}}\sigma_{xx}\Big|_{\text{in/out}}\,\mathrm{d}y, \tag{3.6}$$

where $h_{\text{in}}=1$ by the defined non-dimensionalisation, and h_{out} is half of the final thickness imposed by the rolls. Velocity and shear stress are also assumed to be prescribed at the entrance as,

$$u(z=n=0)=1, \qquad v(z=n=0)=0, \qquad \text{and} \qquad \sigma_{xy}(z=n=0)=\delta\tau_0, \tag{3.7}$$

where we assume that the imposed shear stress at the entrance is $O(\delta)$, and so $\tau_0=\hat{\tau}_0/(\delta\hat{\kappa})$ is the non-dimensionalisation used. This will turn out below to be the correct number of boundary conditions to apply, as will be seen once the solution is derived.

The no-flux constraint on the roll surface $y=h(z)$ leads to

$$v=\delta\frac{\mathrm{d}h}{\mathrm{d}z}u. \tag{3.8}$$

3.2 Asymptotic solution

In order to solve equations (3.4)-(3.8), the stress components, velocity components, and plastic parameter are expanded as asymptotic series in the small parameter δ,

$$\phi = \phi^{(0)}(z, y) + \delta\phi^{(1)}(n, z, y) + \delta^2\phi^{(2)}(n, z, y) + O(\delta^3), \tag{3.9}$$

where ϕ represents any of the mentioned variables. Note that the leading-order terms in all variables are set to be independent of n, which is in line with the slab method.

We now proceed to solve the problem. Anticipating that the stress is independent of velocity, we first derive a solution for the stress components, before returning to the velocities in Section 3.2.2.

3.2.1 Solving for the stresses

By asymptotically expanding in powers of δ and collecting similar terms, equations (3.4a), (3.4b) and (3.4c) become

$$\begin{aligned}\frac{1}{4}\left(\sigma_{xx}^{(0)} - \sigma_{yy}^{(0)}\right)^2 + {\sigma_{xy}^{(0)}}^2 + \delta\left(\frac{1}{2}(\sigma_{xx}^{(0)} - \sigma_{yy}^{(0)})(\sigma_{xx}^{(1)} - \sigma_{yy}^{(1)}) + 2\sigma_{xy}^{(0)}\sigma_{xy}^{(1)}\right)& \\ + \delta^2\left(\frac{1}{4}\left[(\sigma_{xx}^{(1)} - \sigma_{yy}^{(1)})^2 + 2(\sigma_{xx}^{(0)} - \sigma_{yy}^{(0)})(\sigma_{xx}^{(2)} - \sigma_{yy}^{(2)})\right] + {\sigma_{xy}^{(1)}}^2 + 2\sigma_{xy}^{(0)}\sigma_{xy}^{(2)}\right) + O(\delta^3) &= 1,\end{aligned} \tag{3.10a}$$

$$\frac{\partial\sigma_{xy}^{(0)}}{\partial y} + \delta\left(\frac{\partial\sigma_{xx}^{(0)}}{\partial z} + \frac{1}{h(z)}\frac{\partial\sigma_{xx}^{(1)}}{\partial n} + \frac{\partial\sigma_{xy}^{(1)}}{\partial y}\right) + \delta^2\left(\frac{\partial\sigma_{xx}^{(1)}}{\partial z} + \frac{1}{h(z)}\frac{\partial\sigma_{xx}^{(2)}}{\partial n} + \frac{\partial\sigma_{xy}^{(2)}}{\partial y}\right) + O(\delta^3) = 0, \tag{3.10b}$$

$$\frac{\partial\sigma_{yy}^{(0)}}{\partial y} + \delta\left(\frac{\partial\sigma_{yy}^{(1)}}{\partial y} + \frac{\partial\sigma_{xy}^{(0)}}{\partial z} + \frac{1}{h(z)}\frac{\partial\sigma_{xy}^{(1)}}{\partial n}\right) + \delta^2\left(\frac{\partial\sigma_{yy}^{(2)}}{\partial y} + \frac{\partial\sigma_{xy}^{(1)}}{\partial z} + \frac{1}{h(z)}\frac{\partial\sigma_{xy}^{(2)}}{\partial n}\right) + O(\delta^3) = 0. \tag{3.10c}$$

The Coulomb friction surface boundary conditions for stress from (3.5) becomes

$$\begin{aligned}\sigma_{xy}^{(0)} + \delta\left(\frac{\mathrm{d}h}{\mathrm{d}z}(\sigma_{yy}^{(0)} - \sigma_{xx}^{(0)}) + \sigma_{xy}^{(1)}\right) + \delta^2\left(\frac{\mathrm{d}h}{\mathrm{d}z}(\sigma_{yy}^{(1)} - \sigma_{xx}^{(1)}) + \sigma_{xy}^{(2)} - \left(\frac{\mathrm{d}h}{\mathrm{d}z}\right)^2\sigma_{xy}^{(0)}\right) + O(\delta^3)& \\ = \mp\delta\left(\beta\sigma_{yy}^{(0)}\right) \mp \delta^2\left(\beta\sigma_{yy}^{(1)} - 2\beta\frac{\mathrm{d}h}{\mathrm{d}z}\sigma_{xy}^{(0)}\right) + O(\delta^3).&\end{aligned} \tag{3.11}$$

Forward/backward tension per unit width at the roll-gap entrance/exit can be expanded as

$$F_{\text{in/out}} = \int_{-1/h_{\text{out}}}^{1/h_{\text{out}}} \sigma_{xx}^{(0)}\Big|_{\text{in/out}}\,\mathrm{d}y + \delta\int_{-1/h_{\text{out}}}^{1/h_{\text{out}}} \sigma_{xx}^{(1)}\Big|_{\text{in/out}}\,\mathrm{d}y + O(\delta^2). \tag{3.12}$$

Shear stress is assumed to have a known distribution at the entrance, $\delta\tau_0$, and hence

$$\sigma_{xy}(z = n = 0) = 0 + \delta\tau_0 + O(\delta^2), \tag{3.13}$$

Finally, symmetry condition implies that σ_{xy} is zero at all orders of δ about the centre line at $y = 0$.

Assuming the leading-order solution depends only on the slow-changing dimensionless horizontal variable z, we recover the same leading-order solution as explained in the previous chapter in Section 2.3; $\sigma_{xx}^{(0)} = 1 - p^{(0)}(z)$, and $\sigma_{yy}^{(0)} = -1 - p^{(0)}(z)$. The solution for $p^{(0)}(z)$ will be dictated by satisfying the friction expression at $O(\delta)$ on the surface, and thus the derivation is explained in the following section.

3.2.1.1 First-order solution

By taking the terms of order δ in the yield function (3.10a), and from the definition of hydrostatic pressure, $\sigma_{xx}^{(1)}$ and $\sigma_{yy}^{(1)}$ are given by

$$\sigma_{xx}^{(1)}(n, y, z) = \sigma_{yy}^{(1)}(n, y, z) = -p^{(1)}(n, y, z). \tag{3.14}$$

The local balance equations (3.10b) and (3.10c) at this order then become

$$\frac{\partial \sigma_{xy}^{(1)}}{\partial y} - \frac{1}{h(z)}\frac{\partial p^{(1)}}{\partial n} = \frac{\mathrm{d}p^{(0)}}{\mathrm{d}z} \qquad \text{and} \qquad \frac{\partial p^{(1)}}{\partial y} - \frac{1}{h(z)}\frac{\partial \sigma_{xy}^{(1)}}{\partial n} = 0. \tag{3.15}$$

These two equations give wave equations for $p^{(1)}$ and $\sigma_{xy}^{(1)}$, forced by the leading-order pressure gradient, with solution

$$p^{(1)} = A\Big(n + \frac{y}{h}, z\Big) + A\Big(n - \frac{y}{h}, z\Big) + D(z), \tag{3.16a}$$

$$\sigma_{xy}^{(1)} = A\Big(n + \frac{y}{h}, z\Big) - A\Big(n - \frac{y}{h}, z\Big) + y\frac{\mathrm{d}p^{(0)}}{\mathrm{d}z}, \tag{3.16b}$$

with n playing the role of the temporal variable and y the role of the spacial variable. The function $A(\xi, z)$ here is the as-yet-unknown wave solution, and we have made use of the fact that p is symmetric with respect to $y = 0$ axis and σ_{xy} is asymmetric. $D(z)$ is a constant of integration with respect to n and y, and so is only a function of the slow variable z.

With the general form of the solution for $\sigma_{xy}^{(1)}$ now known, we may now solve for $p^{(0)}$, which remained undetermined at leading order. At $O(\delta)$, the Coulomb friction equation (3.11) is

$$-2\frac{\mathrm{d}h}{\mathrm{d}z} + \sigma_{xy}^{(1)} \mp \beta(1 + p^{(0)}) = 0. \tag{3.17}$$

Substituting $\sigma_{xy}^{(1)}$ from (3.16b) into (3.17) and evaluating at $y = h$ results in

$$-2\frac{\mathrm{d}h}{\mathrm{d}z} \mp \beta(1+p^{(0)}) + h\frac{\mathrm{d}p^{(0)}}{\mathrm{d}z} = -\big(A(n+1,z) - A(n-1,z)\big), \tag{3.18}$$

where the left-hand side is a function of the slow variable z only and is independent of the fast variable n. We can therefore interpret (3.18) as a statement that A increases by a constant (with respect to n) when n increases by 2. If the constant is non-zero, A grows as a function of n, and by the end of the roll gap, $p^{(1)}$ or $\sigma_{xy}^{(1)}$ would be $O(n) = O(1/\delta)$ and the asymptotic ordering we assumed in deriving our equations would be broken (Hinch, 1991). Therefore, we require this constant to be zero, for $p^{(1)}$ and $\sigma_{xy}^{(1)}$ to remain bounded in terms of n, i.e.

$$A(n+1,z) - A(n-1,z) = 0. \tag{3.19}$$

We also note that (3.16) allows A to be shifted by any finite function of z, which is then absorbed into D; for simplicity we define D by setting

$$\int_{-1}^{1} A(\xi,z)\,\mathrm{d}\xi = 0. \tag{3.20}$$

Substituting (3.19) into (3.18) gives the same ODE for $p^{(0)}$ as derived by the simple asymptotic model, where $\hat{x} = \hat{\ell}z$, explained in Section 2.3;

$$-2\frac{\mathrm{d}h}{\mathrm{d}z} \mp \beta(1+p^{(0)}) + h\frac{\mathrm{d}p^{(0)}}{\mathrm{d}z} = 0. \tag{3.21}$$

Returning to the first-order solution presented in (3.16), we now consider the two unknown functions $A(\xi,z)$ and $D(z)$. Condition (3.19) establishes that, as a function of ξ, A is periodic with period 2. This means A needs only be found for $-1 < \xi < 1$ as z varies to be fully determined. Finding the z-dependency of the function A, as well as the unknown $D(z)$, requires further information which will be revealed in the next order of correction. However, the boundary condition at the entrance provides the initial conditions. Since F_{in} has already been satisfied at leading order, the first-order correction to it must be zero. Hence, according to equation (3.12) and using condition (3.20),

$$\int_{-h_0}^{h_0} \sigma_{xx}^{(1)}(y,\,0)\,\mathrm{d}y = -\int_{-1}^{1} \big(A(y,\,0) + A\,(-y,\,0) - D(0)\big)\,\mathrm{d}y = 0 \quad \Rightarrow \quad D(0) = 0, \tag{3.22}$$

which is an initial condition for $D(z)$. Unlike the leading order, where the average force was sufficient for the stress boundary conditions, at this order, the force distribution must be specified. We therefore assume a known initial stress distribution at the entrance, given by $\sigma_{xx}^{(1)}(y,0)$ and $\tau_0(y)$. At $z=0$, (3.14) and (3.16) then give

$$\sigma_{xx}^{(1)}(y,0) = -A(y,0) - A(-y,0), \tag{3.23a}$$

$$\tau_0(y) = A(y,0) - A(-y,0) + y\frac{\mathrm{d}p^{(0)}}{\mathrm{d}z}. \tag{3.23b}$$

and consequently,

$$A\left(y,\,0\right) = \frac{1}{2}\Big(\tau_0(y) - \sigma_{xx}^{(1)}(y,0)\Big) - \frac{1}{2}y\left.\frac{\mathrm{d}p^{(0)}}{\mathrm{d}z}\right|_{z=0}. \tag{3.24}$$

Equation (3.24) gives an initial condition for A at $z=0$. The choice of initial stresses will be discussed later in Section 3.3.1.

3.2.1.2 Second-order solution

The solution is continued to this order of correction with the goal of finding the unknown parameters $A(\xi,z)$ and $D(z)$ from the previous order. Using the stress equations in Section 3.2.1 at $O(\delta^2)$, and after significant algebra detailed in Appendix A1, the following expression is derived:

$$2h\frac{\partial A(n+1,z)}{\partial z} + \frac{\partial}{\partial n}\Big(A(n+1,z)^2\Big) + \left(h\frac{\mathrm{d}p^{(0)}}{\mathrm{d}z} \mp 2\beta\right)A(n+1,z) - h\frac{\mathrm{d}D}{\mathrm{d}z} \mp \beta D(z) = 0. \tag{3.25}$$

By integrating (3.25) between $n=-2$ and $n=0$ and imposing (3.20), we arrive at

$$-h\frac{\mathrm{d}D}{\mathrm{d}z} \mp \beta D(z) = 0. \tag{3.26}$$

Since $D(0) = 0$ from (3.22), we conclude that $D(z) \equiv 0$. With this, equation (3.25) then gives an evolution equation for how A varies as z is increased;

$$2h\frac{\partial A(\xi,z)}{\partial z} + \frac{\partial}{\partial \xi}\Big(A(\xi,z)^2\Big) + \left(h\frac{\mathrm{d}p^{(0)}}{\mathrm{d}z} \mp 2\beta\right)A(\xi,z) = 0. \tag{3.27}$$

This PDE cannot be solved exactly, so a numerical approach is needed. We can simplify the numerics required by introducing variables $\alpha_1(z)$, $T(z)$ and $\omega(\xi,T)$, as shown in Appendix A2;

$$T = \int^z \frac{\alpha_1}{h(\tilde{z})^2}\,\mathrm{d}\tilde{z}, \qquad \omega\big(\xi,T(z)\big) = \frac{A(\xi,z)}{(\alpha_1/h)}, \tag{3.28a}$$

$$\text{and} \qquad \alpha_1 = \exp\left\{\int_0^z \Big[\mp\frac{\beta}{2h(\tilde{z})}(p^{(0)}(\tilde{z})-1)\Big]\mathrm{d}\tilde{z}\right\},$$

$$\Rightarrow \qquad \frac{\partial\omega}{\partial T} + \frac{1}{2}\frac{\partial}{\partial\xi}\Big(\omega^2\Big) = 0. \tag{3.28b}$$

Equation (3.28b) is a standard Burger's equation which is especially advantageous as it enables the effective handling of the evolution of discontinuities in the form of shocks or expansion fans.

Once (3.28b) has been solved with suitable initial conditions for ω and hence A, the correction to the pressure, $p^{(1)}$, and all the components of the Cauchy stress, $\sigma_{xx}^{(1)}$, $\sigma_{yy}^{(1)}$ and $\sigma_{xy}^{(1)}$, can be calculated by evaluating (3.16a), (3.14) and (3.16b) respectively. It should be noted that, since the boundary condition changes on the surface at the neutral point, equation (3.28b) should be solved separately for the entrance and exit regions, with the two regions connected at the neutral point. The behaviour in the vicinity of this neutral point is discussed further in the next section.

3.2.1.3 Behaviour near the neutral point

The shear stress $\sigma_{xy}^{(1)}$, given in equation (3.16b), is formed of two components: the first component, involving A, will be seen to cause a wave pattern, while the second one, $y\,\mathrm{d}p^{(0)}/\mathrm{d}z$, causes a discontinuity in shear stress across a vertical line running through the thickness of the sheet, as explained in 2.3.2.1. To prevent this, we require σ_{xy} to be continuous in z. Introducing the notation $(-)$ and $(+)$ to denote variables to the left and right of the neutral point respectively, near the neutral point $z = z_{\mathrm{N}}$ we require $\sigma_{xy}^{(1-)} = \sigma_{xy}^{(1+)}$. Therefore, from (3.16b) we obtain,

$$\begin{aligned} A^{(-)}\left(n_{\mathrm{N}} + \frac{y}{h_{\mathrm{N}}}, z_{\mathrm{N}}\right) - A^{(-)}\left(n_{\mathrm{N}} - \frac{y}{h_{\mathrm{N}}}, z_{\mathrm{N}}\right) \qquad & \\ + \frac{h_{\mathrm{N}}}{2}\left[\left(n + \frac{y}{h_{\mathrm{N}}}, z_{\mathrm{N}}\right) - \left(n - \frac{y}{h_{\mathrm{N}}}, z_{\mathrm{N}}\right)\right] \frac{\mathrm{d}p^{(0-)}}{\mathrm{d}z}\bigg|_{z=z_{\mathrm{N}}} & \\ = A^{(+)}\left(n_{\mathrm{N}} + \frac{y}{h_{\mathrm{N}}}, z_{\mathrm{N}}\right) - A^{(+)}\left(n_{\mathrm{N}} - \frac{y}{h_{\mathrm{N}}}, z_{\mathrm{N}}\right) & \\ + \frac{h_{\mathrm{N}}}{2}\left[\left(n + \frac{y}{h_{\mathrm{N}}}, z_{\mathrm{N}}\right) - \left(n - \frac{y}{h_{\mathrm{N}}}, z_{\mathrm{N}}\right)\right] \frac{\mathrm{d}p^{(0+)}}{\mathrm{d}z}\bigg|_{z=z_{\mathrm{N}}}. & \qquad (3.29) \end{aligned}$$

Solving (3.29) and applying (3.21) yields

$$\begin{aligned} A^{(+)}(\xi, z_{\mathrm{N}}) = A^{(-)}(\xi, z_{\mathrm{N}}) + \frac{h_{\mathrm{N}}}{2}\left(\frac{\mathrm{d}p^{(0-)}}{\mathrm{d}z}\bigg|_{z=z_{\mathrm{N}}} - \frac{\mathrm{d}p^{(0+)}}{\mathrm{d}z}\bigg|_{z=z_{\mathrm{N}}}\right) & \\ = A^{(-)}(\xi, z_{\mathrm{N}}) + \beta\xi\left(1 + p^{(0)}(z_{\mathrm{N}})\right). & \qquad (3.30) \end{aligned}$$

In this derivation, it is assumed that there is no $O(\delta)$ correction to the location of the neutral point, and that the change from $A^{(-)}$ to $A^{(+)}$ happens abruptly. These assumptions are validated through a more comprehensive calculation of an inner region close to the neutral point, as detailed in the rest of this section.

We introduce a new coordinate X measuring distance near the neutral point,

$$z = z_{\mathrm{N}} + \delta X, \tag{3.31}$$

where z_{N} is the location of the neutral point obtained from the leading-order solution. We consider the neutral point to actually occur at $X = X_{\mathrm{N}}$, where X_{N} is an $O(\delta)$ correction to the location of the neutral point. From (3.31), it can be seen that X varies on the same length scale as the workpiece thickness, and so is comparable to the original x coordinate in (3.3a). Within the inner region, there is only one length scale, and so we do not need the multiple-scales variables z and n; stresses are only functions of X and y. Therefore, the governing equations are the same as those explained in the previous chapter in Section 2.4, with the same leading-order and first-order solution. Here we summarised the solution using the label "inner" to distinguish variables in the inner region from those in the outer region.

At leading order, $\sigma^{(0)}_{xy_{\mathrm{inner}}}$ is zero similar to the outer region; therefore, from the yield criterion,

$$\sigma^{(0)}_{xx_{\mathrm{inner}}} = 1 - p^{(0)}_{\mathrm{inner}} \qquad \text{and} \qquad \sigma^{(0)}_{yy_{\mathrm{inner}}} = -1 - p^{(0)}_{\mathrm{inner}}, \tag{3.32}$$

where $p^{(0)}_{\mathrm{inner}}$ is constants.

At $O(\delta)$, from the yield condition,

$$\sigma^{(1)}_{xx_{\mathrm{inner}}} - \sigma^{(1)}_{yy_{\mathrm{inner}}} = 0 \qquad \Rightarrow \qquad \sigma^{(1)}_{xx_{\mathrm{inner}}} = \sigma^{(1)}_{yy_{\mathrm{inner}}} = -p^{(1)}_{\mathrm{inner}}, \tag{3.33}$$

and, from local balance equations,

$$p^{(1)}_{\mathrm{inner}} = G\left(\frac{X}{h_{\mathrm{N}}} + \frac{y}{h_{\mathrm{N}}}\right) + G\left(\frac{X}{h_{\mathrm{N}}} - \frac{y}{h_{\mathrm{N}}}\right), \quad \sigma^{(1)}_{xy_{\mathrm{inner}}} = G\left(\frac{X}{h_{\mathrm{N}}} + \frac{y}{h_{\mathrm{N}}}\right) - G\left(\frac{X}{h_{\mathrm{N}}} - \frac{y}{h_{\mathrm{N}}}\right), \tag{3.34}$$

where $h_{\mathrm{N}} = h(z_{\mathrm{N}})$ is the half-thickness at the unperturbed neutral point and G is an as-yet-unknown wave. Substituting $\sigma^{(1)}_{xy_{\mathrm{inner}}}$ into the friction equation at $O(\delta)$ gives the periodicity constraint on G (with $\mp = \operatorname{sgn}(X - X_{\mathrm{N}})$)

$$-2\left.\frac{\mathrm{d}h}{\mathrm{d}z}\right|_{z=z_N} + \left[G\left(\frac{X}{h_{\mathrm{N}}} + 1\right) - G\left(\frac{X}{h_{\mathrm{N}}} - 1\right)\right] \mp \beta(1 + p^{(0)}_{\mathrm{inner}}) = 0. \tag{3.35}$$

This inner solution above should match with the previously derived outer solutions, as $X \to \pm\infty$. Therefore we may write,

$$\begin{aligned} p &= p^{(0\mp)}(y, z_\mathrm{N} + \delta X) + \delta p^{(1\mp)}\big(n_\mathrm{N} + X/h_\mathrm{N} + O(\delta), y, z_\mathrm{N} + \delta X\big) + O\big(\delta^2\big) \\ &= p^{(0)}(z_\mathrm{N}) + \delta\Bigg[A^{(\mp)}\bigg(n_\mathrm{N} + \frac{X}{h_\mathrm{N}} + \frac{y}{h_\mathrm{N}}, z_\mathrm{N}\bigg) + A^{(\mp)}\bigg(n_\mathrm{N} + \frac{X}{h_\mathrm{N}} - \frac{y}{h_\mathrm{N}}, z_\mathrm{N}\bigg) \\ &\qquad + X\frac{dp^{(0\mp)}(z_\mathrm{N})}{dz}\Bigg] + O\big(\delta^2\big), \end{aligned} \tag{3.36a}$$

$$\begin{aligned} \sigma_{xy} &= \sigma_{xy}^{(1\mp)}\big(n_\mathrm{N} + X/h_\mathrm{N} + O(\delta), y, z_\mathrm{N} + \delta X\big) + O\big(\delta^2\big) \\ &= \delta\Bigg[A^{(\mp)}\bigg(n_\mathrm{N} + \frac{X}{h_\mathrm{N}} + \frac{y}{h_\mathrm{N}}, z_\mathrm{N}\bigg) - A^{(\mp)}\bigg(n_\mathrm{N} + \frac{X}{h_\mathrm{N}} - \frac{y}{h_\mathrm{N}}, z_\mathrm{N}\bigg) + y\frac{dp^{(0\mp)}(z_\mathrm{N})}{dz}\Bigg] + O\big(\delta^2\big), \end{aligned} \tag{3.36b}$$

where $p^{(1\mp)}$ and $\sigma_{xy}^{(1\mp)}$ are taken from equation (3.16), $p^{(0\mp)}$ satisfies (3.21), and $A^{(\mp)}(\xi, z)$ is the function $A(\xi, z)$ from the outer solution to the left $(-)$ or right $(+)$ of the neutral point. Note that $p^{(0+)}(z_\mathrm{N}) = p^{(0-)}(z_\mathrm{N})$, as this is how the neutral point z_N is chosen, but that $\mathrm{d}p^{(0+)}/\mathrm{d}z \neq \mathrm{d}p^{(0-)}/\mathrm{d}z$ at $z = z_\mathrm{N}$ (see 3.21).

p and σ_{xy} in equation (3.36) should match the solution in the inner. At leading order, the comparison gives $p_\mathrm{inner}^{(0)} = p^{(0)}(z_\mathrm{N})$, and confirms that $\sigma_{xy\mathrm{inner}}^{(0)} = 0$. Matching the $O(\delta)$ part of equation (3.36) before the neutral point (superscript $(\mp) = (-)$) with equation (3.34) gives

$$G(\xi) = A^{(-)}(n_\mathrm{N} + \xi, z_\mathrm{N}) + \frac{h_\mathrm{N}}{2}\xi\frac{\mathrm{d}p^{(0-)}}{\mathrm{d}z}\Big|_{z=z_\mathrm{N}} \qquad \text{for} \qquad \xi < \frac{X_N}{h_N} + 1, \tag{3.37}$$

where, $\mp = -$ requires $X < X_N$, and hence $\xi < X_N/h_N + 1$, as indicated in (3.37).

Similarly, we may exactly match $\sigma_{xy_\mathrm{inner}}^{(1)}$ and $p_\mathrm{inner}^{(1)}$ given in equation (3.34) with the $O(\delta)$ part of equation (3.36) with superscript $(\mp) = (+)$ by taking

$$G(\xi) = A^{(+)}(n_\mathrm{N} + \xi, z_\mathrm{N}) + \frac{h_\mathrm{N}}{2}\xi\frac{\mathrm{d}p^{(0+)}}{\mathrm{d}z}\Big|_{z=z_\mathrm{N}} \qquad \text{for} \qquad \xi > \frac{X_N}{h_N} - 1, \tag{3.38}$$

where $\mp = +$ requires $X > X_N$, and hence $\xi > X_N/h_N - 1$, as indicated in (3.38). Note that by substituting the solutions (3.37) and (3.37) for $G(\xi)$ into equation (3.35) it can be shown that $G(\xi)$ exactly satisfies the periodicity constraint.

In order to satisfy both (3.37) and (3.38), for $X_N/h_N - 1 < \xi < X_N/h_N + 1$ we must have

$$G(\xi) = A^{(-)}(n_{\mathrm{N}} + \xi, z_{\mathrm{N}}) + \frac{h_{\mathrm{N}}}{2}\xi \frac{\mathrm{d}p^{(0-)}}{\mathrm{d}z}\Big|_{z=z_{\mathrm{N}}} = A^{(+)}(n_{\mathrm{N}} + \xi, z_{\mathrm{N}}) + \frac{h_{\mathrm{N}}}{2}\xi \frac{\mathrm{d}p^{(0+)}}{\mathrm{d}z}\Big|_{z=z_{\mathrm{N}}} \tag{3.39a}$$

$$\begin{aligned} \Rightarrow \qquad A^{(+)}(n_{\mathrm{N}} + \xi, z_{\mathrm{N}}) &= A^{(-)}(n_{\mathrm{N}} + \xi, z_{\mathrm{N}}) + \frac{h_N}{2}\xi \left[\frac{\mathrm{d}p^{(0-)}}{\mathrm{d}z}\Big|_{z=z_{\mathrm{N}}} - \frac{\mathrm{d}p^{(0+)}}{\mathrm{d}z}\Big|_{z=z_{\mathrm{N}}} \right] \\ &= A^{(-)}(n_{\mathrm{N}} + \xi, z_{\mathrm{N}}) + \beta\xi(1 + p^{(0)}(z_N)). \end{aligned} \tag{3.39b}$$

In the outer region, the condition (3.20) results in $\int A^{(\mp)}(\xi)\,\mathrm{d}\xi = 0$. Therefore,

$$0 = \int A^{(+)}(\xi)\,\mathrm{d}\xi = \int\limits_{X_{\mathrm{N}}/h_{\mathrm{N}}-1}^{X_{\mathrm{N}}/h_{\mathrm{N}}+1} A^{(-)}(n_{\mathrm{N}} + \xi)\,\mathrm{d}\xi + \int\limits_{X_{\mathrm{N}}/h_{\mathrm{N}}-1}^{X_{\mathrm{N}}/h_{\mathrm{N}}+1} \beta\xi\Big(p^{(0)}(z_{\mathrm{N}}) + 1\Big)\,\mathrm{d}\xi = 2\beta\Big(p^{(0)}(z_{\mathrm{N}}) + 1\Big)\frac{X_{\mathrm{N}}}{h_{\mathrm{N}}}. \tag{3.40}$$

In order for this equality to be satisfied, we must take $X_{\mathrm{N}} = 0$. This means there is no $O(\delta)$ correction to the location of the neutral point, and the neutral point is located at $z = z_{\mathrm{N}}$, found from equation (3.21) for $p^{(0)}$ in the outer region. Equation (3.39b) thus gives the connection between the solutions to the left and right of the neutral point which is the same equation given in (3.30) with $X_{\mathrm{N}} = 0$.

From equations (3.30) the full solution of $A(\xi, z)$ in the entire roll gap can be achieved. In fact, $A^{(-)}$ is known completely from the initial conditions (3.24) at $z = 0$ and then solving equation (3.27) or (3.28b) for $0 < z < z_{\mathrm{N}}$. Since both $A^{(-)}$ and $A^{(+)}$ are periodic in ξ with period 2, equations (3.30) completely define $A^{(+)}(\xi, z_{\mathrm{N}})$ in terms of $A^{(-)}$, from which equation (3.27) or (3.28b) can be used to evolve $A^{(+)}$ for $z_{\mathrm{N}} < z < 1$, giving the full solution in the entire roll gap.

3.2.2 Solving for the velocities

With the stresses determined in Section 3.2.1, the next step is to compute the velocity field. The approach here is the same as what is used for the stresses above. By asymptotically expanding equations (3.4d), (3.4e) and (3.4f) in successive powers of δ

and collecting like terms we obtain,

$$\frac{\partial v^{(0)}}{\partial y}+\delta\left(\frac{\partial u^{(0)}}{\partial z}+\frac{1}{h(z)}\frac{\partial u^{(1)}}{\partial n}+\frac{\partial v^{(1)}}{\partial y}\right)+\delta^2\left(\frac{\partial u^{(1)}}{\partial z}+\frac{1}{h(z)}\frac{\partial u^{(2)}}{\partial n}+\frac{\partial v^{(2)}}{\partial y}\right)+O(\delta^3)=0, \tag{3.41a}$$

$$\begin{aligned}\delta\left(\frac{\partial u^{(0)}}{\partial z}+\frac{1}{h(z)}\frac{\partial u^{(1)}}{\partial n}\right)+\delta^2\left(\frac{\partial u^{(1)}}{\partial z}+\frac{1}{h(z)}\frac{\partial u^{(2)}}{\partial n}\right)+O(\delta^3)&=\frac{1}{2}\lambda^{(0)}\left(\sigma_{xx}^{(0)}-\sigma_{yy}^{(0)}\right)\\&+\frac{\delta}{2}\left(\lambda^{(0)}\left(\sigma_{xx}^{(1)}-\sigma_{yy}^{(1)}\right)+\lambda^{(1)}\left(\sigma_{xx}^{(0)}-\sigma_{yy}^{(0)}\right)\right)+O(\delta^2),\end{aligned} \tag{3.41b}$$

$$\begin{aligned}&\frac{\partial u^{(0)}}{\partial y}+\delta\left(\frac{\partial u^{(1)}}{\partial y}+\frac{\partial v^{(0)}}{\partial z}+\frac{1}{h(z)}\frac{\partial v^{(1)}}{\partial n}\right)+\delta^2\left(\frac{\partial u^{(2)}}{\partial y}+\frac{\partial v^{(1)}}{\partial z}+\frac{1}{h(z)}\frac{\partial v^{(2)}}{\partial n}\right)+O(\delta^3)\\&\quad=2\sigma_{xy}^{(0)}\lambda^{(0)}+2\delta\left(\lambda^{(0)}\sigma_{xy}^{(1)}+\lambda^{(1)}\sigma_{xy}^{(0)}\right)+2\delta^2\left(\lambda^{(0)}\sigma_{xy}^{(2)}+\lambda^{(1)}\sigma_{xy}^{(1)}+\lambda^{(2)}\sigma_{xy}^{(0)}\right)+O(\delta^3).\end{aligned} \tag{3.41c}$$

The surface boundary condition for velocity from (3.8) is

$$v^{(0)}+\delta v^{(1)}+\delta^2 v^{(2)}+O(\delta^3)=\delta\frac{\mathrm{d}h}{\mathrm{d}z}\left(u^{(0)}+\delta u^{(1)}\right)+O(\delta^3). \tag{3.42}$$

For the velocity initial condition, at $z=0$, we set $v^{(1)}\equiv u^{(1)}\equiv 0$ for consistency with our assumptions. This reflects that the sheet has undergone negligible elastic deformation at the entrance, and there is no plastic deformation outside the roll gap, so that the sheet enters the roll gap as a solid body motion. Thus, equation (3.7) is expanded as

$$u(z=n=0)=1+\delta(0)+\delta^2(0)+O(\delta^3)\quad\text{and}\quad v(z=n=0)=0+\delta(0)+\delta^2(0)+O(\delta^3). \tag{3.43}$$

Finally, symmetry condition implies v is zero at all orders of δ about the centre line at $y=0$.

Assuming the leading-order solution depends only on the large length scale z, the same leading-order solutions are recovered as those explained in the previous chapter in Section 2.3; $u^{(0)}(z)=1/h(z)$, and $v^{(0)}=0$. The leading-order plastic multiplier, $\lambda^{(0)}$, is also determined to be zero since $\hat{\lambda}$ is non-dimensionalised respect to $\hat{h}_0$ as $\hat{U}_0/(\hat{h}_0\hat{\kappa})$.

3.2.2.1 First-order solution

By only taking terms of order δ, the continuity equation (3.41a) and the shear flow-rule equation (3.41c) become, respectively,

$$\frac{\partial v^{(1)}}{\partial y}+\frac{1}{h}\frac{\partial u^{(1)}}{\partial n}=-\frac{\partial u^{(0)}}{\partial z}\qquad\text{and}\qquad\frac{\partial u^{(1)}}{\partial y}+\frac{1}{h}\frac{\partial v^{(1)}}{\partial n}=0. \tag{3.44}$$

Therefore, similar to the stresses at this order, $u^{(1)}$ and $v^{(1)}$ satisfy a wave equation with the general solution

$$u^{(1)}=B\Big(n+\frac{y}{h},z\Big)+B\Big(n-\frac{y}{h},z\Big), \tag{3.45a}$$

$$v^{(1)}=-\Big[B\Big(n+\frac{y}{h},z\Big)-B\Big(n-\frac{y}{h},z\Big)\Big]+\frac{y}{h^2}\frac{\mathrm{d}h}{\mathrm{d}z}, \tag{3.45b}$$

where $B(\xi,z)$ is an unknown function. The solution above has accounted for the symmetry of u and asymmetry of v with respect to the centre line. Also, similar to $p^{(1)}$, the shift in $u^{(1)}$ is set to zero from averaged mass balance and setting

$$\int_{-1}^{1}B(\xi,z)\,\mathrm{d}\xi=0, \tag{3.46}$$

By substituting the solution for $v^{(1)}$ into the tension flow-rule equation (3.41b), $\lambda^{(1)}$ is found to be

$$\lambda^{(1)}=-\frac{\partial v^{(1)}}{\partial y}=\frac{1}{h}\Big[B'\Big(n+\frac{y}{h},z\Big)+B'\Big(n-\frac{y}{h},z\Big)\Big]-\frac{1}{h^2}\frac{\mathrm{d}h}{\mathrm{d}z}, \tag{3.47}$$

with prime denoting $\partial/\partial\xi$. As a result of the no-penetration boundary condition on the surface (3.42),

$$v^{(1)}(y=h)=\frac{\mathrm{d}h}{\mathrm{d}z}u^{(0)}\qquad\Rightarrow\qquad B(n+1,z)=B(n-1,z), \tag{3.48}$$

which implies that $B(\xi,z)$ is periodic with periodicity 2, similarly to $A(\xi,z)$ for the stresses. This means B needs only be defined for $-1<\xi<1$ for each value of z. Initial condition for $B(\xi,z)$ at the entrance, is given by setting $n=z=0$ in (3.45) and subtracting equation (3.45b) from (3.45a). By imposing zero first-order velocities at the entrance from (3.43), the initial conditions for $B(\xi,z)$ is given by

$$B(y,\,0)=\frac{y}{2}\left.\frac{\mathrm{d}h}{\mathrm{d}z}\right|_{z=0}. \tag{3.49}$$

Additional information is required to determine the evolution of this initial condition with respect to z (i.e. the z dependency of the function B), which is discussed below.

3.2.2.2 Second-order solution

The continuity equation (3.41a) and the shear flow-rule equation (3.41c), at order δ^2 are, respectively,

$$\frac{\partial v^{(2)}}{\partial y} + \frac{1}{h}\frac{\partial u^{(2)}}{\partial n} = -\frac{\partial u^{(1)}}{\partial z}, \tag{3.50a}$$

$$\frac{\partial u^{(2)}}{\partial y} + \frac{1}{h}\frac{\partial v^{(2)}}{\partial n} = -\frac{\partial v^{(1)}}{\partial z} + 2\lambda^{(1)}\sigma_{xy}^{(1)}. \tag{3.50b}$$

As for the stresses and the first-order velocities, these equations form a coupled wave equation for $u^{(2)}$ and $v^{(2)}$. Following the same procedure as for the second-order stresses, solving for $u^{(2)}$ and $v^{(2)}$ is detailed in Appendix A3. Avoiding a growing term, as for the stresses, results in an evolution equation in z for B given by

$$\frac{\partial B(n+1,z)}{\partial z} - \frac{1}{h^2}\frac{\mathrm{d}h}{\mathrm{d}z}A(n+1,z) - \left(\frac{1}{2}\frac{\mathrm{d}p^{(0)}}{\mathrm{d}z} - \frac{1}{h}\frac{\mathrm{d}h}{\mathrm{d}z}\right)B(n+1,z) + \frac{1}{h}B'(n+1,z)A(n+1,z) = 0. \tag{3.51}$$

This equation can be simplified by defining $\alpha_2(z) = \exp\left\{\frac{1}{2}p^{(0)}\right\}$, to give,

$$\frac{\partial}{\partial z}\left(\frac{B(\xi,z)}{(\alpha_2/h)}\right) + \frac{A(\xi,z)}{h}\frac{\partial}{\partial \xi}\left(\frac{B(\xi,z)}{(\alpha_2/h)}\right) = \frac{1}{h\alpha_2}\frac{\mathrm{d}h}{\mathrm{d}z}A(\xi,z). \tag{3.52}$$

This is a type of advection equation with a velocity of $A(\xi,z)/h$. It is, however, more convenient to solve the equation if the excitation term on the right-hand side can be included inside the derivatives. Moreover, when compared to Burger's equation for the stresses (3.28b), the above equation can be rewritten to have the same advection speed $\omega(\xi,z)$. The derivation of this rearranged equation is also given in Appendix A4, finally yielding the genuine advection equation

$$\frac{\partial}{\partial T}\left(\frac{B}{(\alpha_2/h)} - Q\omega\right) + \omega\frac{\partial}{\partial \xi}\left(\frac{B}{(\alpha_2/h)} - Q\omega\right) = 0, \quad \text{where} \quad Q(z) = \int_0^z \frac{\alpha_1}{\alpha_2 h^2}\frac{\mathrm{d}h}{\mathrm{d}\tilde{z}}d\tilde{z}. \tag{3.53}$$

Equation (3.53) or (3.52) can be solved with a suitable initial condition, and the solution B can be subsequently used to calculate $u^{(1)}$, $v^{(1)}$ and $\lambda^{(1)}$ by evaluating (3.45a), (3.45b) and (3.47) respectively.

3.3 Computing the asymptotic solutions

Above the governing equations for the various components of stress and strain have been derived that can be integrated through the roll gap, either analytically or semi-analytically, starting from initial conditions at the roll-gap entrance and matching some conditions at the roll-gap exit. This section summarises the solutions obtained for stresses and velocities separately and outlines a straightforward numerical procedure for performing these calculations.

3.3.1 Stresses

The stress profiles in terms of horizontal distance x, and vertical distance y are written in terms of horizontal scales $n = \int_0^x 1/h \, \mathrm{d}x$ and $z = \delta x$ as

$$\begin{aligned} p &= p^{(0)}(z) + \delta \left[A\Big(n + \frac{y}{h}, z\Big) + A\Big(n - \frac{y}{h}, z\Big) \right] + O(\delta^2) && \text{(3.54a)} \\ \sigma_{xy} &= \quad 0 \quad + \delta \left[A\Big(n + \frac{y}{h}, z\Big) - A\Big(n - \frac{y}{h}, z\Big) + y \frac{\mathrm{d}p^{(0)}}{\mathrm{d}z} \right] + O(\delta^2), && \text{(3.54b)} \\ \sigma_{xx} &= \quad 1 - p, && \text{(3.54c)} \\ \sigma_{yy} &= -1 - p. && \text{(3.54d)} \end{aligned}$$

The leading-order pressure $p^{(0)}(z)$ is given by (3.21). This is the same equation derived by the simple asymptotic model, where $\hat{x} = \hat{\ell} z$, explained in 2.3.

The first-order wave-like oscillatory function $A(\xi, z)$, in the set of equations (3.54), obeys Burger's equation once suitably rescaled,

$$A(\xi, z) = \frac{\alpha_1}{h} \omega\big(\xi, T(z)\big), \quad \frac{\partial \omega}{\partial T} + \frac{1}{2} \frac{\partial}{\partial \xi} \Big(\omega^2\Big) = 0 \qquad \text{for} \quad -1 < \xi < 1, \tag{3.55a}$$

$$T = \int^z \frac{\alpha_1}{h(\bar{z})^2} \, \mathrm{d}\bar{z}, \qquad \alpha_1 = \exp\left\{ \int_0^z \Big(\mp \frac{\beta}{2h(\tilde{z})} \big(p^{(0)}(\tilde{z}) - 1\big) \Big) \mathrm{d}\tilde{z} \right\}, \tag{3.55b}$$

where A and therefore ω are periodic in ξ such that

$$A(\xi + 1, z) = A(\xi - 1, z). \tag{3.56}$$

Due to periodicity, it is sufficient to solve Burger's equation for $-1 < \xi < 1$. Burger's equation (3.55) is solved first from the entrance at $z = 0$ to the neutral point at $z = z_{\mathrm{N}}$ to give $A^{(-)}$, and is then solved again from $z = z_{\mathrm{N}}$ onwards with the new initial condition at the neutral point to give $A^{(+)}$:

$$A(\xi, z) = \begin{cases} A^{(-)}(\xi, z) \quad \text{for } z < z_{\mathrm{N}} \quad \text{with} \quad A^{(-)}(\xi, 0) = \dfrac{1}{2}\Big(\tau_0(\xi) - \sigma_{xx}^{(1)}(\xi, 0)\Big) - \dfrac{1}{2} \xi \dfrac{\mathrm{d}p^{(0)}}{\mathrm{d}z}\bigg|_{z=0} \\ \\ A^{(+)}(\xi, z) \quad \text{for } z > z_{\mathrm{N}} \quad \text{with} \quad A^{(+)}(\xi, z_{\mathrm{N}}) = A^{(-)}(\xi, z_{\mathrm{N}}) + \beta \xi \big(p^{(0)}(z_{\mathrm{N}}) + 1\big). \end{cases} \tag{3.57}$$

For the initial condition at $n = z = 0$ in (3.57), the simplest assumption is that $\sigma_{xx}^{(1)}$ is zero and $\tau_0(y)$ is linear in y at the entrance; taking $\tau_0(y) = -1.2y$ was found to give a good comparison for all rolling parameters considered here. This implies a situation where all material points are affected the same by the inlet tension, and the shear stress linearly increases from zero at the symmetry line to its maximum value at the surface. While this maximum shear stress can be chosen to give good agreement with FE results, as will be seen below, an improved estimation is obtained by allowing $\sigma_{xx}^{(1)}$ to vary quadratically (but with average value zero to maintain the same inlet tension according to (3.12)). Both scenarios are compared with FE results in Section 3.4. Once $A^{(-)}$ is completely solved from (3.55) with the initial conditions at $n = z = 0$, the solution at z_{N} is used to modify the initial condition at the neutral point. This new initial condition is then used to solve $A^{(+)}$ from the neutral point to the exit. $A^{(-)}$ and $A^{(+)}$ together give the full solution in the entire roll gap.

Burger's equation (3.55) is solved with the finite volume method in Matlab, and a limiter is applied to ensure that the numerical solution does not develop new extrema. While the periodicity of A in ξ means that A will have discontinuities (e.g. at $\xi = \pm 1$), these discontinuities form an expansion fan in the Burger's equation solution, and so are not problematic. Using the unoptimised Matlab code, solving for all stresses takes of the order of a couple of seconds on a standard laptop.

3.3.2 Velocities

The velocity profiles are given by,

$$u = \frac{1}{h} + \delta \left[B\Big(n + \frac{y}{h}, z\Big) + B\Big(n - \frac{y}{h}, z\Big) \right] + O(\delta^2), \tag{3.58a}$$

$$v = \;0\; - \delta \left[B\Big(n + \frac{y}{h}, z\Big) - B\Big(n - \frac{y}{h}, z\Big) - y\frac{\mathrm{d}h/\mathrm{d}z}{h^2} \right] + O(\delta^2), \tag{3.58b}$$

where the leading-order slab-like behaviour is controlled directly by the roll-gap thickness imposed by the rolls, and the wave-like oscillatory correction obeys,

$$\frac{\partial}{\partial T}\left(\frac{B}{(\alpha_2/h)} - Q\omega\right) + \omega\frac{\partial}{\partial \xi}\left(\frac{B}{(\alpha_2/h)} - Q\omega\right) = 0 \quad \text{for} \quad -1 < \xi < 1 \tag{3.59a}$$

$$\text{with} \quad B(\xi, 0) = \frac{\xi}{2}\left.\frac{\mathrm{d}h}{\mathrm{d}z}\right|_{z=0},$$

$$Q(z) = \int_0^z \frac{\alpha_1}{\alpha_2 h^2}\frac{\mathrm{d}h}{\mathrm{d}\tilde{z}}d\tilde{z}, \qquad \alpha_2(z) = \exp\left\{\frac{1}{2}p^{(0)}\right\}, \tag{3.59b}$$

and with periodicity $B(\xi + 1, z) = B(\xi - 1, z)$, as for $A(\xi, z)$.

Similarly to $A(\xi, z)$, the advection equation (3.59) may be fully solved for $B(\xi, z)$ using suitable initial conditions at $z = 0$ for $-1 < \xi < 1$, with discontinuities at the beginning and end of each interval forced by the periodic nature of $B(\xi, z)$, similar to $A(\xi, z)$, which again results in an expansion fan.

A subtlety of the solution here, however, unlike the Burger's equation solution for $A(\xi, z)$, is that a discontinuous initial condition coupled with the advection equation for $B(\xi, z)$ does not completely determine the solution within the expansion fan. This distinction arises because, in Burger's equation, the function within an expansion fan is inversely proportional to the slope of characteristic lines, a relationship which does not apply to the advection equation. Consequently, additional information is needed to specify the initial condition for the expansion fan for $B(\xi, z)$. Physically, this might come from solving an inner elastic problem at the contact point at the entrance, a topic not addressed in this study. Consequently, here we assume that, as for Burger's equation, the expansion fan is initially linear, and instead of specifying $B(\xi, z)$ at $z = 0$ and integrating forwards, we specify $B(\xi, z)$ for a small nonzero value of z close to the entrance and solve for the evolution forward to the exit and backward to the entrance using the advection equation (3.59). This allows us to use a continuous initial condition for our solver, chosen such that the solution at the entrance is the desired one.

The numerical solution to (3.59) is non-trivial, with the advected velocity depending on both ξ and z and being positive and negative. Here, an upwinding explicit finite difference method is employed. The computation time varies with the step size in order to maintain a CFL constraint, but the results plotted here are obtained in a few seconds using unoptimised MATLAB code on a standard laptop. It should be noted that there are many ways to numerically solve Burger's equation and the advection equation, and the emphasis here has been on a simple solution that could give illustrative plots of the mathematical solution, rather than an efficient state-of-the-art robust numerical solution.

3.4 Results and comparison with FE simulation

3.4.1 Prediction of through-thickness variation

Figure 3.1 compares the axial stress σ_{xx}, hydrostatic pressure $-p$, and shear stress σ_{xy} predicted by the ABAQUS simulation and the current mathematical model for $\delta = 0.125$ with zero backwards/forwards tensions. The top row shows FE simulation and the two bottom rows show results from the mathematical model with two different inlet boundary conditions. According to the ABAQUS simulation in Figure 3.1, even with zero back tension, the distribution of σ_{xx} is non-zero at the entrance, which can be attributed to the elastic deformation at the entrance. If known, this can be included in the mathematical model by considering the quadratic function as an initial condition as explained in 3.3.1, and the result of this is shown in the middle row in Figure 3.1. In this figure, the unknown term in (3.57) is taken to be $\tau_0(y) - \sigma_{xx}^{(1)}(y, 0) = -2(0.15y^2 + 0.5y - 0.05)$, where the coefficients are chosen by comparing the results with simulation and imposing a zero average $A^{(-)}(\xi, 0)$ in (3.57). However, reasonable results can still be obtained by disregarding the initial distribution of σ_{xx} and imposing a linear distribution for shear stress τ_0 as the initial condition (see the bottom row in Figure 3.1); for this case, $\tau_0 = -1.2y$ is chosen, which gives a good comparison for all rolling parameters considered here and can be utilised if the model is intended to be employed in a fully predictive

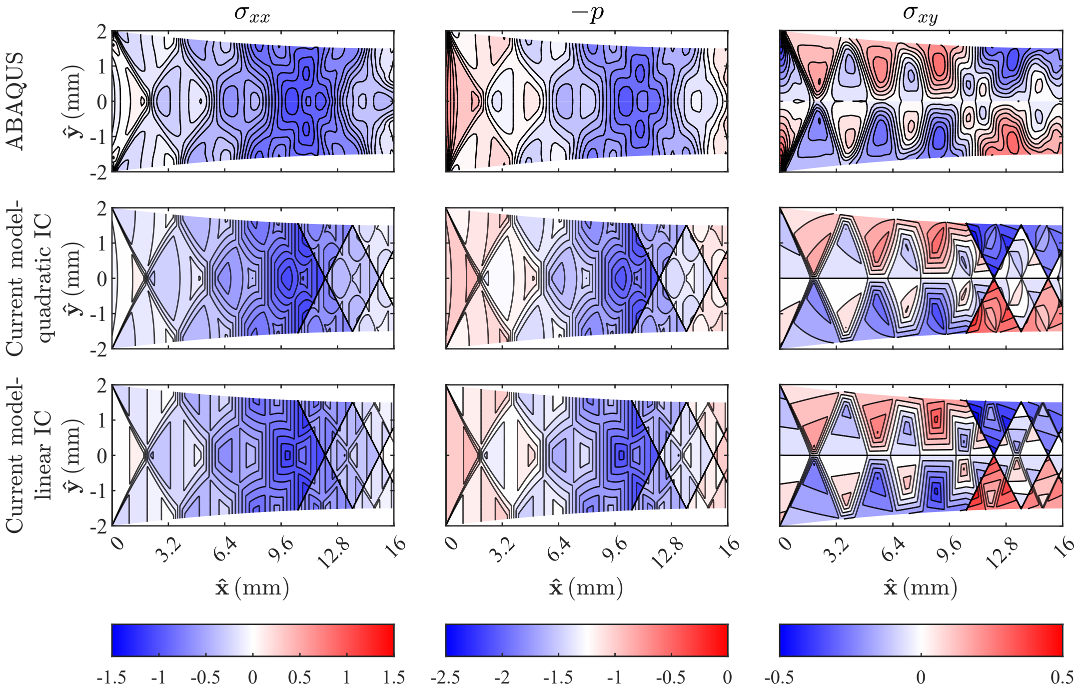

Figure 3.1: Comparison of results for $\delta = 0.125$ from FE simulations (Flanagan et al., 2024) (top row) with the current model (equation 3.54), with two different initial conditions: quadratic initial condition (middle row) and linear initial condition (bottom row). Left: contour plots of horizontal stress. Middle: contour plots of pressure. Right: contour plots of shear stress. Results are shown in dimensionless form, i.e. scaled with $\hat{\kappa}$, the yield stress in shear. Parameters used are $(\hat{h}_0, r, \mu, \hat{\kappa}) = (2\,\text{mm}, 25\%, 0.1, 288.67\,\text{MPa})$.

way without relying on FE data. Comparing the two bottom rows in Figure 3.1 also demonstrates that, with the cost of an extra degree of freedom, the quadratic initial condition results in a rounded pattern which is more similar to the FE simulation. The mathematical model's prediction of stresses at the roll-gap exit differs from those of the FE simulation due to the workpiece unloading and becoming purely elastic, although this appears to be localised to the roll-gap exit and does not appear to affect the agreement of the solution elsewhere within the roll gap.

The oscillatory pattern in the pressure distribution shown in Figure 3.1 is very similar to σ_{xx}, and with a similar effect of the initial conditions at the roll-gap entrance, as is expected from equations (3.54c). The pressure solution is the summation of the leading-order solution describing the "pressure hill" and the $O(\delta)$ correction term causing an oscillatory pattern. As a result of the pressure hill, the pressure is seen to approximately increase in magnitude up to the neutral point ($\hat{x} \approx 10.7$) and decrease after that up to the exit point. Nevertheless, this trend is not monotonic within either of the two zones due to the correction term; each momentary increase in pressure is followed by a subsequent decrease, resulting in the formation of multiple local peaks. This means that unlike the slab method prediction the maximum pressure does not necessarily occur exactly at the neutral point.

The shear stress distribution in the last column in Figure 3.1 also reveals a unique distribution, which is replicated by the mathematical model. The different initial conditions in the last two rows in the σ_{xy} panel in Figure 3.1 do not significantly affect the shear distribution pattern. This implies that a linear variation of shear stress is sufficient to model initial condition in (3.57) for the remainder of this chapter. Unlike many other mathematical models, where the application of Coulomb friction is associated with a vertical discontinuity at the neutral point, the current model correctly predicts the trend of the changing sign in shear along the diagonal lines. This is shown more clearly for shorter roll gaps, plotted as the top rows in Figure 3.2, where the shear stress fields from FE (left column) and the mathematical model (right column) are plotted for varying $\delta = \hat{h}_0/\hat{l}$.

The shear stress predicted by the current model is discontinuous at the surface at the location of the neutral point (see Figures 3.1 and 3.2). While this is an unavoidable consequence of our assumption of Coulomb friction without sticking, the shear stress remains continuous below the surface, as ensured by equation (3.29). The shear stress discontinuity at the surface for the mathematical model causes a shock to form in the Burger's equation solution, producing the sharp diagonal line starting from the neutral point. The FE simulation, on the other hand, predicts a sticking region, giving a smoother transition between positive and negative shear at the neutral point than is observed in the mathematical model. Still, the predicted neutral point is correctly positioned compared with the FE simulations for all aspect ratios.

Another interesting feature seen in Figures 3.1 and 3.2 is the initial diagonal discontinuity in stresses emanating from the first contact point between the workpiece surface and the rolls (e.g. the top left and bottom left points in each plot); this initial discontinuity subsequently spreads out and weakens. This is the result of the evolution of the discontinuity in the initial condition (as explained in 3.3.1) as an expansion fan. Neither of the simple models presented in Chapter 2 was able to capture this effect, and FE simulations require significant numerical resolution at the contact points to accurately reproduce the same behaviour.

The trend observed in Figure 3.2 indicates that the oscillatory pattern is not restricted to a particular aspect ratio, as similar trends are noted for all values of δ between the FE and the model. The number of lobes present increases with roll-gap length and is approximately proportional to the aspect ratio of the roll gap $1/\delta$. This can potentially be explained by the underlying mechanism of deformation. The deformation mechanism in the roll gap is effectively that of uniaxial extension, with the sheet getting longer and thinner, although forced by the rolls rather than extensive normal forces at the entrance and exit. This means the slip lines, along which information about the deformation is carried, align with the local direction of maximum shear at 45 degrees to the centre line. As information only reaches a material element along slip lines, information about initial contact with the rolls, friction, the neutral point, etc, all

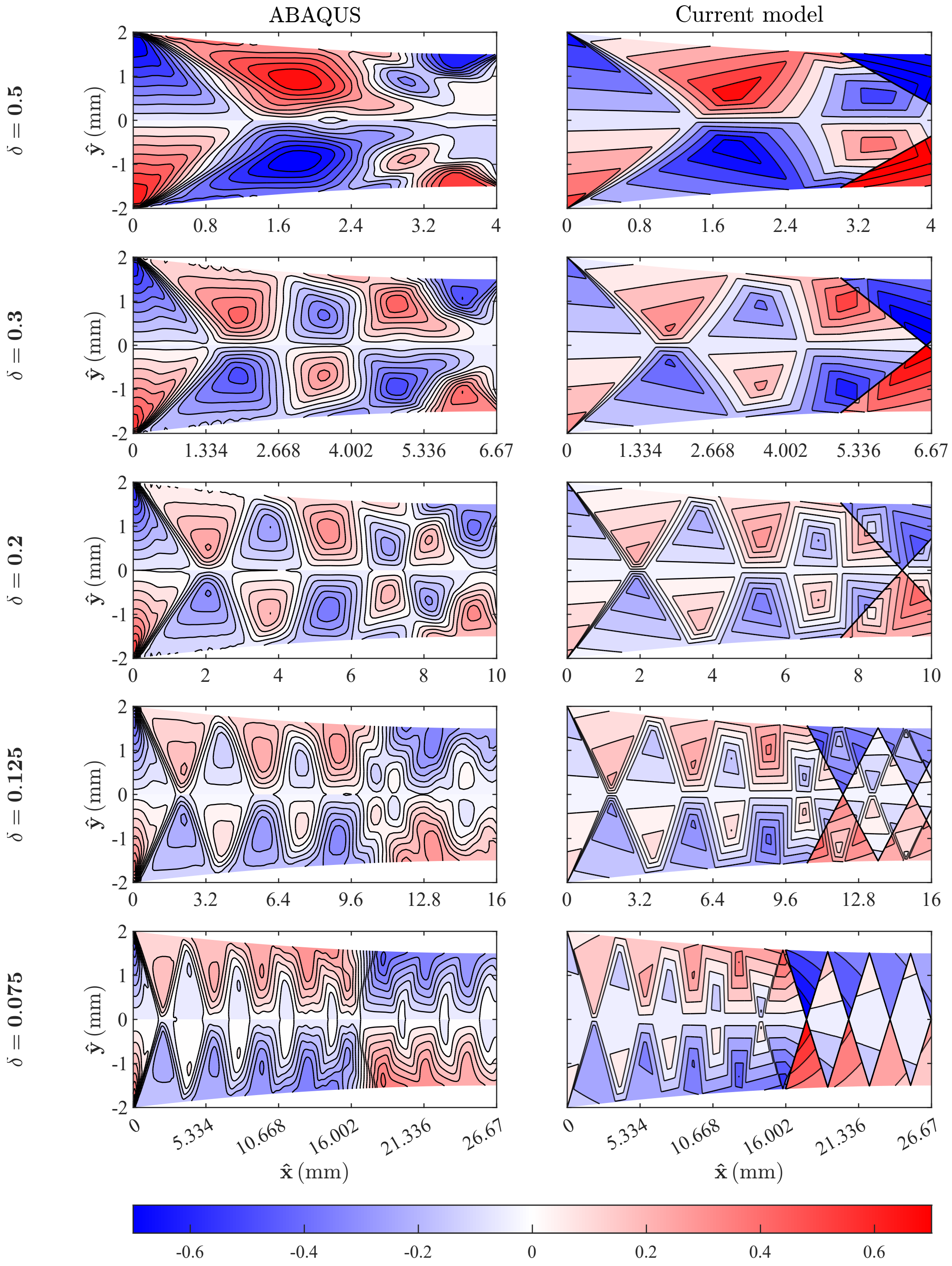

Figure 3.2: Comparison of shear stress results from the current model (equation (3.54b)) (right panel) and FE simulations (Flanagan et al., 2024) (left panel) for varying δ values. Results are shown in dimensionless form, i.e. scaled with $\hat{\kappa}$, the yield stress in shear. Parameters used are $(\hat{h}_0, r, \mu, \hat{\kappa}) = (2\,\text{mm}, 25\%, 0.1, 288.67\,\text{MPa})$, except $\delta = 0.5$ which uses $\mu = 0.25$ and $\delta = 0.3$ which uses $\mu = 0.15$.

travel at 45 degrees to the centre line. This sets up an oscillatory pattern that repeats, because of the 45 degree angle, on average every sheet thickness, meaning the number of oscillations depends on the number of sheet thicknesses that fit into the length of the roll gap. This becomes more comprehensible when viewed alongside the velocity distribution in Figure 3.3.

Figure 3.3 shows the vertical and horizontal velocity distribution for $\delta = 0.125$ both from FE simulation and the mathematical model. The results from the current model with the assumption of a homogeneous rigid-body velocity profile at the entrance align well with FE simulations, despite its elasto-plastic material model. The agreement is attributed to simulating a single pass where the sheet enters horizontally into the roll gap. The frequency at which the pattern in vertical and horizontal velocity recurs is almost the same as that observed in stresses (Figure 3.2). In the vertical velocity contour plots in Figure 3.3, as expected, the material points are pushed towards the centre line due to the presence of the rolls, although interestingly this is limited to certain regions, between which there is almost no vertical velocity. Each zone exhibits distinct horizontal and vertical velocities that are suggestive of a block gliding over its neighbouring block at a roughly constant speed; this provides another alternative interpretation of the contrasting shear signs observed in Figure 3.2.

The horizontal velocity distribution in Figure 3.3 is also notable. The solution to $u^{(0)}$, and indeed the classic slab method, both predict a smoothly increasing horizontal velocity from the entrance to the exit due to the continuity requirement. However, the inclusion of the correction term results in an increasing horizontal velocity characterised by a series of incremental steps. This can be seen in more detail in figure 3.4, where the horizontal velocity along the surface and along the centreline are compared from three different methods: the slab method, the current model, and FE simulations. The sheet is introduced into the roll gap horizontally at a velocity lower than that of the rolls, and initially, while the surface accelerates following contact with the roll, the centre maintains its initial velocity. This trend then reverses and the centre line advances more rapidly than the surface. This leapfrogging of surface and centerline continues up to some point near the exit where the centerline velocity stays higher than the surface, just before the entire block travels uniformly and exits the roll gap in a horizontal direction. The sheet surface velocity and roll velocity are plotted in the bottom row of Figure 3.4 and compared with ABAQUS results. The sheet surface velocity is almost identical to the horizontal velocity plotted in Figure 3.4, as the contribution of the vertical velocity is of order δ. The ABAQUS roll-surface and sheet-surface velocities coincide over a sticking region, while the model sheet-surface velocity increases past the roll-surface velocity at the neutral point, as expected from the differences in sticking and slipping behaviour between the model and the FE.

By way of a more quantitative comparison between the FE and model stresses, figure 3.5 plots the root–mean–square (RMS) differences of the σ_{xx}, σ_{xy} and σ_{yy} stress

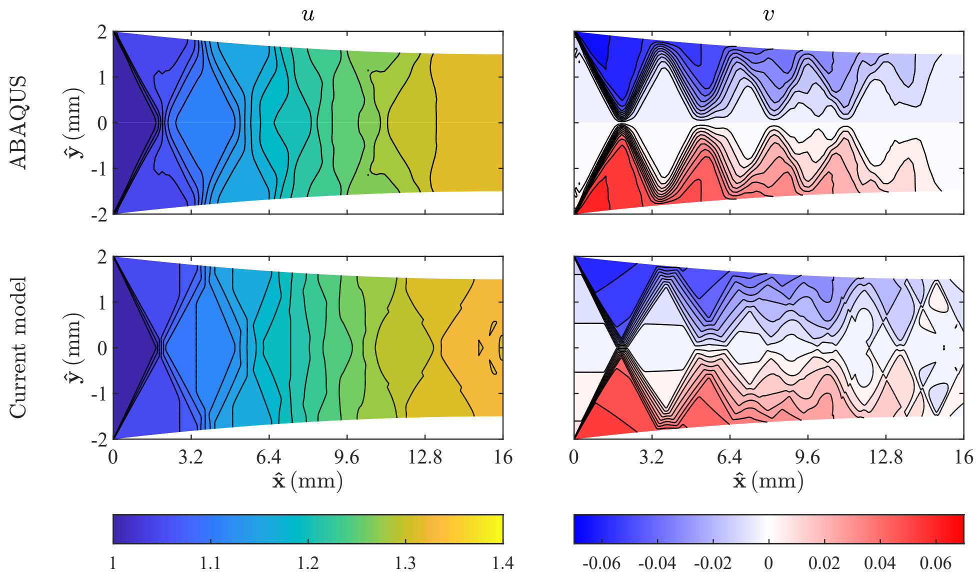

Figure 3.3: Comparison of velocities from the current model (equation (3.58)) (top row) with FE simulations (Flanagan et al., 2024) (bottom row) for $\delta = 0.125$. Left: contour plots of horizontal velocity, right: contour plots of vertical velocity. Results are shown in dimensionless form, i.e. scaled with $\hat{U}_0$, the entrance velocity. The other parameters used are $(\hat{h}_0, r, \mu, \hat{\kappa}) = (2\,\mathrm{mm}, 25\%, 0.1, 288.67\,\mathrm{MPa})$

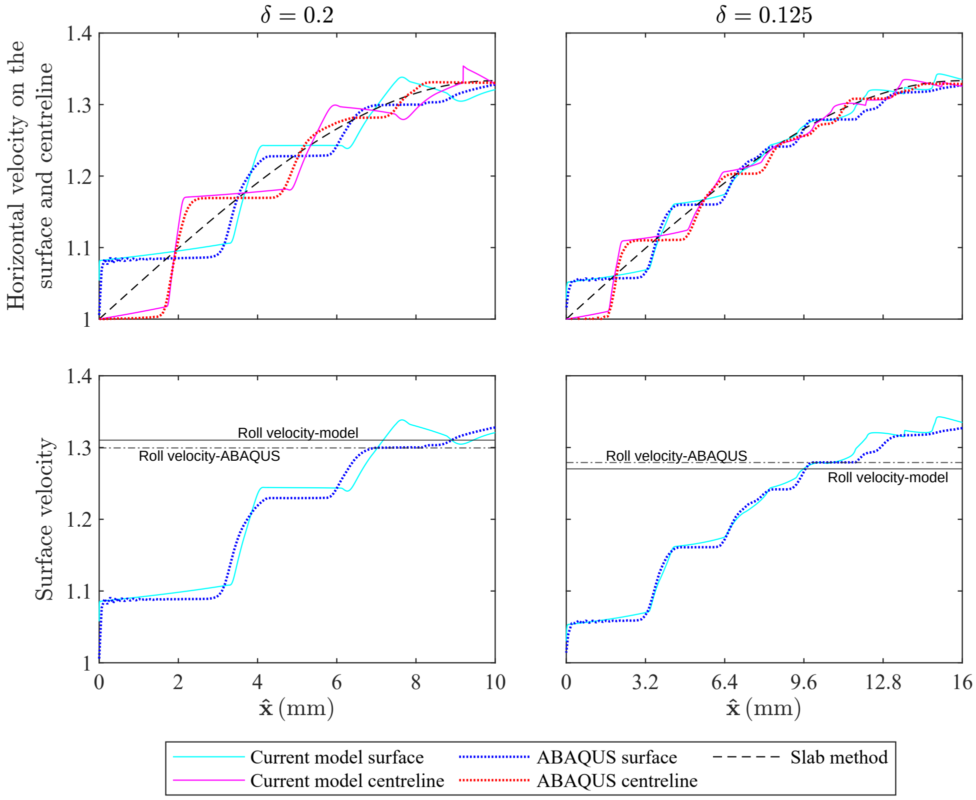

Figure 3.4: Plots of horizontal sheet velocity u on the roll surface and along the centreline (top row), and sheet surface velocity and roll velocity (bottom row) plotted as functions of distance through the roll gap, for $\delta = 0.2$ (left) and $\delta = 0.125$ (right). Results are shown in dimensionless form, i.e. scaled with U_0, the entrance velocity. Other parameters used are $(\hat{h}_0, r, \mu, \hat{\kappa}) = (2\,\mathrm{mm}, 25\%, 0.1, 288.67\,\mathrm{MPa})$. Also plotted are the horizontal roll-surface velocities for comparison.

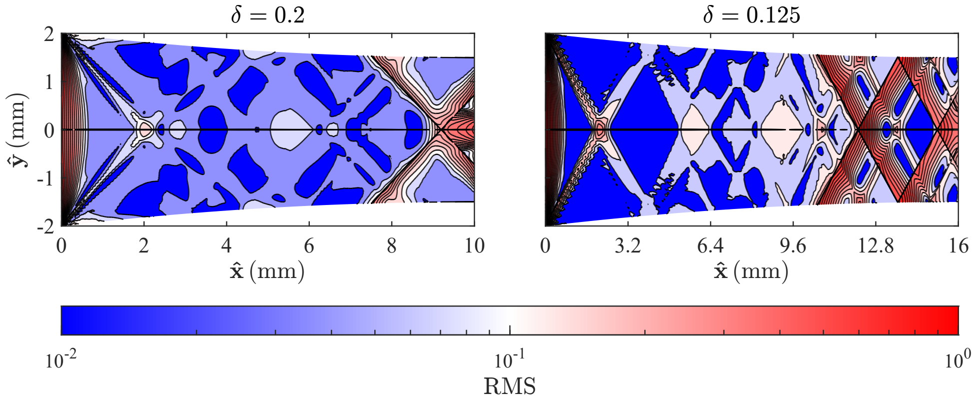

Figure 3.5: RMS differences between the FE and model stresses (combining σ_{xx}, σ_{yy} and σ_{xy}) for $\delta = 0.2$ (left) and $\delta = 0.125$ (right).

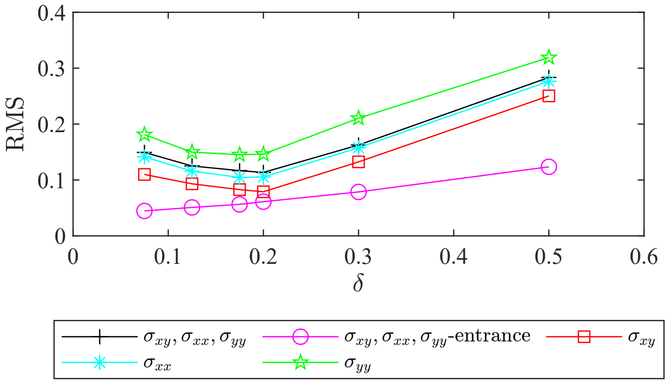

Figure 3.6: Averaged RMS differences between the FE and model stresses for different values of δ and different stress components (σ_{xx}, σ_{yy}, σ_{xy}, and all combined). The "entrance" values are calculated only from the entrance to the neutral point.

components between the FE results and the model results. Before the neutral point, the difference is mostly $O(\delta^2)$, as expected from the asymptotic analysis; however, after the neutral point, the difference increases to $O(\delta)$ due to the assumption of no sticking region in the model. Significant differences are also seen at the entrance owing to the initial deformation in the FE results being below-yield and elastic, while the model neglects elasticity. The average RMS difference is dominated by the larger post-neutral-point differences, as is demonstrated in figure 3.6. The average RMS differences for each component of the stress follow the same trend as the combined differences, and are significantly larger than the average differences in the entrance region only (averaged from the entrance up to the neutral point). The asymptotics is expected to give more accuracy for smaller values of δ, and this is seen in the entrance region. However, the differences between the FE and the model increase beyond the neutral point as δ is reduced, owing to the increased number of oscillations in this region for smaller δ.

3.4.2 Comparison to slab analysis

Since slab analysis is not intended to give through-thickness information, it would be unfair to compare the results above with the slab method. Instead, the distribution on the surface is used to compare the slab method, the FE, and the current model. Results for pressure, as well as shear, normal, and tangential stresses, are plotted for two aspect ratios in Figure 3.7. Note that the normal stress characterises the roll pressure, and the hydrostatic pressure plotted here on the surface is different from the roll pressure. The pressure labelled as the "slab method" is obtained from the leading-order pressure equation (3.21), while the "current model" pressure curve is derived from equation (3.54a). The compressive normal stress, σ_n, is approximated by σ_{yy} in the "slab method", and computed from the leading-order relation $\sigma_{yy}^{(0)} = -1 - p^{(0)}$. Note that while the hydrostatic pressure and roll pressure are compressive and therefore negative in sign, the absolute values are plotted in Figure 3.7. The tangential stress, σ_t, in the "slab method" is calculated as $\mp\mu\sigma_{yy}^{(0)}$, whereas for the "current model", σ_n and σ_t are obtained from the components of the stress tensor using $\boldsymbol{n}\cdot\boldsymbol{\sigma}\cdot\boldsymbol{n}$ and $\boldsymbol{t}\cdot\boldsymbol{\sigma}\cdot\boldsymbol{n}$, respectively. For shear stress, the "slab method" curve is given by $y\,\mathrm{d}p^{(0)}/\mathrm{d}z$, with an $O(\delta^2)$ correction added using the boundary condition $\sigma_{xy}^{(2)} \mp \beta p^{(1)} = 0$ at $y = h$, to obtain the "current model" shear stress.

The hydrostatic pressure p and the roll pressure σ_n exhibit the same oscillatory pattern, with their magnitudes differing by approximately a constant offset. The mathematical model accurately captures the oscillations observed in the FE data by incorporating a correction term of magnitude δ. For short roll-gap lengths, this correction is not necessarily small, and in fact, the successive pressure peaks completely overcome the classic slab method pressure hill profile, as was observed experimentally by Al-Salehi et al. (1973). These deviations are unrelated to elastic deformation, roll flattening, or hardening, as those effects are not included here. As the sheet length increases, the stress oscillations become small fluctuations to the pressure hill, as also noted by Montmitonnet (2006). These oscillations are averaged out when integrating the roll pressure and shear over the whole roll surface to produce the roll force and roll torque; this is why both roll force and roll torque are poor measures for the accuracy of a rolling simulation (Flanagan et al., 2024), and why classical slab methods produce reasonable predictions for the total roll force and roll torque.

When considering shear on the surface, the current model prediction is identical to the slab method to the first-order correction on the surface (see equations (3.54b) and (3.56)). However, incorporating the correction of $O(\delta^2)$ on the surface accounts for the oscillations detected in the simulation, and this is what is plotted as "Current model" surface shear in Figure 3.7. The number of local peaks increases for longer sheet lengths, as also seen in the shear lobe pattern in Figure 3.2. As mentioned in the previous section, the observed discontinuity on the surface at the neutral point is an inevitable consequence of slipping Coulomb friction, while the FE simulation varies

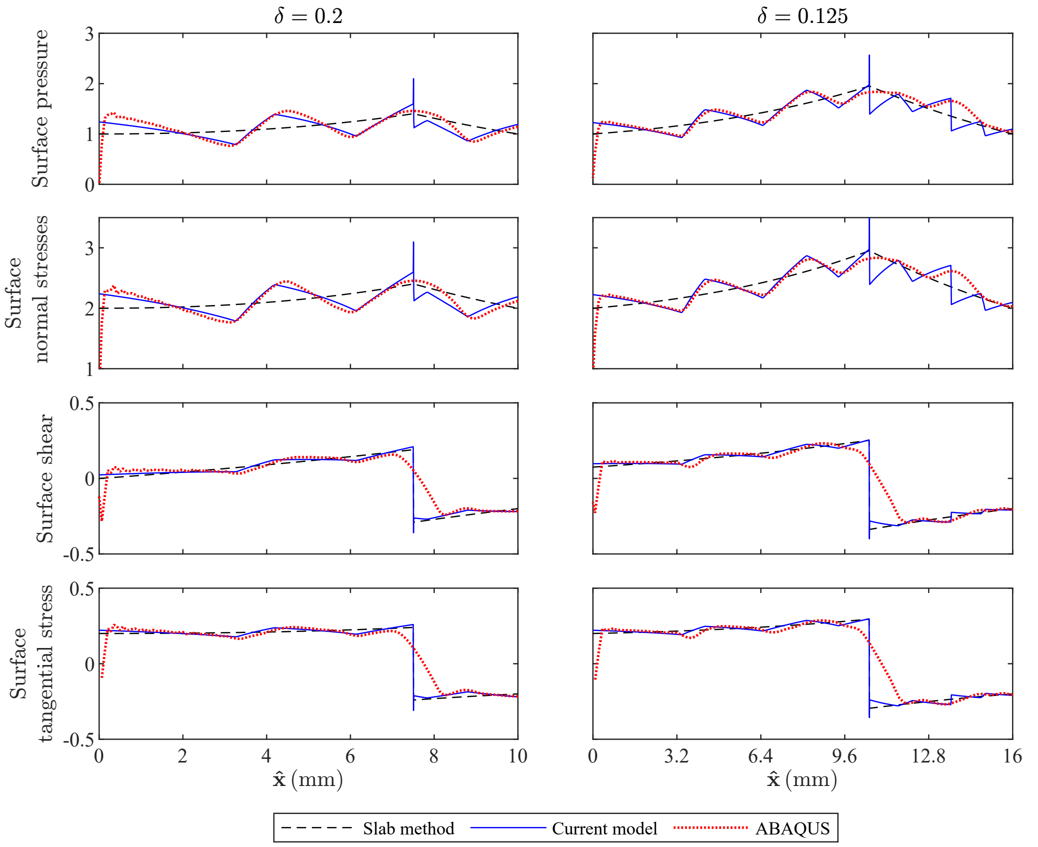

Figure 3.7: Plots of p (first row), σ_n (second row), σ_{xy} (third row) and σ_t (bottom row) on the sheet surface, plotted as a function of distance through the roll gap, for $\delta = 0.2$ (left) and $\delta = 0.125$ (right). Results are shown in dimensionless form, i.e. scaled with $\hat{\kappa}$, the yield stress in shear. Other parameters used are $(\hat{h}_0, r, \mu, \hat{\kappa}) = (2\,\text{mm}, 25\%, 0.1, 288.67\,\text{MPa})$.

smoothly due to a small zone of sticking friction. This could be improved in future by incorporating sticking friction in the asymptotic model, although a more rigorous study would be required also incorporating elasticity, as the friction rule alone may not solely be responsible for the behaviour around the neutral point (Orowan, 1943; Flanagan et al., 2024). Such alternative friction treatments are beyond the scope of the present study. Also, the sudden changes observed near the entrance in the FE surface pressure and shear results are attributable to elastic deformation, which is not accounted for in the current model. Finally, the tangential stress profile is quite similar to the shear stress profile and shares the same characteristics, though the magnitude is different.

3.4.3 Streamlines

Streamlines represent the paths followed by material particles as they flow through the deformation zone. Streamlines in the metal rolling process are useful for visualising material flow during deformation. Demonstrative streamlines for different distances through the thickness are plotted in Figure 3.8 using the `stream2` function in MATLAB.

As the material is assumed to enter horizontally as a rigid body, the streamlines are horizontal outside the roll gap at the entrance, and then curve inward as the material approaches the roll gap, following the curvature of the roll. However, the streamlines through the thickness show slight fluctuations due to the velocity oscillations discussed earlier. Figure 3.8 also shows the horizontal velocity, vertical stress, and shear stress along the presented streamlines in the top-left corner plot, using the same colour scheme to indicate the related streamline. While the through-thickness velocity and vertical stress remain between their surface and midplane values, the maximum shear stress does not occur at the surface but within the material's thickness.

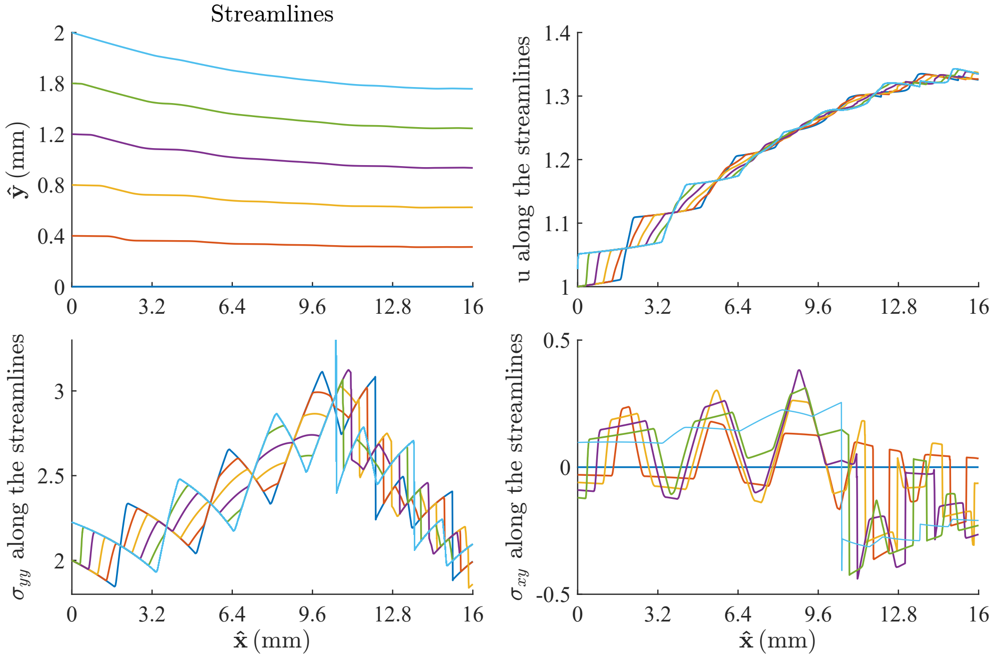

Figure 3.8: Plots of streamlines and u and σ_{yy} and σ_{xy} along the streamlines, plotted as a function of distance through the roll gap, for $\delta = 0.125$. Results are shown in dimensionless form. Other parameters used are $(\hat{h}_0, r, \mu, \hat{\kappa}) = (2\,\text{mm}, 25\%, 0.1, 288.67\,\text{MPa})$.

3.4.4 Comparison with a work-hardening FE simulation

In the previous sections, the current mathematical model was extensively verified against FE simulations which used a non-hardening material model, where the yield stress was kept fixed at $\hat{\kappa} = 288.67\,\text{MPa}$. To examine the deviation of the model when the realistic material is concerned, we now compare the current mathematical model with non-hardening material against the simulation results with hardening material. For this, in the FE simulation, the initial yield stress is taken to be $\hat{\kappa} = 275.51\,\text{MPa}$ increasing to $324.29\,\text{MPa}$ at a true plastic strain of 0.4 as a result of strain hardening.

Figure 3.9 shows pressure and shear distribution on the sheet surface from the current model and from the FE simulation with hardening material. Since in the mathematical model all stresses are scaled by the yield stress $\hat{\kappa}$, the prediction depends on its magnitude. To see the effect, the simulation is compared with the mathematical model twice: once taking the stress scaling factor as the initial yield stress $\hat{\kappa} = 275.51\,\mathrm{MPa}$; and once as the average yield stress $\hat{\kappa} = 288.67\,\mathrm{MPa}$ from the hardening simulation. The impact of the different stress scalings is more noticeable on the pressure rather than shear stress, and overall, the larger scaling ($\hat{\kappa} = 288.67\,\mathrm{MPa}$) results in better agreement. The stress oscillations seem to be unaffected by the hardening characteristics, with the effect of hardening being only a progressive increase in the magnitude of stress from left to right as the workpiece passes through the roll gap. This is explored further in the next chapter, where incorporating hardening into the mathematical model leads to additional improvements.

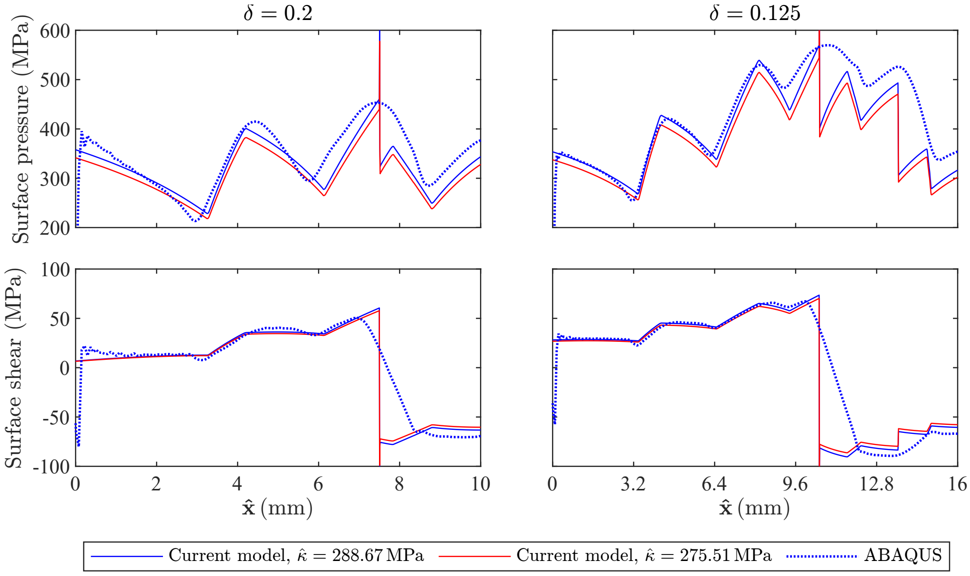

Figure 3.9: Plots of p (top) and σ_{xy} (bottom) on the roll surface, plotted as a function of distance through the roll gap. ABAQUS results (Flanagan et al., 2024) are from hardening material, with an initial yield stress of $\hat{\kappa} = 275.51\,\mathrm{MPa}$ increasing to $324.29\,\mathrm{MPa}$ at a true plastic strain of 0.4 as a result of strain hardening. The current model is for non-hardening material with two different yield stresses $\hat{\kappa} = 288.67\,\mathrm{MPa}$ and $\hat{\kappa} = 275.51\,\mathrm{MPa}$. The left panel shows results for $\delta = 0.2$. The right panel shows results for $\delta = 0.125$. Other parameters used are $(\hat{h}_0, r, \mu) = (2\,\mathrm{mm}, 25\%, 0.1)$

3.5 Conclusion

A semi-analytic model for symmetric rolling under Coulomb friction has been presented. Two length scales were introduced which enable the use of a multiple-scales asymptotic analysis: the large scale of the length of the roll gap, $\hat{l}$; and the small length scale of the initial sheet half-thickness, $\hat{h}_0$. The leading-order solution depends on the large length scale only and recreates the conventional pressure hill from slab analysis. The next-order correction is an order $O(\delta)$ smaller than the leading order, depends on both the large and small length scales, and reveals two sets of waves for stress and velocity distribution varying on the short length scale of the sheet thickness. These are governed by a Burger's equation and an advection equation respectively, and can easily be solved numerically with suitable initial conditions at the roll-gap entrance.

Significant work is needed for the FE simulation to be sufficiently accurate to give good agreement with the mathematical model. This highlights another use of the mathematical model presented here: it can be used to validate FE simulations. To date, the asymptotic solution and FE simulations shown here demonstrate the highest degree of agreement the author is aware of in the literature. The solutions deviate in three places due to the simplifying assumptions of the mathematical model: the entrance and exit regions are sub-yield and are therefore governed by elasticity, which is neglected in the mathematical model; and the neutral point demonstrates sticking behaviour in the numerical simulations while only slipping friction was assumed in the mathematical model.

The mathematical model presented in this study offers a significant advantage in terms of computational efficiency compared to FE simulations. The FE simulations for $\delta = 0.125$ used in this chapter took 15.89 hours CPU time to run on a standard desktop computer, making them unsuitable for optimisation and real-time control. In contrast, the unoptimised MATLAB code evaluating the new mathematical model for the same δ took 3.45 seconds CPU time to run on a standard laptop which is more than 16,000 times faster compared to FE simulation.

The corrections to the stress distribution have a minimal influence on the overall roll force and torque predictions, indicating that the accuracy of roll forces and torques are poor indications of the quality and accuracy of the entire simulation. Moreover, these fine details in the stress and velocity distribution will likely become significant when studying material properties, such as the hardening, development of anisotropy, or development of residual stress in the rolled sheet.

Further work could look at the entry and exit boundary conditions, likely by the inclusion of an elastic entrance and exit region. Similarly, including elasticity and a sticking friction model near the neutral point would smooth the shock that is seen in the mathematical model but not the FE simulations. Calculating higher-order terms, for example of $O(\delta^2)$, may or may not lead to more accurate results, and is unlikely to uncover new behaviour. Finally, the present model's assumptions of perfect plasticity could be generalised to more realistic material models including strain-hardening which is the subject of the next chapter.

Chapter 4

Asymptotic model of sheet rolling with hardening material

Driven by the motivation to study the effect of rolling on material properties and to have a more realistic model, the asymptotic model from Chapter 3 has been extended to incorporate isotropic hardening.

The governing equations are outlined in Section 4.2. The solutions are detailed in Section 4.3, where it is explained why incorporating the effect of hardening at the first-order correction is not feasible. In light of ABAQUS results, in Section 4.4 the assumption is established that the effect of hardening at the first-order correction on stress and strain is negligible. With this approximation, the solutions are derived and compared with FE results in Section 4.5.

This model is consistent with the non-hardening model in the limit of constant yield stress.

4.1 Introduction

In cold rolling, hardening occurs primarily due to the plastic deformation of the metal as it is compressed and elongated between rollers. Studying the effect of hardening in metal rolling is important because it affects the mechanical properties and performance of the final product, including strength, durability, and resistance to further deformation.

Hardening was incorporated into the slab model by Alexander (1972) by modifying the yield stress using a power law $Y = Y_0(1 + C\varepsilon_{eq})^m$, where Y_0 is the initial yield stress, and C and m are material constants and ε_{eq} denotes the equivalent strain. The effective strain term was then approximated with $(2/\sqrt{3})\ln(h_0/h)$ by assuming vertically homogenous deformation. Smet and Johnson (1989) employed the same hardening rule in their asymptotic analysis of cold rolling. The equivalent strain was expressed as the time integral of the equivalent strain rate, with the integration variable subsequently transformed using the pathline of a material particle, $S = S(t)$, which was further simplified to x. By incorporating the assumption of a significant shear effect, inhomogeneous deformation was accounted for in their model. The solution, however, required solving three coupled equations numerically with an initial guess for the solution of one of the equations, which was not very straightforward. They claimed that the introduction of inhomogeneous work hardening would invalidate the need for the boundary condition of sticking on the rolls because the shear stress can never exactly equal the yield stress (except possibly at only one point). Domanti and McElwain (1995) used the same hardening rule with an extra small parameter, which simplified the equations, allowing them to solve the first-order hardening directly from the leading-order stress or velocity, independently of the first-order solution. Cherukuri et al. (1997) incorporated the strain-rate hardening into their asymptotic analysis by combining the flow rule and hardening law as $\dot{\varepsilon}_{ij} = \hat{B}\hat{\Omega}^{n-1}\hat{s}_{ij}$. In this formulation, $\hat{B}$ is material constant, n is a hardening-rate exponent, $\hat{\Omega}$ is von Mises stress, defined as $\sqrt{1/2\left(\hat{s}_{xx}^2 + \hat{s}_{yy}^2\right) + \hat{s}_{xy}^2}$, and $\hat{B}\hat{\Omega}^{n-1}$ appears to be equivalent to $\hat{\lambda}$ in the conventional flow rule.

4.2 Mathematical model

4.2.1 Governing equations

While similar to previous chapters, elastic effects are neglected in both the workpiece and the rollers, the metal between the rolls is allowed to harden as a result of plastic strain. This modifies the von Mises yield function, previously used, into

$$\frac{1}{4}\left(\hat{\sigma}_{xx} - \hat{\sigma}_{yy}\right)^2 + \hat{\sigma}_{xy}^2 = \hat{\sigma}_p^2, \tag{4.1}$$

where $\hat{\sigma}_p$ represents the shear yield stress, which evolves due to hardening. For brevity, we refer to this as “hardening” throughout this chapter. The hardening behaviour is modelled using the same equation employed by Alexander (1972):

$$\hat{\sigma}_p = \hat{\kappa}(1 + C\varepsilon_{eq})^m, \tag{4.2}$$

where C and m are material constants, and $\hat{\kappa}$ is the initial shear yield stress at the start of the process. It should be noted that any other hardening equation can be employed, provided it offers a continuous prediction of yield strength from $\varepsilon_{eq} = 0$ to higher values of ε_{eq}.

The remaining governing equations are identical to those presented in Chapter 3 and are therefore not repeated here.

4.2.2 Non-dimensionalised governing equations

Hardening is non-dimensionalised with the same factor as other stresses, $\hat{\kappa}$. Therefore, equation (4.2) is non-dimensionalised as

$$\sigma_p = (1 + C\varepsilon_{eq})^m . \tag{4.3}$$

Since the strain rate can be defined in terms of velocity (see equation (1.14)), we proceed by taking the time derivative of equation (4.3), resulting in

$$\dot{\sigma_p} = mC\dot{\varepsilon}_{eq}\,{\sigma_p}^{\frac{m-1}{m}} , \tag{4.4}$$

where $\dot{\varepsilon}_{eq}$, by definition, is equal to $\sqrt{(2/3)\dot{\varepsilon}_{ij}\dot{\varepsilon}_{ij}}$, which simplifies to the following equation for incompressible plane-strain deformation:

$$\dot{\varepsilon}_{eq} = \frac{2}{\sqrt{3}}\sqrt{\dot{\varepsilon}_{xx}^2 + \dot{\varepsilon}_{xy}^2}. \tag{4.5}$$

Replacing equation (4.5) into the right-hand side of equation (4.4) and applying the material derivative on the left-hand side, we obtain

$$u\frac{\partial \sigma_p}{\partial x} + v\frac{\partial \sigma_p}{\partial y} = mC\frac{2}{\sqrt{3}}\sqrt{\dot{\varepsilon}_{xx}^2 + \dot{\varepsilon}_{xy}^2}\;{\sigma_p}^{\frac{m-1}{m}} , \tag{4.6}$$

or equally, from the flow rule equation,

$$u\left(\frac{1}{h}\frac{\partial \sigma_p}{\partial n} + \delta\frac{\partial \sigma_p}{\partial z}\right) + v\frac{\partial \sigma_p}{\partial y} = mC\frac{2}{\sqrt{3}}\sqrt{(\lambda s_{xx})^2 + (\lambda s_{xy})^2}\;{\sigma_p}^{\frac{m-1}{m}} . \tag{4.7}$$

Note that $\partial/\partial x$ in equation (4.6) is replaced with (3.2) to include multiple scales defined in Chapter 3. Equation 4.7 is an evolutionary equation for hardening in terms of stresses.

The rest of the equations are identical to those presented in Section 3.1.2 of Chapter 3. However, for ease of referencing, the equations are rewritten here;

$$\frac{1}{h(z)}\frac{\partial \sigma_{xx}}{\partial n} + \delta\frac{\partial \sigma_{xx}}{\partial z} + \frac{\partial \sigma_{xy}}{\partial y} = 0, \tag{4.8}$$

$$\frac{\partial \sigma_{yy}}{\partial y} + \frac{1}{h(z)}\frac{\partial \sigma_{xy}}{\partial n} + \delta\frac{\partial \sigma_{xy}}{\partial z} = 0, \tag{4.9}$$

$$\frac{1}{4}(\sigma_{xx} - \sigma_{yy})^2 + \sigma_{xy}^2 = \sigma_p^2, \tag{4.10}$$

$$\frac{1}{h(z)}\frac{\partial u}{\partial n} + \delta\frac{\partial u}{\partial z} + \frac{\partial v}{\partial y} = 0, \tag{4.11}$$

$$\frac{1}{h(z)}\frac{\partial u}{\partial n} + \delta\frac{\partial u}{\partial z} = \frac{1}{2}\lambda(\sigma_{xx} - \sigma_{yy}) = \lambda s_{xx}, \tag{4.12}$$

$$\frac{\partial u}{\partial y}+\frac{1}{h(z)}\frac{\partial v}{\partial n}+\delta\frac{\partial v}{\partial z}=2\lambda\sigma_{xy}, \tag{4.13}$$

with, again, the boundary condition of Coulomb friction applied on the roll surface

$$\delta\frac{\mathrm{d}h}{\mathrm{d}z}(\sigma_{yy}-\sigma_{xx})+\left(1-\delta^2\left(\frac{\mathrm{d}h}{\mathrm{d}z}\right)^2\right)\sigma_{xy}=\mp\delta\beta\left(\sigma_{yy}-2\delta\frac{\mathrm{d}h}{\mathrm{d}z}\sigma_{xy}+\delta^2\left(\frac{\mathrm{d}h}{\mathrm{d}z}\right)^2\sigma_{xx}\right), \tag{4.14}$$

and tensions per unit width $F_{\text{in/out}}$ applied at the entrance and exit

$$F_{\text{in/out}}=\int_{-h_{\text{in/out}}}^{h_{\text{in/out}}}\sigma_{xx}\,\mathrm{d}y. \tag{4.15}$$

4.3 Solution

4.3.1 Leading-order solution

With the unchanged force and mass balance equations and boundary conditions as the non-hardening model, we recover that $\sigma_{xy}^{(0)}=\lambda^{(0)}=v^{(0)}=0$, and $u^{(0)}=1/h(z)$. The yield function (4.10), at leading order, is

$$\frac{1}{2}\left(\sigma_{xx}^{(0)}-\sigma_{yy}^{(0)}\right)=\sigma_p^{(0)}. \tag{4.16}$$

Combining the definition of hydrostatic pressure with the yield equation (4.16), we get

$$\sigma_{xx}^{(0)}=\sigma_p^{(0)}-p^{(0)} \qquad \text{and} \qquad \sigma_{yy}^{(0)}=-\sigma_p^{(0)}-p^{(0)}, \tag{4.17}$$

considering the fact that $\sigma_{yy}^{(0)}$ is more compressive than $\sigma_{xx}^{(0)}$. From the force balance equation (4.9) at leading order

$$\frac{\partial\left(\sigma_p^{(0)}+p^{(0)}\right)}{\partial y}=0. \tag{4.18}$$

$p^{(0)}$ and $\sigma_p^{(0)}$ must be symmetric about the centre line and both greater than zero, and the back tension (as defined in equation (4.15)) must be greater than or equal to zero. Yet equation (4.18) allows for variation in y for $p^{(0)}$ and $\sigma_p^{(0)}$. For simplicity and consistency, we assume $p^{(0)}$ and $\sigma_p^{(0)}$ are independent of y, which is generally a valid assumption for leading-order solutions. The solution for $p^{(0)}(z)$ is determined by satisfying the friction equation (4.14) at $O(\delta)$, while the solution for $\sigma_p^{(0)}(z)$ is governed by the hardening rate equation (4.7). However, both equations depend on as-yet unknowns that will be revealed in the next order. Therefore, the first-order equations must be solved in the subsequent section before $\sigma_p^{(0)}(z)$ and $p^{(0)}(z)$ can be fully determined.

The prescribed front and back tension (equation (4.15)) dictate the pressure at the entrance and exit as

$$p^{(0)}(z=0)=\sigma_p^{(0)}(0)-\frac{F_{\text{in}}}{2} \qquad \text{and} \qquad p^{(0)}(z=1)=\sigma_p^{(0)}(1)-\frac{F_{\text{out}}}{2h(1)}, \tag{4.19}$$

where $\sigma_p^{(0)}(0)$ is equal to 1 due to scaling, and $\sigma_p^{(0)}(1)$ will be determined independently of the pressure in the next section.

4.3.2 First-order solution

By only taking terms of order δ in the continuity equation (4.11) and the shear flow-rule equation (4.13), the same solution as non-hardening for $u^{(1)}$ and $v^{(1)}$ is derived;

$$u^{(1)}=B\Big(n+\frac{y}{h},z\Big)+B\Big(n-\frac{y}{h},z\Big), \tag{4.20a}$$

$$v^{(1)}=-\Big[B\Big(n+\frac{y}{h},z\Big)-B\Big(n-\frac{y}{h},z\Big)\Big]+\frac{y}{h^2}\frac{\mathrm{d}h}{\mathrm{d}z}, \tag{4.20b}$$

where $B(\xi,z)$ is an as-yet-unknown function with the same constraint as non-hardening model;

$$B(n+1,z)-B(n-1,z)=0, \qquad \text{and} \qquad \int_{-1}^{1}B(\xi,z)\,\mathrm{d}\xi=0. \tag{4.21}$$

Also, similar to the non-hardening model, we set $v^{(1)}\equiv u^{(1)}\equiv 0$ at the entrance, consistent with our assumption of rigid body motion at the entrance. Therefore, the initial condition for $B(\xi,z)$ at $n=z=0$ is given from (4.20) as

$$B(y,\,0)=\frac{y}{2}\left.\frac{\mathrm{d}h}{\mathrm{d}z}\right|_{z=0}. \tag{4.22}$$

From the hardening equation (4.7), $\sigma_p^{(0)}$ and $\sigma_p^{(1)}$ are related through a single equation as

$$u^{(0)}\frac{\mathrm{d}\sigma_p^{(0)}}{\mathrm{d}z}+\frac{1}{h}u^{(0)}\frac{\partial\sigma_p^{(1)}}{\partial n}=mC\frac{2}{\sqrt{3}}\lambda^{(1)}s_{xx}^{(0)}\,\sigma_p^{(0)}{}^{\frac{m-1}{m}}. \tag{4.23}$$

By substituting the flow rule equation (4.12) with the term $\lambda^{(1)}s_{xx}^{(0)}$ and subsequently rearranging the resulting expression, we arrive at

$$u^{(0)}\frac{\mathrm{d}\sigma_p^{(0)}}{\mathrm{d}z}-\frac{2}{\sqrt{3}}mC\frac{\mathrm{d}u^{(0)}}{\mathrm{d}z}\,\sigma_p^{(0)}{}^{\frac{m-1}{m}}=-\frac{1}{h}\left(u^{(0)}\frac{\partial\sigma_p^{(1)}}{\partial n}-\frac{2}{\sqrt{3}}mC\frac{\partial u^{(1)}}{\partial n}\,\sigma_p^{(0)}{}^{\frac{m-1}{m}}\right). \tag{4.24}$$

The left-hand side in (4.24) only depends on z. Therefore, we may write

$$\frac{\mathrm{d}\sigma_p^{(0)}}{\mathrm{d}z} - T(z)\frac{\mathrm{d}u^{(0)}}{\mathrm{d}z} = f(z), \tag{4.25a}$$

$$\frac{\partial\sigma_p^{(1)}}{\partial n} - T(z)\frac{\partial u^{(1)}}{\partial n} = -h(z)f(z), \tag{4.25b}$$

where $T(z) = (2/\sqrt{3})mCh\,\sigma_p^{(0)\,\frac{m-1}{m}}$. In (4.25b), the right-hand side is a function of the slow variable z only, and $u^{(1)}$ in the left-hand side is a function of the fast-changing variable, n, but bounded in it (see equations (4.21)). If $f(z)$ is nonzero, then $\partial\sigma_p^{(1)}/\partial n$ grows by $-2h(z)f(z)$ every time n increases by 2, and by the end of the roll gap, $\sigma_p^{(1)}$ would have grown to be $O(n) = O(1/\delta)$ and the asymptotic ordering we assumed in deriving our equations would be broken. We, therefore, require $f = 0$. With this, the equation (4.25a) can be solved for $\sigma_p^{(0)}$ in terms of $u^{(0)}$, and equation (4.25b) for $\sigma_p^{(1)}$ in terms of $u^{(1)}$, to give

$$\sigma_p^{(0)} = \left(1 - \frac{2}{\sqrt{3}}C\log h\right)^m, \tag{4.26a}$$

$$\sigma_p^{(1)} = T(z)u^{(1)}, \tag{4.26b}$$

where in (4.26a) we have considered $\sigma_p^{(0)}(z=0) = 1$, and in (4.26b) the symmetry of σ_p with respect to the $y = 0$ axis. It should be noted that equation (4.26a) represents the same solution for hardening derived by Alexander (1972), which is anticipated, given that the assumptions in our leading-order analysis are consistent with those used in the slab method.

By taking terms only order δ in the yield function (4.10), and from the definition of hydrostatic, $\sigma_{xx}^{(1)}$ and $\sigma_{yy}^{(1)}$ are solved to be

$$\sigma_{xx}^{(1)} = \sigma_p^{(1)} - p^{(1)} \qquad \text{and} \qquad \sigma_{yy}^{(1)} = -\sigma_p^{(1)} - p^{(1)}. \tag{4.27}$$

Accordingly, the local balance equations (4.8) and (4.9) at this order are simplified to the following equations, respectively:

$$\frac{\partial\sigma_{xy}^{(1)}}{\partial y} + \frac{1}{h}\frac{\partial\left(\sigma_p^{(1)} - p^{(1)}\right)}{\partial n} = -\frac{\mathrm{d}\left(\sigma_p^{(0)} - p^{(0)}\right)}{\mathrm{d}z}, \tag{4.28}$$

$$-\frac{1}{h}\frac{\partial\sigma_{xy}^{(1)}}{\partial n} + \frac{\partial\left(\sigma_p^{(1)} + p^{(1)}\right)}{\partial y} = 0. \tag{4.29}$$

Substituting $\sigma_p^{(1)}$ from (4.26b), the solutions for $p^{(1)}$ and $\sigma_{xy}^{(1)}$ are found to be

$$p^{(1)} = A\left(n+\frac{y}{h}, z\right) + A\left(n-\frac{y}{h}, z\right) - yT\left[B'\left(n+\frac{y}{h}, z\right) - B'\left(n-\frac{y}{h}, z\right)\right], \tag{4.30a}$$

$$\sigma_{xy}^{(1)} = A\left(n+\frac{y}{h}, z\right) - A\left(n-\frac{y}{h}, z\right) - yT\left[B'\left(n+\frac{y}{h}, z\right) + B'\left(n-\frac{y}{h}, z\right)\right] \tag{4.30b}$$
$$+ y\frac{\mathrm{d}\left(p^{(0)} - \sigma_p^{(0)}\right)}{\mathrm{d}z},$$

considering the fact that p is symmetric and σ_{xy} is asymmetric with respect to the $y = 0$ axis.

The Coulomb friction boundary condition on the surface provides information about $\sigma_{xy}^{(1)}$ in terms of the leading-order solution. At $O(\delta)$, the Coulomb friction equation (4.14) is

$$-2\frac{\mathrm{d}h}{\mathrm{d}z}\sigma_p^{(0)} + \sigma_{xy}^{(1)} \mp \beta\left(\sigma_p^{(0)} + p^{(0)}\right) = 0. \tag{4.31}$$

Substituting $\sigma_{xy}^{(1)}$ into (4.31) and evaluating at $y = h$ results in

$$-2\frac{\mathrm{d}h}{\mathrm{d}z}\sigma_p^{(0)} + h\frac{\mathrm{d}\left(p^{(0)} - \sigma_p^{(0)}\right)}{\mathrm{d}z} \mp \beta\left(\sigma_p^{(0)} + p^{(0)}\right) =$$
$$-\left[A(n+1, z) - A(n-1, z)\right] + hT\left[B'(n+1, z) + B'(n-1, z)\right]. \tag{4.32}$$

Recognising that the left-hand side of this equation is a function of z only, and $B'(n+1, z) = B'(n-1, z)$ (see equation (4.21)), we may write

$$-2\frac{\mathrm{d}h}{\mathrm{d}z}\sigma_p^{(0)} + h\frac{\mathrm{d}\left(p^{(0)} - \sigma_p^{(0)}\right)}{\mathrm{d}z} \mp \beta\left(\sigma_p^{(0)} + p^{(0)}\right) = g(z), \tag{4.33a}$$

$$A(n+1, z) - A(n-1, z) = 2hTB'(n-1, z) - g(z). \tag{4.33b}$$

For $A(\xi, z)$ to remain bounded in n, the right-hand side of equation (4.33b) must equal zero. The behaviour of B and B' will not become apparent until the next order of correction, which depends on $A(\xi, z)$ itself. Drawing from the non-hardening model in Chapter 3 and the similarities between hardening and non-hardening results (as will be demonstrated in the next section), it is likely that the discontinuity in $B(\xi)$ develops into an expansion fan. This implies that $B'(\xi, 0)$ is a piecewise function that varies with both n and z. In this case, the right-hand side of equation (4.33b) cannot be zero. Consequently, $A(\xi, z)$ grows to be $O(n) = O(1/\delta)$ and the asymptotic ordering we assumed in deriving our equations would be broken. For this reason, it is not obvious how to interpret equation (4.33b). In the non-hardening model explained in the previous chapter, in the absence of term $B'(n-1, z)$, the right-hand side of equation (4.33b) was set to zero. This condition ensured that $A(\xi, z)$ remained both periodic and bounded in n.

In the next section, we compare FE results from Abaqus for a 25% reduction from both hardening and non-hardening materials. Observing similar stress and velocity oscillations in both cases—which, based on equations (4.20) and (4.30), can be interpreted as similar solutions for $B(\xi, z)$ and $A(\xi, z)$ as non-hardening—we then apply the solution derived in Chapter 3, along with the leading-order solution presented here, to obtain the full solution for the hardening case. Yet, this is only an approximate solution, and a more comprehensive solution would involve determining $B(\xi, z)$ and $A(\xi, z)$ independently of the non-hardening solution. Given the contradiction explained regarding equation (4.33b), achieving this may necessitate adopting a different scaling approach; for instance, the coefficient of friction could be scaled independently of δ, as suggested by Johnson and Smelser (1992); alternatively, scaling $\mathrm{d}\hat{h}/\mathrm{d}\hat{x}$ with $r\delta$ might lead to a more simplified solution, particularly under the condition where both the reduction and δ are small, aligning with the limit used here for showcasing the results.

4.4 Simulation results

For a better understanding of the effect of hardening on stress and velocity distribution, the Abaqus/Standard package is used to model the rolling process. The full details are given by Flanagan et al. (2024), and the summary of simulations are provided in Section 2.5 in Chapter 2.

Two different material models are used; One with the yield stress fixed, so that the simulation is close to the perfectly plastic material; and the other with a more typical hardening profile. The data point used for hardening in FE simulations and the function fitted based on equation (4.3) is plotted in Figure 4.1.

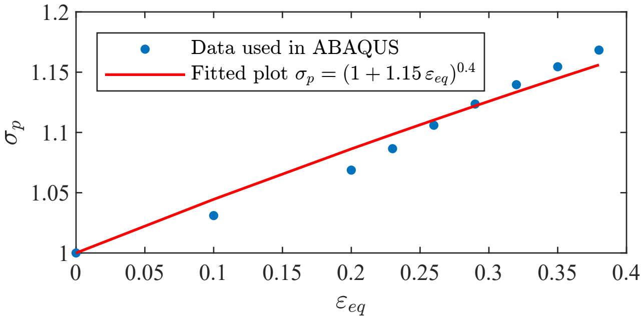

Figure 4.1: Hardening data used in Abaqus simulations and the fitted curve based on equation (4.3). Results are shown in dimensionless form, i.e. scaled with $\hat{Y} = 275.51 * \sqrt{3}\,\mathrm{MPa}$, the yield strength.

Figure 4.2 compares horizontal stress, hydrostatic pressure, and shear stress, from Abaqus simulations for hardening and non-hardening material for $\delta = 0.125$ and $r = 25\%$. Although the yielding condition differs, the distribution pattern remains largely similar between the non-hardening and hardening cases. As expected, the magnitude is greater in the hardening case, particularly toward the exit, which is evident from the darker contour colours when compared to the non-hardening contour plots. This can be understood better in Figure 4.3 where the hydrostatic pressure, $-p$, and shear, σ_{xy}, profiles are investigated at different through-thickness heights for the hardening and non-hardening cases for two different aspect ratios.

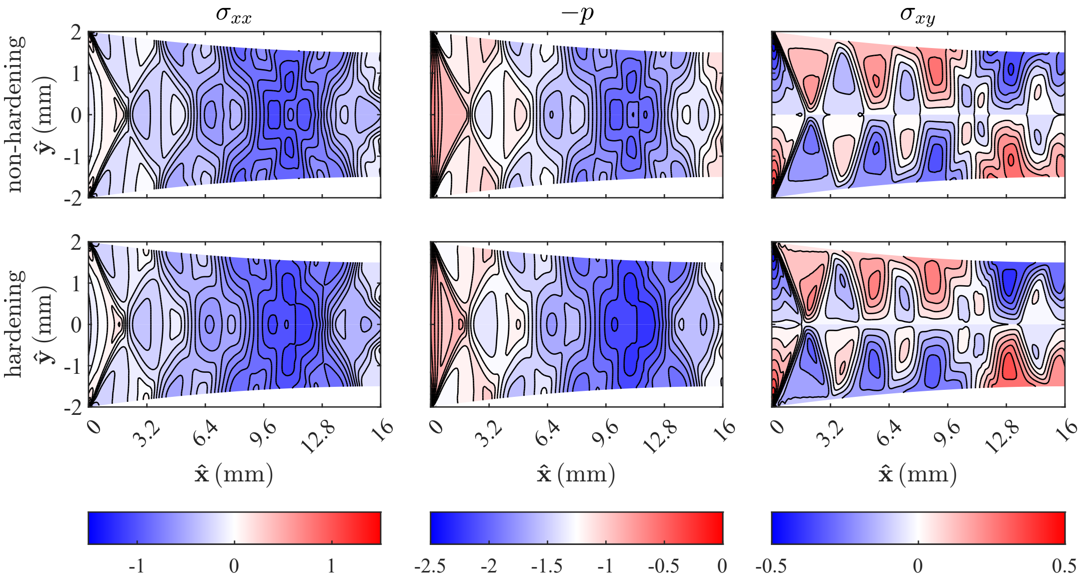

Figure 4.2: FE simulations (Flanagan et al., 2024) for non-hardening (top) and hardening (bottom) for $\delta = 0.125$. Left: contour plots of horizontal stress. Middle: contour plots of pressure. Right: contour plots of shear stress. Results are shown in dimensionless form, i.e. scaled with $\hat{\kappa}$, the yield stress in shear. Parameters used are $(\hat{h}_0, r, \mu, \hat{\kappa}) = (2\,\text{mm}, 25\%, 0.1, 275.51\,\text{MPa})$.

The average pressure resembles a pressure hill, with the maximum occurring at the neutral point. Hardening modifies the average pressure curve by increasing the values and shifting the neutral point slightly toward the exit. Surface pressure also shows an increase as a result of hardening as expected, but the oscillatory pattern seems to remain similar for hardening and non-hardening. To further investigate this, the pressure at different heights (surface, $y = 2h/3$ and $y = h/3$) is subtracted from the average pressure and shown in the middle row in Figure 4.3. The average pressure in the current model is the leading-order solution; therefore, by subtracting the total pressure from the average pressure, the correction terms causing the oscillations remain (see equation (4.30a)). A very similar trend observed for hardening and non-hardening material in the middle row in Figure 4.3 implies that the correction terms for pressure solution are not significantly affected by hardening. This observation may suggest that to determine the pressure in rolling with a hardening material, only the leading-order solution needs to be adjusted, while the correction terms remain mostly unchanged from the non-hardening model.

Shear stress on the surface and at $2h/3$ for hardening and non-hardening material is shown in the last row of Figure 4.3. The plot for $h/3$ is close to the $2h/3$ plot and is omitted for clarity. Similar to pressure, hardening seems to have a negligible impact on oscillations, and a slight increase in magnitude in the case of hardening material might be the effect of the leading-order pressure on the shear solution (see the last term in equation (4.30b)).

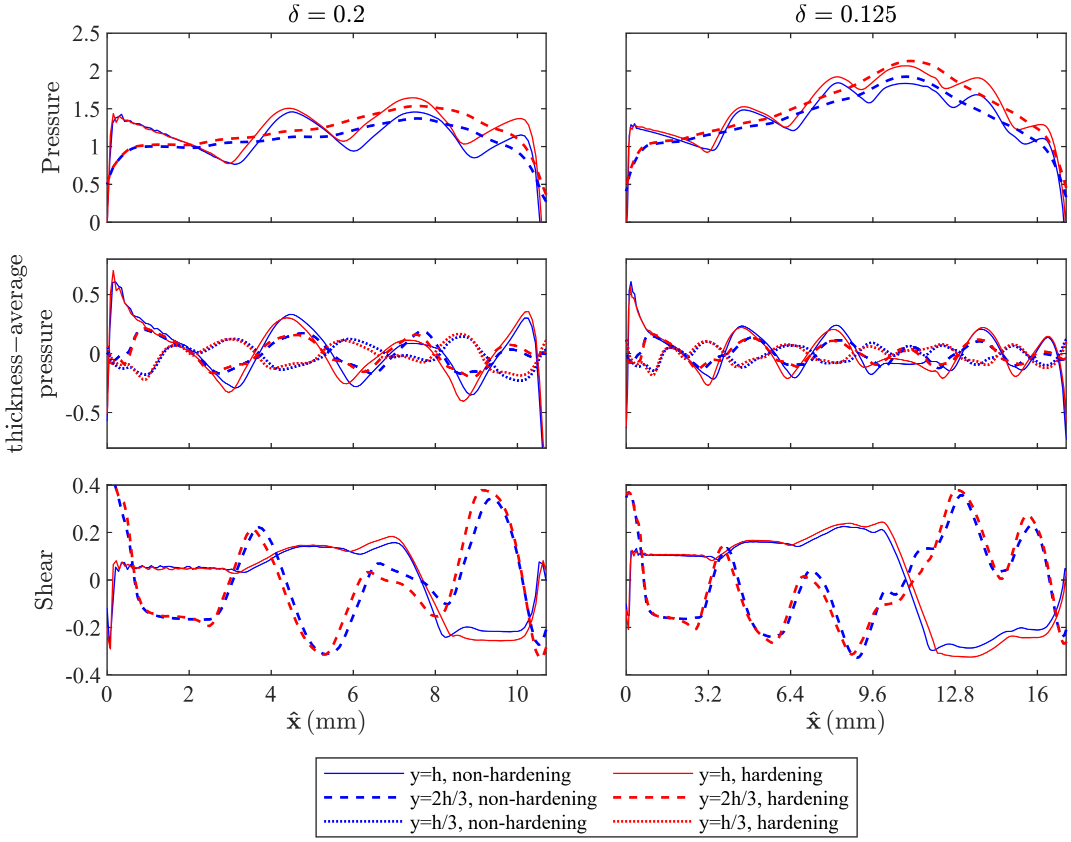

Figure 4.3: Pressure (p) and shear stress (σ_{xy}) for hardening (red curves) and non-hardening (blue curves) materials at different through-thickness heights from FE simulations (Flanagan et al., 2024). Results are shown in dimensionless form, i.e., scaled with $\hat{\kappa}$, the yield stress in shear. Parameters used are $(\hat{h}_0, r, \mu, \hat{\kappa}) = (2\,\text{mm}, 25\%, 0.1, 275.51\,\text{MPa})$.

Figure 4.4 compares velocities for hardening and non-hardening materials from FE simulations. Aside from the minor variations in vertical velocity results, both cases exhibit a very similar trend. In Abaqus/Standard, velocity is computed based on the change in displacement between time intervals, making it sensitive to the selected time frame in the simulation. Thus, the observed differences are more likely the result of this dependency than a fundamental difference in the solution. Moreover, while hardening is expected to influence stresses, it should have little effect on strain rates and, consequently, velocities. This can also be seen from Figure 4.5 where the horizontal and vertical velocities are plotted at different thicknesses (surface, $2h/3$, and $h/3$) for hardening and non-hardening materials.

It should be noted that the similarity observed between the stress and strain

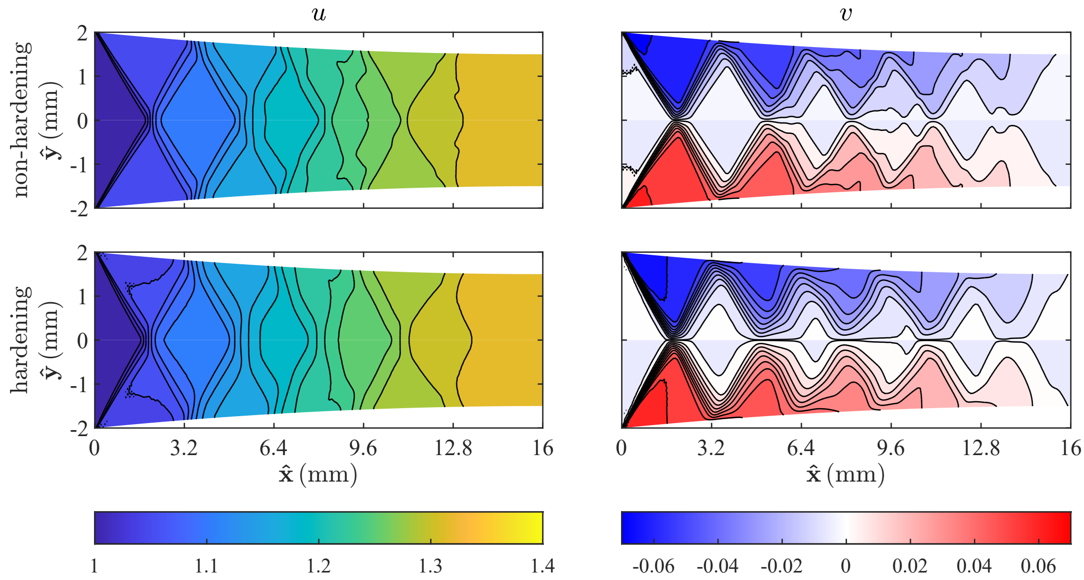

Figure 4.4: FE simulations (Flanagan et al., 2024) for non-hardening (top) and hardening (bottom) for $\delta = 0.125$. Left: contour plots of horizontal velocity. Right: contour plots of vertical velocity. Results are shown in dimensionless form, i.e. scaled with the sheet entrance velocity. Parameters used are $(\hat{h}_0, r, \mu, \hat{\kappa}) = (2\,\text{mm}, 25\%, 0.1, 275.51\,\text{MPa})$.

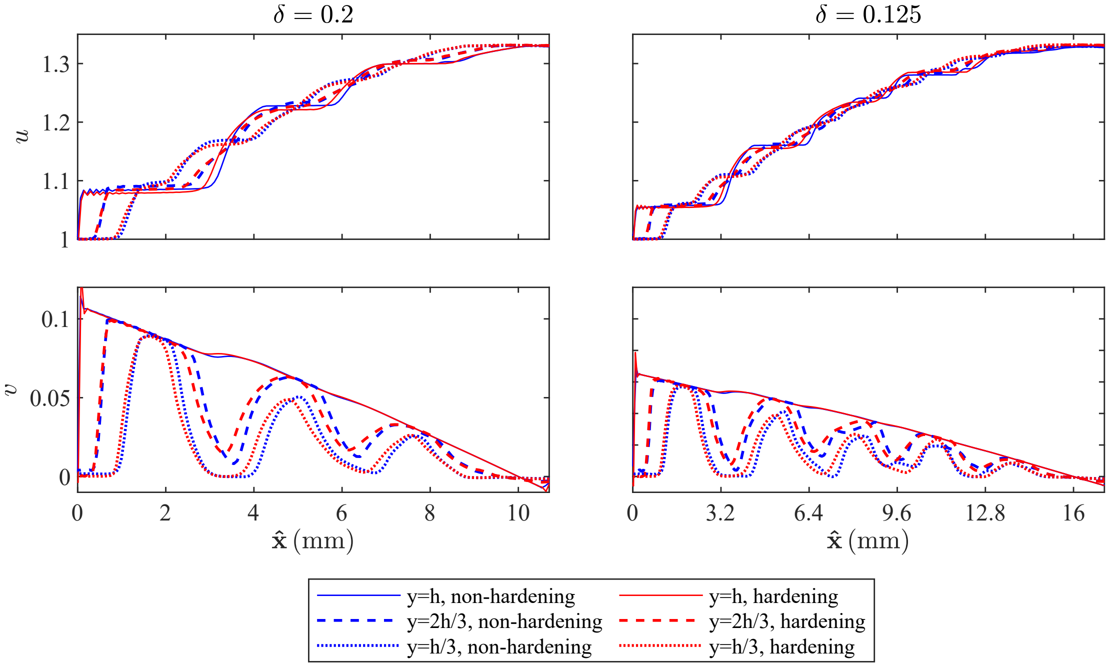

Figure 4.5: Horizontal velocity (u) and vertical velocity (v) for hardening (red curves) and non-hardening (blue curves) material at different through-thickness heights from FE simulations (Flanagan et al., 2024). Left: $\delta = 0.2$ (left); Right: $\delta = 0.125$. Results are shown in dimensionless form, i.e., scaled with the sheet entrance velocity. Parameters used are $(\hat{h}_0, r, \mu, \hat{\kappa}) = (2\,\text{mm}, 25\%, 0.1, 275.51\,\text{MPa})$.

oscillations in hardening and non-hardening cases may result from the relatively small friction and reduction ratios used in the simulations. While further simulations are required to draw a definitive conclusion, the equations are further simplified in the following section based on the current observations.

4.5 Comparison of model with the simulation results

To fully compare the model with the FE simulations, the unknown parameters $p^{(0)}$, $A(\xi, z)$ and $B(\xi, z)$ must first be determined. However, the solution process encounters difficulties with equation (4.33b). The complexity arises from the terms $B'(\xi, z)$ resulting from the effect of $\sigma_p^{(1)}$. In the previous section, it was demonstrated that the oscillatory stress patterns were almost similar for both hardening and non-hardening materials, suggesting that the effect of $\sigma_p^{(1)}$ on the stresses is negligible.

Consequently, we disregard $\sigma_p^{(1)}$ in the stress calculations and simplify equation 4.30 to

$$p^{(1)} = A\left(n + \frac{y}{h}, z\right) + A\left(n - \frac{y}{h}, z\right), \tag{4.34a}$$

$$\sigma_{xy}^{(1)} = A\left(n + \frac{y}{h}, z\right) - A\left(n - \frac{y}{h}, z\right) + y\frac{\mathrm{d}\left(p^{(0)} - \sigma_p^{(0)}\right)}{\mathrm{d}z}, \tag{4.34b}$$

which has a similar form to the non-hardening case. Also, by assuming that $A(\xi, z)$ has the same properties as in the non-hardening case, specifically that $A(\xi, z)$ remains bounded in n, we can set $g(z) = 0$. This simplifies equation 4.33a to

$$-2\frac{\mathrm{d}h}{\mathrm{d}z}\sigma_p^{(0)} + h\frac{\mathrm{d}\left(p^{(0)} - \sigma_p^{(0)}\right)}{\mathrm{d}z} \mp \beta\left(\sigma_p^{(0)} + p^{(0)}\right) = 0, \tag{4.35}$$

where using the entrance and exit boundary conditions (4.19), $p^{(0)}$ is determined by integrating equation (4.35). In this way, by ignoring any effect of hardening terms smaller than the leading order and following the same procedure as outlined in Chapter 3, the same Burgers' equation will be derived to describe the evolution of $A(\xi, z)$, while the $p^{(0)}$ term in Burgers' equation is obtained from (4.35).

In summary, the asymptotic solution for pressure is equal to

$$p = p^{(0)} + \delta p^{(1)} + O(\delta^2), \tag{4.36}$$

where $p^{(0)}$ is solved from (4.33a) and $p^{(1)}$ from equations (4.34a) and $A(\xi, z)$ from (3.55). Similarly, the asymptotic shear is equal to

$$\sigma_{xy} = \delta\sigma_{xy}^{(1)} + \delta^2\sigma_{xy}^{(2)} + O(\delta^3), \tag{4.37}$$

where $\sigma_{xy}^{(1)}$ is calculated from equations (4.34b), and $\sigma_{xy}^{(2)}$ is calculated only on the surface, with the same equation as non-hardening;

$$\sigma_{xy}^{(2)} = \mp\beta\left(-p^{(1)}\right). \tag{4.38}$$

The negligible effect of $\sigma_p^{(1)}$ on stress calculations can be justified from the equations. The solution to $\sigma_p^{(1)}$ is proportional to $u^{(1)}$, where $u^{(1)}$ represents a correction in the order of $\mathrm{d}h/\mathrm{d}z$ (see equation (4.22)). The term $\mathrm{d}\hat{h}/\mathrm{d}\hat{z}$ is scaled with δ, and consequently, $\mathrm{d}h/\mathrm{d}z$ is $O(1)$. Under this scaling, no restriction is imposed on the reduction ratio, r. However, if r is small, as chosen in the current FE simulations, then $\mathrm{d}h/\mathrm{d}z$ becomes $O(r)$ and is therefore small. This is also evident in Figure 4.4, where the oscillations in $u^{(1)}$ are relatively small compared to those observed in pressure. This suggests that $\sigma_p^{(1)}$ is small in magnitude and, therefore, regardless of its oscillatory pattern (which resembles that of the horizontal velocity), it cannot alter the predominant stress distribution.

However, as hardening is homogeneous at leading order, a negligible non-homogeneous oscillatory correction can still influence the final distribution (similar to the effect of $u^{(1)}$ on the velocity profile). Therefore, the correction term is retained in the solution for σ_p, and we write

$$\sigma_p = \sigma_p^{(0)} + \delta\sigma_p^{(1)} + O(\delta^2), \tag{4.39}$$

where $\sigma_p^{(0)}$ and $\sigma_p^{(1)}$ are calculated from (4.26). $B(\xi, z)$ is as-yet-unknown in $\sigma_p^{(1)}$. Given the similar velocity distributions in Figure 4.5, along with the identical velocity expressions ((4.20)) for both non-hardening and hardening materials, we assume that the same advection equation governs $B(\xi, z)$ in both cases. The only difference is that $p^{(0)}$ in the advection equation (3.59) is now calculated for the hardening material.

4.5.1 Through-thickness distribution

The contour plots of hydrostatic pressure, shear stress, and hardening for $\delta = 0.125$ are shown in Figure 4.6 and compared with FE simulations for hardening material. The asymptotic model successfully predicts both the magnitude and distribution patterns of all components. The good agreement between the model and simulation confirms the validity of the model and the assumptions made. The oscillatory pattern observed for hardening closely resembles that of the horizontal velocity, as predicted by equation (4.26), indicating that the material does not harden uniformly through the thickness.

Figure 4.7 presents the pressure and shear stress on the surface and compares them with FE simulations for the hardening material. The asymptotic leading-order solution for pressure shows good agreement with the average pressure from FE, confirming the validity of equation (4.35) for determining the leading-order pressure. With zero exit tension, the leading-order pressure at the exit is dictated by $\sigma_p^{(0)}$ (see equa-

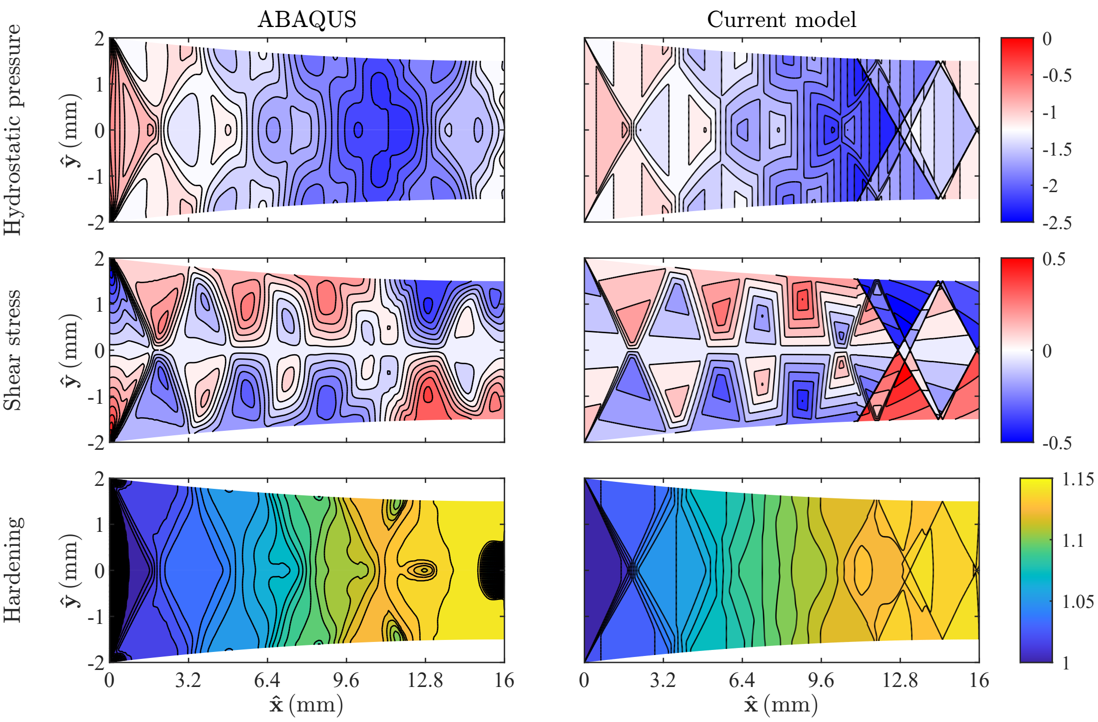

Figure 4.6: Comparison of results for hardening material from the current model (right) with FE simulations (Flanagan et al., 2024) (left) for $\delta = 0.125$. Results are shown in dimensionless form, i.e., scaled with $\hat{\kappa}$, the yield stress in shear. Parameters used are $(\hat{h}_0, r, \mu, \hat{\kappa}) = (2\,\text{mm}, 25\%, 0.1, 275.51\,\text{MPa})$.

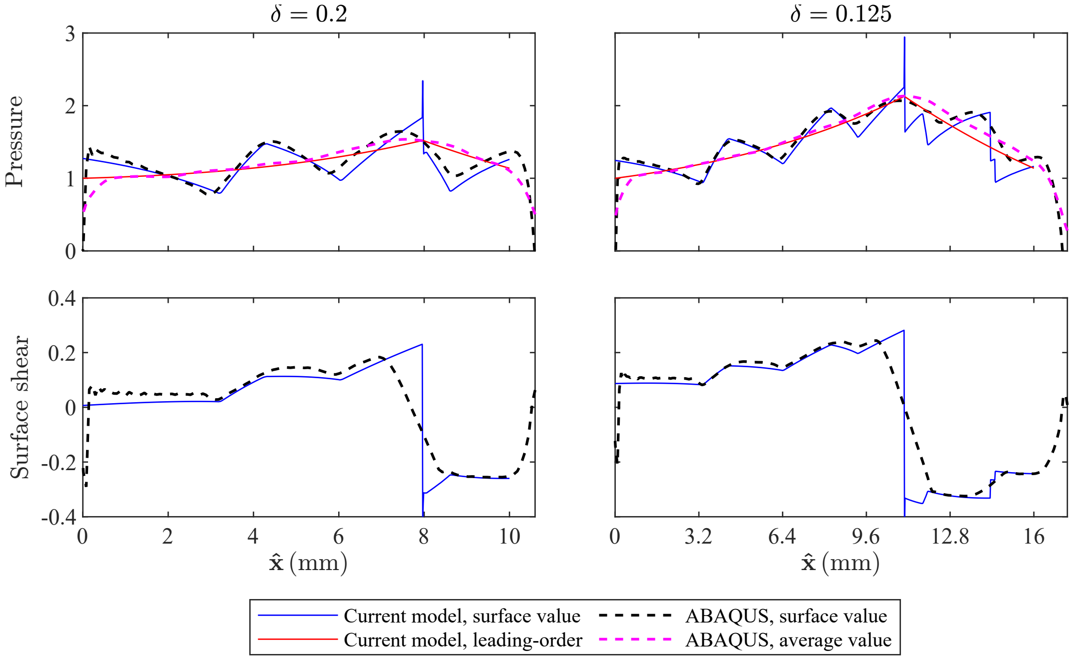

Figure 4.7: Plots of p (top) and σ_{xy} (bottom) on the surface for hardening material, plotted as a function of distance through the roll gap, for $\delta = 0.2$ (left) and $\delta = 0.125$ (right). Results are shown in dimensionless form, i.e. scaled with $\hat{\kappa}$, the yield stress in shear. Other parameters used are $(\hat{h}_0, r, \mu, \hat{\kappa}) = (2\,\text{mm}, 25\%, 275.51\,\text{MPa})$.

tion (4.15)). This value is accurately predicted for $\delta = 0.2$ but slightly underestimated for $\delta = 0.125$. The surface pressure and shear stress also align well with the asymptotic model. Yet, using the same friction model as in the previous chapter, a similar discontinuity is observed at the neutral point.

4.5.2 Roll force and torque

To evaluate the performance of the hardening model in predicting roll force and roll torque, the predictions are compared with those of the perfectly plastic asymptotic model from Chapter 3 and the perfectly plastic slab method from Chapter 2, as well as with the FE results for the hardening material, as shown in Table 4.1 and Table 4.2. The colour of each cell represents the error compared with Abaqus results, with the five different shades of green indicating errors from 0% to 9%, yellow representing 10%, and the three shades of orange denoting errors from 11% to 16%. Since the yield strength is constant in the perfectly plastic models, the results are calculated for two different yield strengths: $\hat{\kappa} = 275.51\,\text{MPa}$, the initial yield strength of the material, and $\hat{\kappa} = 294.55\,\text{MPa}$, the average yield strength during the process.

Table 4.1: Roll force (MN per unit width)

δ	Hardening		Perfect plastic			
			Asymptotics		Slab method	
	Abaqus	Current model	$\kappa=294.55$	$\kappa=275.51$	$\kappa=294.55$	$\kappa=275.51$
0.5	2.54	2.41	2.34	2.19	2.44	2.28
0.3	4.31	4.11	4.06	3.80	4.16	3.89
0.2	6.74	6.26	6.23	5.83	6.28	5.87
0.175	7.95	7.45	7.38	6.90	7.42	6.94
0.125	12.19	11.29	11.18	10.46	11.37	10.63
0.075	24.76	22.97	22.53	21.07	22.62	21.16

Table 4.2: Roll torque (KNm per unit width)

δ	Hardening		Perfect plastic			
			Asymptotics		Slab method	
	Abaqus	Current model	$\kappa=294.55$	$\kappa=275.51$	$\kappa=294.55$	$\kappa=275.51$
0.5	5.42	5.62	5.65	5.29	4.86	4.54
0.3	15.10	15.70	15.97	14.94	13.62	12.74
0.2	31.39	32.14	31.92	29.85	30.75	28.77
0.175	40.88	42.47	42.70	39.94	41.22	38.56
0.125	86.83	89.77	89.68	83.88	87.35	81.71
0.075	289.34	299.57	303.03	283.45	290.06	271.32

0 1	2 3	4 5	6 7	8 9	10	11 12	13 14	15 16

From Table 4.1, roll force is accurately predicted by the current hardening model, with deviations from FE simulations remaining below 7% across different aspect ratios.

Regardless of the model used, calculating roll force with the initial yield strength results in significant errors when hardening is ignored. Predictions from perfectly plastic models, including the slab method, can be improved by employing the average yield strength. However, determining the average yield strength requires knowledge of the yield value at the end of the roll gap, which is calculated here using equation (4.26a). The results for roll torque are shown in Table 4.2. The current hardening model slightly overestimates roll torque, with a maximum 4% error across various roll-gap aspect ratios. Similar to roll force prediction, using the average yield strength with perfectly plastic models can improve torque prediction.

In summary, when the aim is predicting roll force and torque, the current hardening model is effective, whether used to directly predict stresses or to determine the average yield stress during the process to be combined with perfectly plastic models, including the slab method.

4.6 Conclusion

Building on the same assumptions as those in Chapter 3, the asymptotic model has been extended to include isotropic hardening, with hardening expressed as a power law. The added complexity in the equations due to hardening limits the derivation of a complete solution. However, further approximations supported by Abaqus results enable the derivation of the solution. A comparative FE analysis of hardening and non-hardening materials reveals that hardening increases the magnitude of stress without significantly altering stress oscillation patterns, and that the velocity distribution remains nearly unaffected by hardening. These findings suggest that $\sigma_p^{(1)}$ is neglegible. Therefore, to account for hardening effects in this chapter, only the leading-order solution and its related terms are modified, while the oscillatory terms are calculated using the asymptotic non-hardening model for perfectly plastic materials presented in Chapter 3. It should be noted that this approximation is based on the analysis of FE simulations with weak shear ($\mu = 0.1$ and $r = 25\%$), and further simulations are necessary to validate the assumption under large shear conditions.

The through-thickness hardening and stress predictions from the current model align well with the FE results. Similarly, the model accurately captured the surface shear and pressure, supporting the validity of the assumptions and equations. Still, focusing on developing a mathematically consistent approach to model hardening could be a valuable direction for future work.

Roll force and roll torque are compared for both hardening and non-hardening materials. Roll force and roll torque are closely predicted by the current hardening model, with deviations from FE simulations kept under 7% for roll force and 4% for roll torque for various roll-gap aspect ratios. For cases without hardening, roll force predictions based on the initial yield strength show significant errors, while roll torque is less sensitive to hardening effects. Predictions from perfectly plastic models, including the slab method, can be improved by using the average yield strength value. For this, the leading-order solution for hardening can be used to find the final yield strength.

Chapter 5

Mathematical model of wire flat rolling

A mathematical model for flat rolling of wire is introduced in this chapter. The governing equations in all directions are formulated for rigid perfectly plastic material and simplified using the same small parameters as those used in sheet rolling, namely, the ratio of half thickness to the length and the friction coefficient, along with the additional small lateral spread assumption. These assumptions reduce the general state of deformation to plane-stress deformation, formulated in Section 5.2 and then solved for the leading order in Section 5.3.

The model has been implemented in MATLAB, and results are validated against FE data from the literature as well as experimental data, obtained by a collaborator, in Section 5.4.1 and 5.4.2 for roll pressure and lateral spread, respectively.

5.1 Introduction

Applications including sawblades, springs, piston rings, and transformers depend critically on flattened wires (Utsunomiya et al., 2001). These wires are usually made by a flat rolling technique where a wire with a circular cross-section is cold rolled between cylindrical rolls—sometimes through several passes—to get a particular width (Figure 5.1). Achieving a final product that closely matches the desired specifications requires an understanding of how the wire deforms, making it essential to predict the lateral spread accurately.

In cold rolling of a sheet, deformation in the lateral direction often remains within the elastic range due to the product's geometry. However, this is not the case when an initial width-to-thickness ratio ($W_0/2h_0$) is less than 6, say as low as 1 as such in plate rolling or wire flat rolling (Chitkara and Johnson, 1966). In such cases, the plastic flow in the roll gap at the start of rolling schedules is inherently three-dimensional, complicating the analysis. For round wire, this complexity is further increased by the transformation

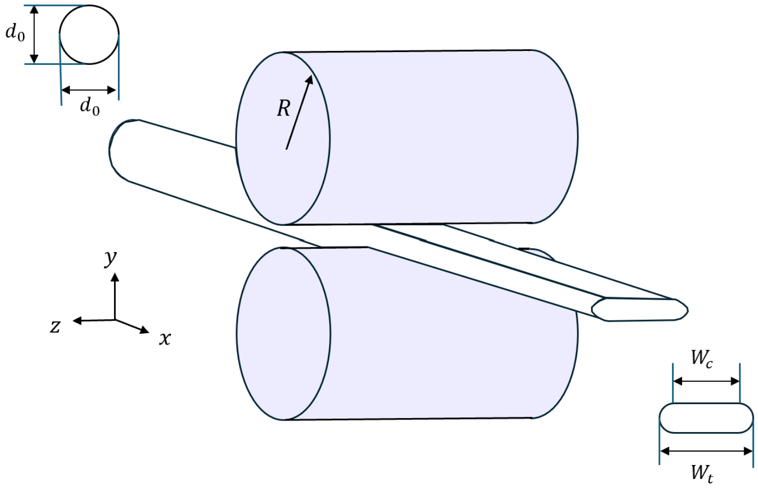

Figure 5.1: A diagram of wire flat rolling process; the wire initially has a circular cross-section and is flattened to a rectangular shape with round edges. Adapted from Carlsson (1998)

of a round cross-section into a rectangular shape with bulged edges during a single pass.

Although some old research has been done on modelling of the lateral spread in thick plate rolling (Oh and Kobayashi, 1975; Kennedy, 1987; Lahoti and Kobayashi, 1974; El-Nikhaily, 1979), wire flat rolling clearly receives less attention. Kazeminezhad and Taheri published a series of papers studying different parameters in wire rolling (Kazeminezhad and Taheri, 2005, 2006; Kazeminezhad et al., 2008). In (Kazeminezhad and Taheri, 2005), the authors developed a relationship for the width of the contact area between the rolls and the wire. Their equation was based on experimental and FE observations of the formation of X-shaped shear bands in the wire cross-section during the rolling process (Semiatin and Jonas, 1984; Pesin et al., 2002), along with the assumption that as the height reduction increases, the shear bands rotate while maintaining a constant length. This equation is then used together with the slab method in (Kazeminezhad and Taheri, 2006) to find the roll pressure. With the assumptions of small friction coefficient, μ, and roll angle, ϕ, they wrote the force balance in the rolling direction as

$$hW_c\frac{\mathrm{d}\sigma_{xx}}{\mathrm{d}x} + W_c\,\sigma_{xx}\frac{\mathrm{d}h}{\mathrm{d}x} + h\sigma_{xx}\frac{\mathrm{d}W_c}{\mathrm{d}x} + W_c\,\sigma_{yy}\tan\phi \mp \mu\sigma_{yy}W_c = 0, \tag{5.1}$$

where h is the half height of wire, W_c is the contact width, and $\mp = \mathrm{sgn}(x - x_\mathrm{N})$ gives the direction of the friction force before and after the neutral point x_N. This equation is then solved coupled with the Tresca yield criterion, where σ_{xx} is assumed to be the minimum stress and σ_{yy} to be the maximum stress and the compressive stress in the lateral direction, σ_{zz} to have a value between them as

$$\sigma_{xx} - \sigma_{yy} = 2\kappa, \tag{5.2}$$

resulting in a pressure hill distribution. Although σ_{zz} is implicitly included in the yield function, and therefore in calculating the roll pressure, since the value of σ_{zz} is unknown, it must be approximated to find the lateral spread. In (Kazeminezhad and Taheri, 2005), they assumed σ_{zz} to take a value between plane strain and plane stress and written as $m\sigma_{yy}$ where m varies from 0 to 0.5. Using flow rule equations and setting σ_{xx} to be zero at the end of the roll gap, they then wrote

$$\frac{d\varepsilon_{zz}}{-d\varepsilon_{yy}} = \frac{\ln \frac{W_t}{d_0}}{\ln \frac{d_0}{2h_1}} = \frac{1-2m}{2-m}, \tag{5.3}$$

where $2h_1$ is the final height, d_0 is the diameter of the wire and W_t is the lateral spread of the wire. This formulation was first used by Hill for plate rolling and has also been derived by several authors (Chitkara and Johnson, 1966; McCrum, 1956; Wusatowski, 1969; Group and Sparling, 1961), who experimentally observed a linear relationship between $\ln(W_t/W_0)$ and $\ln(h_0/h_1)$. Factor m and another factor of linearity then must be found from experiments with a payoff that each resulting equation only gives reasonable lateral spread prediction within the ranges of conditions for which they were empirically determined (Chitkara and Johnson, 1966). For low and high carbon steel Kazeminezhad and Taheri (2005) wrote equation (5.3) as

$$\frac{W_t}{d_0} = 1.02\left(\frac{d_0}{2h_1}\right)^{0.45}. \tag{5.4}$$

Among a wide range of empirical formulations suggested for predicting lateral spread, the one proposed by Kobayashi (1978) is often referred to as being reliable (Kazeminezhad et al., 2008; Utsunomiya et al., 2001; Vallellano et al., 2008). In (Vallellano et al., 2008; Utsunomiya et al., 2001), the following equation is attributed to Kobayashi and will be referred to by the same name throughout this chapter.

$$\frac{W_t}{d_0} = 0.7854\left(\frac{d_0}{2h_1}\right)\left(1-15.8\left(1-\left(\frac{2h_1}{d_0}\right)\right)^{2.25}\left(\frac{2R}{d_0}\right)^{-0.82}\right)+0.1426\left(\frac{2h_1}{d_0}\right), \tag{5.5}$$

where R is the roll radius.

Similar to other metal-forming processes, the application of FE analysis has provided insights into the stress distribution in the rolling of wire. A three-dimensional (3D) numerical study conducted using Abaqus software by Carlsson (1998) and Vallellano et al. (2008) revealed that the contact pressure distribution is more complex than the traditional pressure hill profile. Their results showed a well-defined peak in the entry zone in the rolling direction followed by a valley and another peak at the location of the neutral point for long enough roll gaps. In the lateral direction, pressure distribution showed decay to zero from the central line to the lateral edges, but with a peak happening just before the contact edges (see Figure 5.2).

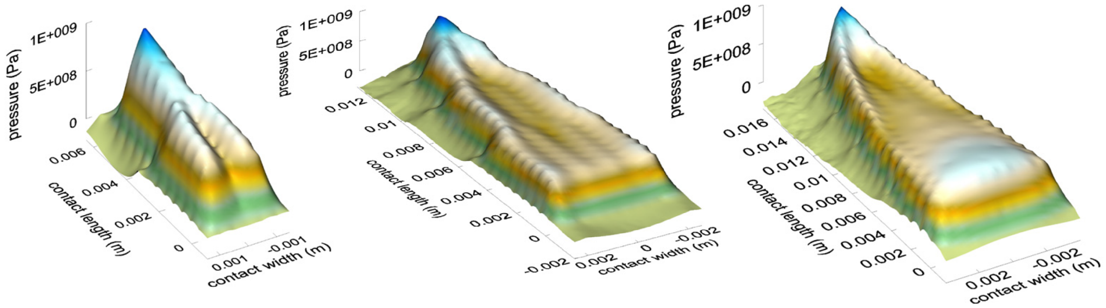

Figure 5.2: Distributions of the contact pressure for 5 mm wire diameter with different reductions from Abaqus simulations (Vallellano et al., 2008), left: r=10.5%, middle: r=40%, right: r=75%

Although 3D FE analysis provides highly detailed information, it is prohibitively expensive. Meanwhile, the search in the literature revealed a notable gap in the availability of mathematical models with clear, traceable assumptions for the rolling of round wire. Here, a simple mathematical model is presented to examine changes in the contact stresses and lateral spread in the rolling of round wire.

5.2 Governing equations

In the first pass of rolling, the round wire undergoes deformation, resulting in a barrel-like cross-section. With the goal of the simplest possible model, instead of a circular cross-section, a square cross-section is assumed, which progressively flattens into a rectangular shape as rolling continues. From this assumption, two possible modelling cases emerge.

In the first case, it is assumed there exists a point after the entrance where the initial circular cross-section of wire has turned into a rectangular cross-section while the area is preserved. This stage is marked A, in Figure 5.3(***i***), and is chosen as the beginning of the roll gap in the model for case (***i***)). Therefore, we may write

$$\pi\hat{d}_0/4 = 4\hat{h}_0^2 \qquad\qquad \Rightarrow \qquad\qquad 2\hat{h}_0 = \frac{\sqrt{\pi}}{2}\hat{d}_0, \tag{5.6}$$

where $\hat{h}_0$ is the half thickness of the wire corresponding to location A. As the rolling progresses, it is assumed that the area of the rectangular cross-section in the model is the same as the area of the real cross-section, with the bulged edges (see Figure 5.3(***i***)).

Alternatively, in the second modelling case, the rolling of a round wire is assumed to be analogous to the rolling of a slab, such that the lateral spread of the slab matches the lateral spread of the wire at the same position in the rolling direction (see Figure 5.3(***ii***)). Therefore, in this case,

$$2\hat{h}_0 = \hat{d}_0, \tag{5.7}$$

where h_0 is the half thickness of the wire at the roll gap entrance.

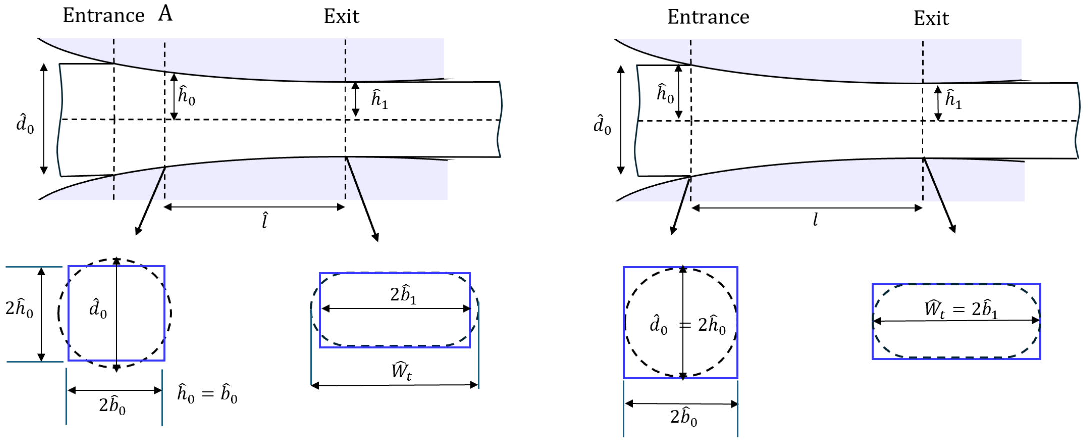

(i) ***(ii)***

Figure 5.3: A diagram of two modelling cases; ***(i)*** the volume is conserved, ***(ii)*** the lateral spread is conserved

Similar to the models for sheet rolling in Chapters 2 and 3, the rolls are assumed to be rigid, and the rolled material is represented as a non-hardening rigid perfectly plastic, while the Coulomb friction is imposed between the rolls and material with a constant friction coefficient.

5.2.1 Scaling and non-dimensionalising the equations

Similar to the sheet rolling, stress and strain oscillations are expected, which, as explained in Chapter 3, are captured in the first-order corrections through multiple scales. However, as will be explained later, the solution for wire rolling is derived only to the leading order. Consequently, the use of multiple scales is unnecessary. Instead, the horizontal distance is scaled with the characteristic roll-gap length, $\hat{\ell}$, such that $\hat{x} = \hat{\ell}x$, and the vertical distance with the initial sheet half-thickness, $\hat{h}_0$. Recall that $\hat{\ell}$ for circular rolls is equal to

$$\hat{\ell} = \sqrt{2\hat{R}\left(\hat{h}_0 - \hat{h}_1\right) - \left(\hat{h}_0 - \hat{h}_1\right)^2}, \tag{5.8}$$

where $\hat{h}_0$ and as a result, $\hat{\ell}$ are different in the modelling cases ***(i)*** and ***(ii)*** according to Figure 5.3.

Similar to sheet rolling, we are interested in small values of friction coefficient and $\delta = \hat{h}_0/\hat{\ell}$. The latter can be justified by the practical application of small wire diameters (less than a centimetre) and large reductions. For instance, applying a 100 mm roll diameter to an 8 mm wire diameter with a reduction of 0.3 results in $\delta = 0.37$. Any larger reduction and/or smaller wire diameter further decreases the value of δ. Here, a further assumption is made that the width, $\hat{b}(\hat{x})$, is of the order of magnitude of thickness. Therefore, the lateral distance $\hat{z}$ is scaled with the initial sheet half-thickness,

$\hat{h}_0$. In this way, with the assumption of the rectangular cross-section without considering barreling, z varies between $-b(x)$ and $b(x)$ where $b(x) = \hat{b}(\hat{x})/\hat{h}_0$.

Unlike the previous chapters where different components of the stress tensor were scaled with the same factor (so as the velocity vector), here they are scaled differently. The velocity $(\hat{u}, \hat{v}, \hat{w})$, is scaled with the entrance wire velocity and to balance incompressibility as $(\hat{R}\hat{U}_0, \delta\hat{R}\hat{U}_0, \delta\hat{R}\hat{U}_0)$. Hydrostatic pressure, $-\hat{p}$, and the normal Cauchy stresses, $\hat{\sigma}_{xx}$ and $\hat{\sigma}_{yy}$, and their deviatoric components, $\hat{s}_{xx}$ and $\hat{s}_{yy}$, are all scaled with shear yield stress, $\hat{\kappa}$. The assumption of a small friction coefficient is encoded by setting $\beta = \delta\mu$, where β is a quantity of approximate unit magnitude. Similarly, the shear stress, $\hat{\sigma}_{xy}$ is scaled with $\delta\hat{\kappa}$ resulting from small friction.

The boundary condition is analysed to determine the order of magnitude of stress components in the z-direction. To let the width of the sheet vary over the length of the roll gap, the lateral edges of the wire must be tension-free so that the material can move in this direction (z-direction). This condition may be written as $\boldsymbol{\sigma} \cdot \boldsymbol{s} = 0$, where $\boldsymbol{s}$ is the unit normal to the wire lateral edges. Therefore, at $z = b(x)$, $\boldsymbol{b} = (-\delta \mathrm{d}b/\mathrm{d}x, 0, 1)$ and we get

$$\delta \frac{\mathrm{d}b}{\mathrm{d}x} \sigma_{xx} = \hat{\sigma}_{xz}/\hat{\kappa}, \tag{5.9a}$$

$$\delta^2 \frac{\mathrm{d}b}{\mathrm{d}x} \sigma_{xy} = \hat{\sigma}_{yz}/\hat{\kappa}, \tag{5.9b}$$

$$\delta \frac{\mathrm{d}b}{\mathrm{d}x} \hat{\sigma}_{xz}/\hat{\kappa} = \hat{\sigma}_{zz}/\hat{\kappa}. \tag{5.9c}$$

where $\mathrm{d}b/\mathrm{d}x$, σ_{xx}, and σ_{xy} are written in their known dimensionless forms, and $\hat{\sigma}_{zz}$, $\hat{\sigma}_{xz}$, and $\hat{\sigma}_{yz}$, whose orders of magnitude are thus far unknown, are written in dimensional form. The set of equations 5.9 implies that $\hat{\sigma}_{xz}$ is $O(\delta)$ and the normal stress in the lateral direction, $\hat{\sigma}_{zz}$ and the shear stress component $\hat{\sigma}_{yz}$ are $O(\delta^2)$. Although this holds at the lateral edges, we assume these orders of magnitude apply throughout the modelling region. Consequently, $\hat{\sigma}_{zz}$ and $\hat{\sigma}_{yz}$ are scaled with $\delta^2\hat{\kappa}$, while $\hat{\sigma}_{xz}$ is scaled with $\delta\hat{\kappa}$. As will be shown later, this approach leads to the simplest yet consistent solution, where the horizontal velocity depends only on x. To complete the non-dimensionalisation of the problem, the plastic parameter, $\hat{\lambda}$, is scaled with $\hat{U}_0/\hat{\kappa}\hat{\ell}$.

Under the scaling introduced, the dimensionless form of force balance in different directions is

$$\frac{\partial \sigma_{xx}}{\partial x} + \frac{\partial \sigma_{xy}}{\partial y} + \frac{\partial \sigma_{xz}}{\partial z} = 0, \tag{5.10}$$

$$\delta^2 \frac{\partial \sigma_{xy}}{\partial x} + \frac{\partial \sigma_{yy}}{\partial y} + \delta^2 \frac{\partial \sigma_{yz}}{\partial z} = 0, \tag{5.11}$$

$$\frac{\partial \sigma_{xz}}{\partial x} + \frac{\partial \sigma_{yz}}{\partial y} + \frac{\partial \sigma_{zz}}{\partial z} = 0. \tag{5.12}$$

The dimensionless form of the incompressibility and flow rule relation are

$$
\begin{aligned}
\frac{\partial u}{\partial x} + \frac{\partial w}{\partial z} + \frac{\partial v}{\partial y} &= 0, && (5.13)\\
\frac{\partial u}{\partial x} &= \lambda s_{xx}, && (5.14)\\
\frac{\partial v}{\partial y} &= \lambda s_{yy}, && (5.15)\\
\frac{\partial w}{\partial z} &= \lambda s_{zz}, && (5.16)\\
\frac{\partial u}{\partial y} + \delta^2 \frac{\partial v}{\partial x} &= \delta^2 \frac{1}{2} \lambda \sigma_{xy}, && (5.17)\\
\frac{\partial u}{\partial z} + \delta^2 \frac{\partial w}{\partial x} &= \delta^2 \frac{1}{2} \lambda \sigma_{xz}, && (5.18)\\
\frac{\partial v}{\partial z} + \frac{\partial w}{\partial y} &= \delta^2 \frac{1}{2} \lambda \sigma_{yz}, && (5.19)
\end{aligned}
$$

where the deviatoric stresses s_{ij} is defined as

$$
\sigma_{ij} = s_{ij} - p\delta_{ij} \qquad \text{and} \qquad -p = \frac{1}{3}(\sigma_{xx} + \sigma_{yy} + \delta^2 \sigma_{zz}). \tag{5.20}
$$

From (5.20) it can be seen that to get a non-zero pressure at leading order, $\hat{s}_{zz}$ is also required to be the order of magnitude of $\hat{\kappa}$.

With the scaling introduced, the von Mises yield criterion will be

$$
(\sigma_{xx} - \sigma_{yy})^2 + (\sigma_{xx} - \delta^2 \sigma_{zz})^2 + (\sigma_{yy} - \delta^2 \sigma_{zz})^2 + 6\delta^2 \sigma_{xy}^2 + 6\delta^2 \sigma_{xz}^2 + 6\delta^4 \sigma_{yz}^2 = 6. \tag{5.21}
$$

The Coulomb friction condition on the roll surface $y = h(x)$ is exactly the same as in the previous chapters, expressed as

$$
\delta \frac{\mathrm{d}h}{\mathrm{d}x}(\sigma_{yy} - \sigma_{xx}) + \left(1 - \delta^2 \left(\frac{\mathrm{d}h}{\mathrm{d}x}\right)^2\right) \sigma_{xy} = \mp \delta\beta \left(\sigma_{yy} - 2\delta \frac{\mathrm{d}h}{\mathrm{d}x} \sigma_{xy} + \delta^2 \left(\frac{\mathrm{d}h}{\mathrm{d}x}\right)^2 \sigma_{xx}\right). \tag{5.22}
$$

Assuming non-dimensionalised tensions $F_{\text{in/out}}$ are applied at the entrance and exit, the horizontal stress must satisfy

$$
F_{\text{in/out}} = \int_{-b_{\text{in/out}}}^{b_{\text{in/out}}} \int_{-h_{\text{in/out}}}^{h_{\text{in/out}}} \sigma_{xx} \, \mathrm{d}y\mathrm{d}z, \tag{5.23}
$$

where $h_{\text{in}} = b_{\text{in}} = 1$ by our non-dimensionalisation, and h_{out} and b_{out} are half of the final thickness and width respectively. Integrating the mass conservation law in (5.13) from $y = -h(x)$ to $y = h(x)$ and $z = -b(x)$ to $z = b(x)$ yields

$$
\int_{-b(x)}^{b(x)} \int_{-h(x)}^{h(x)} u \, \mathrm{d}y\mathrm{d}z = 4. \tag{5.24}
$$

Finally, the no-flux constraint on the roll surface $y = h(x)$ and wire edges $z = b(x)$ leads to

$$v = \delta \frac{\mathrm{d}h}{\mathrm{d}x} u, \tag{5.25}$$

$$w = \delta \frac{\mathrm{d}b}{\mathrm{d}x} u. \tag{5.26}$$

5.3 Leading-order solution

From hydrostatic pressure (5.20) and yield function (5.21) at leading order, we have

$$\sigma_{xx}^{(0)} = -\frac{3p^{(0)}}{2} + \frac{\sqrt{4 - 3p^{(0)^2}}}{2}, \tag{5.27a}$$

$$\sigma_{yy}^{(0)} = -\frac{3p^{(0)}}{2} - \frac{\sqrt{4 - 3p^{(0)^2}}}{2}, \tag{5.27b}$$

$$s_{zz}^{(0)} = p^{(0)}. \tag{5.27c}$$

From the force balance in y direction (5.11), we have,

$$\frac{\partial \sigma_{yy}^{(0)}}{\partial y} = 0. \tag{5.28}$$

Using this condition along with (5.27) implies that $p^{(0)}$ and all normal stress components are vertically homogeneous which is the same as the slab method's assumption. We now show that these components are independent of z, as well, and only change along the rolling direction, x. From (5.17) and (5.18) $u^{(0)}$ is independent of y and z which along with the continuity equation (5.13) and (5.19) it can be inferred that $v^{(0)}$ is linear in y and $w^{(0)}$ is linear in z. Now the set of equations (5.14)-(5.16), where their left-hand sides are only functions of x while the stresses are functions of $p^{(0)}$ (equation (5.27)) shows that in order to a single value for $\lambda^{(0)}$ satisfies them all, $p^{(0)}$ must be a function of x only.

The force equilibrium in x direction (5.10) now can be integrated over z and y to give

$$h(x)b(x)\sigma_{xx}^{(0)}(x) + b(x)\sigma_{xy}^{(0)}(x, h(x)) + h(x)\sigma_{xz}^{(0)}(x, b(x)) = 0, \tag{5.29}$$

where $\sigma_{xy}^{(0)}(x, h(x)$ and $\sigma_{xy}^{(0)}(x, b(x))$ can be found from the boundary conditions (5.22) and (5.9a), respectively. We therefore have

$$hb\frac{\mathrm{d}\sigma_{xx}^{(0)}}{\mathrm{d}x} + \sigma_{xx}^{(0)}\left(b\frac{\mathrm{d}h}{\mathrm{d}x} + h\frac{\mathrm{d}b}{\mathrm{d}x}\right) - b\sigma_{yy}^{(0)}\frac{\mathrm{d}h}{\mathrm{d}x} \mp \beta\sigma_{yy}^{(0)} b = 0. \tag{5.30}$$

This is the same equation as equation (5.1) driven by the slab method in Kazeminezhad and Taheri (2006). However, this work deviates from their model in defining the relation between $\sigma_{xx}^{(0)}$ and $\sigma_{yy}^{(0)}$. In Kazeminezhad and Taheri (2006), σ_{xx} is assumed to be the minimum stress and σ_{yy} to be the maximum stress and σ_{zz} to have a value between them. The use of non-dimensionalised Tresca yield criterion then resulted in $\sigma_{xx} - \sigma_{yy} = 2$. In the current work, however, $\hat{\sigma}_{zz}$ is assumed to be zero at leading order, and the use of von Mises criterion led to relation (5.27) between σ_{xx} and σ_{yy}.

The complexity of setting σ_{zz} non-zero at leading order is twofold; first, the governing equations require σ_{zz}, and consequently σ_{xx} and σ_{yy}, to depend on z at leading order, significantly complicating their solution. In Kazeminezhad and Taheri (2006), normal stresses are instead assumed to depend only on x, meaning only the average values over the z-direction are considered; second, for predicting the lateral spread, still the knowledge of σ_{zz} is required, even when using the averaged values. This limitation is evident in the presence of an unknown factor, m, in the expression for lateral spread proposed by Kazeminezhad and Taheri (2005), which must be determined by fitting experimental data. To avoid the complexities associated with non-zero σ_{zz} at leading order, the current model sets $\sigma_{zz} = 0$ at this order, as a direct consequence of the assumption that $\partial b/\partial x = O(\delta)$. This simplification enables the prediction of roll pressure and lateral spread without the need for parameter fitting (the constants in equations (5.4) and (5.5)). Nonetheless, having formulated stress and strain equations in all directions lays the groundwork for a more general model, where normal stresses vary in both the lateral and roll directions, which can be a topic for future research.

Equation (5.30) provides an ODE for $p^{(0)}$ and $b(x)$, when combined with stress equations (5.27). Another ODE is resulting from the velocity equations. The mass balance requires that

$$u^{(0)}(x) = \frac{1}{b(x)h(x)}. \tag{5.31}$$

From the tension flow rule in y direction (5.15) we have

$$v^{(0)} = y\lambda^{(0)} s_{yy}^{(0)}. \tag{5.32}$$

This, along with the no-penetration on the surface condition (5.25), results in

$$\lambda^{(0)} = \frac{\mathrm{d}h/\mathrm{d}x}{bh^2 s_{yy}^{(0)}}. \tag{5.33}$$

Similarly, from the tension flow rule in z direction (5.16) coupled with no-flow on the edge condition (5.26) we have

$$\lambda^{(0)} = \frac{\mathrm{d}b/\mathrm{d}x}{b^2 h p^{(0)}}. \tag{5.34}$$

Matching (5.33) and (5.34) gives an ODE for $b(x)$ as

$$\frac{\mathrm{d}b}{\mathrm{d}x} = \frac{b}{h}\frac{\mathrm{d}h}{\mathrm{d}x}\frac{p^{(0)}}{s_{yy}^{(0)}}. \tag{5.35}$$

From these equations, $b(x)$, and consequently the width of contact and the lateral spread of the wire, is shown to depend on the initial diameter of the wire, reduction ratio, roll radius, and friction coefficient. While the influence of roll speed and material type is negligible, it becomes apparent when hardening is incorporated into the analysis. By solving equations (5.35) together with (5.30), $b(x)$ and $p^{(0)}$ are solved. However, in equation (5.30) the dependency on $b(x)$ can be removed to simplify further. An alternative ODE for $b(x)$ may be found by replacing $u^{(0)}$ from (5.31) and $\lambda^{(0)}$ from (5.34) into (5.14), as

$$b\frac{\mathrm{d}h}{\mathrm{d}x} + h\frac{\mathrm{d}b}{\mathrm{d}x} = -h\frac{\mathrm{d}b}{\mathrm{d}x}\frac{s_{xx}^{(0)}}{p^{(0)}}. \tag{5.36}$$

By replacing expression (5.36) into (5.30) and further simplifying the resultant using (5.35) we get

$$\frac{\mathrm{d}\sigma_{xx}^{(0)}}{\mathrm{d}x} - \left(\frac{\mathrm{d}h/\mathrm{d}x}{h}\frac{s_{xx}^{(0)}}{s_{yy}^{(0)}}\right)\sigma_{xx}^{(0)} + \frac{1}{h}\left(-\frac{\mathrm{d}h}{\mathrm{d}x} \mp \beta\right)\sigma_{yy}^{(0)} = 0, \tag{5.37}$$

which is an ODE for the stresses without depending on the width. Expression (5.37) can be written in terms of $p^{(0)}$ by replacing stress components from (5.27) and (5.20), and solved with boundary conditions (5.23)

$$4\sigma_{xx}^{(0)}(x=0) = F_{\text{in}} \qquad \text{and} \qquad 4bh\sigma_{xx}^{(0)}\Big|_{x=1} = F_{\text{out}}. \tag{5.38}$$

From (5.38), if there is no exit tension, then $\sigma_{xx}^{(0)}$ becomes zero at the exit. Otherwise, the value of $\sigma_{xx}^{(0)}$ at the exit depends on the final width. In such cases, b at the exit must be estimated and iteratively refined to align with the width determined from (5.35) or (5.36).

5.4 Results and discussion

5.4.1 Roll pressure

$p^{(0)}$ is solved by integrating equation (5.37) forward from the entrance with −ve sign of the coefficient of the friction, and backwards from the exit with + sign, using the Matlab ODE solver `ode45` MathWorks Inc. (2024), resulting in a pressure hill profile. The roll pressure $\sigma_{yy}^{(0)}$ is then found from (5.27) and plotted with respect to the contact angle, ϕ in Figure 5.4 for different reduction ratios. Results are compared with FE simulations from Vallellano et al. (2008), the slab model from Kazeminezhad and Taheri (2006) and the slab model for rolling of thin sheet in Chapter 2 (plane strain). The results for plane stress and plane strain are calculated from case **(*i*)** where the stresses are measured from point A in Figure 5.3(**i**). The wire is 5 mm in diameter, the roll is 75 mm in radius, and the forward/backward tensions are zero. The yield stress, $\hat{\kappa}$, is assumed to be constant and equal to $385/\sqrt{3}$ MPa the same as the average value in FE simulations. The Tresca friction law, $\hat{\tau} = m\hat{\kappa}$ with the coefficient of $m = 0.25$ is used to generate FE results in (Vallellano et al., 2008). Generally, the relationship $\mu < m/\sqrt{3}$ is used essentially for a simple elastoplastic model (Zhang and Ou, 2016), where the upper limit is used to transfer m into the Coulomb friction coefficient, μ, for generating the analytical results presented in Figure 5.4.

FE results for all reductions can be seen to have two distinct regions; a massive rise between the entrance and point A and a shallow rise from point A to the exit. This trend can be explained better when looking alongside Figure 5.5 which schematically shows how the wire looks as seen from the side and above while rolling. The wire enters between rolls from the right-hand side with a circular cross-section and exits from the left with an almost rectangle cross-section, therefore, the contact surface forms rather like half of an ellipse. As explained by Carlsson (Carlsson, 1998) when the material starts to deform, surrounding parts of the wire are still in the elastic range and will therefore resist deformation. The situation may be compared to that of an indentation. As a result, a normal pressure will build up, resulting in a sharp rise in contact pressure soon after the entrance. As deformation continues, larger parts of the wire deform and the resistance from the elastic parts decreases, allowing the material to flow laterally which in turn results in a pressure drop until point A. At this point, an ordinary friction hill starts to form with a pressure pick between this point and the roll exit (Carlsson, 1998).

From the results, it can be seen that the current model correctly predicts the location of point A by assuming that the area of the cross-section at this point is the same as that of the wire before rolling. Both the current plane-stress model and Kazeminezhad and Taheri (2006) correctly predict the roll pressure at point A, for larger reductions. From point A to the roll exit, the FE results lie between the plane-strain and plane-stress predictions, reflecting the presence of 3D material flow within the roll gap. Consequently, the results presented by Kazeminezhad and Taheri (2006) show better agreement with the FE data. Another notable difference between the FE results and the perfect plastic models in Figure 5.4 is that the roll pressure starts at zero at the entrance and returns to zero at the exit. This behaviour arises from the inclusion of elasticity in the FE simulations, which is absent in the perfect plastic models.

5.4.2 Lateral spread

After solving for stresses, $b(x)$ and consequently the lateral spread, is determined by integrating either equation (5.35) or (5.36) from the entrance to the exit. The integration is performed using the MATLAB ODE solver `ode45` MathWorks Inc. (2024), with the initial condition $b(x = 0) = 1$, which is consistent with the chosen non-dimensionalisation. Depending on the assumptions made in cases $(\boldsymbol{i})$ and $(\boldsymbol{ii})$, illustrated in Figure 5.3, the lateral spread varies. In case $(\boldsymbol{i})$, the volume of the hypothetical shape is considered to

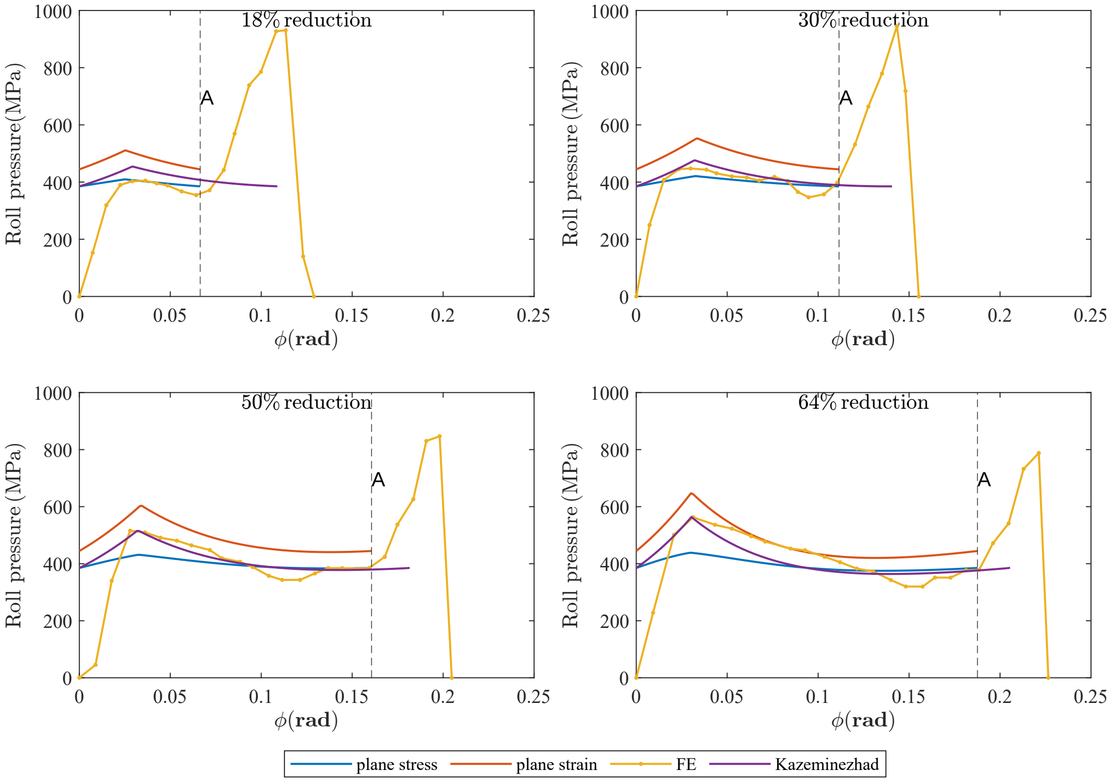

Figure 5.4: σ_{yy} on the surface for the wire with 5 mm diameter and the rolls with 75 mm radius and different reduction ratios, plotted against the contact angle, ϕ.

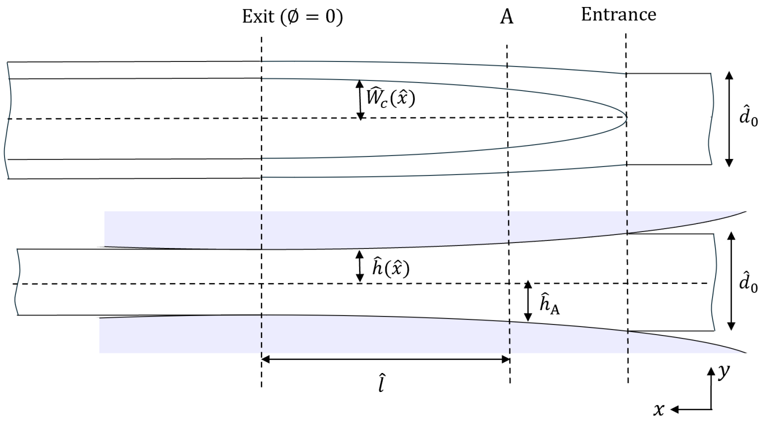

Figure 5.5: A diagram of the deforming wire, seen from above (top figure) and from side (bottom figure). The wire/roll contact surface forms rather like half of an ellipse. Adapted from Carlsson (1998)

be equal to that of the actual wire in the roll gap. As a result, the lateral spread is determined by equating the cross-sectional area of the real shape to that of the rectangle. We therefore write

$$2\hat{W}_c\hat{h} + \pi\hat{h}^2 = 4\hat{b}\hat{h} \qquad \Rightarrow \qquad \hat{W}_c = 2\hat{b} - \frac{\pi\hat{h}}{2}, \tag{5.39}$$

where $\hat{W}_c$ is the width in contact with the roll, while the bulged edges are assumed to form a half-circle. With this, the lateral spread, $\hat{W}_t$, is found as

$$\hat{W}_t = \hat{W}_c + 2\hat{h}. \tag{5.40}$$

In case ***(ii)***, it is assumed that the predicted cross-section is always circumscribed about the real cross-section (see Figure 5.3***(ii)***). In other words, $\hat{W}_t = 2\hat{b}$. The lateral spread prediction, $\hat{W}_t$, for both cases, is plotted in Figure 5.6 for various diameters and reduction ratios with 50 mm roll radius. The results are compared with experimental data (Erfanian et al., 2025b), Kobayashi's empirical equation (5.5), and equation (5.4) from Kazeminezhad and Taheri (2005). The latter equation is particularly relevant because the wire used in the experiments is stainless steel, which aligns with the materials to which equation (5.4) applies. The experiments were conducted in the WMG labs at the University of Warwick using the existing rolling machine. Stainless steel and brass wires were tested at different diameters and reduction ratios. For brass wires, reductions greater than 30% could not be achieved due to the onset of alligatoring fracture; therefore, only the data from stainless steel wires are reported here.

In the current model, predictions depend on the friction coefficient, which is challenging to determine experimentally. The experimental data were obtained under non-lubricated test conditions, and a friction coefficient of $\mu = 0.25$ has been shown to provide the best agreement with experimental data. Consequently, this value is used for results in Figure 5.6. The case ***(i)*** performs closely to experimental data across all diameters and reduction ratios while the case ***(ii)*** consistently overpredicts the lateral spread. Kazeminezhad Equation (5.4) depends only on the reduction ratio. While it performs well for smaller reduction ratios, it deviates for larger values, with the deviation appearing to depend on wire diameter (e.g., underestimates for $\hat{d}_0 = 5.96$ mm and overestimates for $\hat{d}_0 = 7.96$ mm). Kobayashi's equation underestimates the lateral spread across all wire diameters. The deviation is significant, particularly at higher reduction ratios, and it is the least reliable for predicting this set of experimental data.

Some studies suggest that the friction coefficient has a negligible effect on the lateral spread (Carlsson, 1998; Kazeminezhad et al., 2008). This observation is attributed to the movement of lubricant toward the sides of the roll, driven by the extremely high contact pressure at the entry point. Similarly, the empirical equations proposed by Kazeminezhad and Kobayashi exhibit no dependence on friction. To examine the impact

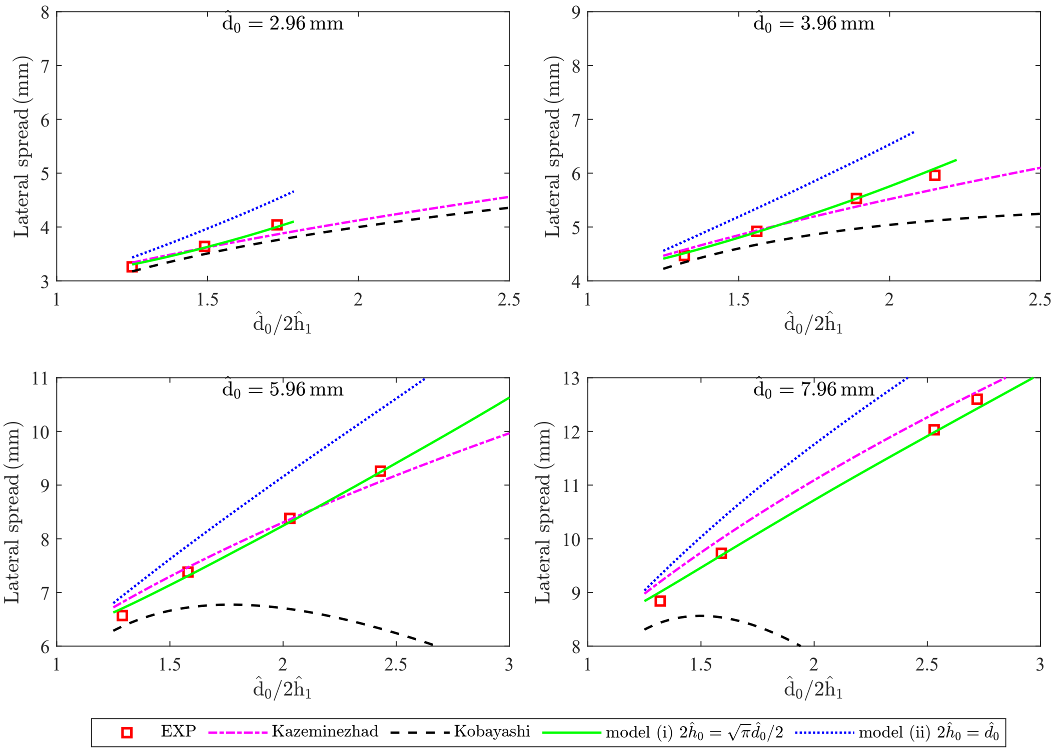

Figure 5.6: Lateral spread for wires with different diameters, d_0, and reduction ratios, $d_0/(2h_1)$

of friction, the ratio of lateral spread to the initial wire diameter is plotted in Figure 5.7 for two different friction coefficients. In the absence of experimental data under the lubricated condition, the FE results from Vallellano et al. (2008) are utilised. Specifically, the data represented by the black line with circles correspond to the experimental measurements for $d_0 = 5.96$ mm with $\mu = 0.25$, while the counterpart for $d_0 = 5$ mm is derived from FE simulations using $m = 0.25$ (approximated with $\mu = 0.14$). To minimise the influence of different wire diameters in this comparison, wires with relatively similar diameters were selected, and the results were scaled by the initial diameter.

The comparison in Figure 5.7 shows that larger friction extends the lateral

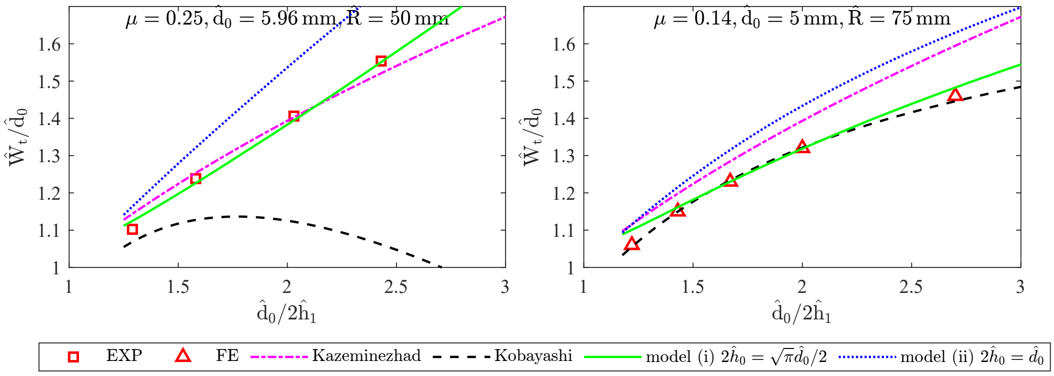

Figure 5.7: Effect of friction coefficient on lateral spread

spread, possibly due to the enhanced constraint in the longitudinal direction. This effect is accurately captured by model $(\boldsymbol{i})$, and becomes more significant at larger reductions. Kazeminezhad's equation correctly predicts lateral spread for high friction coefficients but tends to overestimate the results for lower friction values. Conversely, Kobayashi's equation demonstrates better agreement under low-friction conditions compared to high friction, although different roll and wire diameters might also influence this.

While additional experimental data is required to draw more robust conclusions, the current dataset presented in Figures 5.6 and 5.7 shows that the mathematical model in case $(\boldsymbol{i})$ successfully predicts lateral spread across a range of wire diameters, reduction ratios, and both low and high friction coefficients. Importantly, this model achieves accurate predictions without requiring fitting parameters or assuming additional factors.

5.5 Conclusion

A mathematical model for wire rolling is presented. The needed equations in all directions are written for perfect rigid plastic material and simplified with the assumption of a small rate of change of both thickness and width with respect to the length. This assumption simplifies a general state of deformation to the plane-stress deformation. Results for roll pressure and width are provided and compared to FE or experimental data. The model predicts the correct order of magnitude for roll pressure distribution in the rolling direction, however, FE results remain between the results from plane-stress and plane-strain deformation and are better matched with results from Kazeminezhad's slab model. Despite this limitation, the mathematical model in case $(\boldsymbol{i})$ accurately predicts lateral spread for various wire diameters, reduction ratios, and friction coefficients without relying on fitting parameters or additional assumptions. A possible explanation for this lies in the importance of the stress ratio, s_{zz}/s_{yy}, rather than the absolute stress values, in predicting the lateral spread.

However, there remains considerable scope for improvement. Relaxing the assumption of a small rate of change in width would allow the problem to be modelled under a general stress state. This would also enable more detailed modelling of pressure distribution across the lateral direction and account for the curvature of the edges.

Another challenge is in terms of the material. Cold-rolled wire, often exhibits a strong texture in the axial direction, while the texture in the cross-section can be quite different (Carlsson, 1998). Such anisotropy introduces challenges that must be addressed. Regarding the split observed during the rolling of brass wire, it is worth investigating whether this issue arises from a manufacturing defect or if there exists a fundamental limit to the rolling process for wires.

Chapter 6

Conclusion and further work

This thesis advances the understanding of the complex behaviour of symmetric rolling. This includes:

- a systematic analysis and review of simple models for cold rolling which demonstrates their deficiencies in capturing the complex stress and strain behaviour in rolling (Chapter 2);
- a new asymptotic model, which illustrates a robust method with a simple material model for constructing thin-sheet rolling models appropriate for FE validation and real-time prediction and control (Chapter 3);
- a more realistic material model, which predicts an inhomogeneous hardening effect through the thickness (Chapter 4);
- and a new framework for modelling flat rolling of wire, which is shown to be more reliable than other phenomenological models in the literature (Chapter 5).

In retrospect, the asymptotic models of the sheet rolling process, presented in Chapters 2 and 3, successfully predict the through-thickness stress and strain oscillations. While the leading-order solution recreates the conventional pressure hill from slab analysis, the work is distinguished by the use of multiple scales resulting in a different $O(\delta)$ correction. To date, the asymptotic solution and FE simulations presented in this work demonstrate the highest degree of agreement the author is aware of in the literature while is more than $16,000$ times faster compared to FE simulation. Furthermore, the modelling and validation process in Chapter 4 reveals that the hardening effect only emerges at the leading-order solutions. As a result, the first-order corrections remain largely unaffected and are applicable to both hardening and non-hardening materials. Consequently, while the inclusion of hardening makes the model more realistic and reveals the inhomogenous hardening through-thickness, its impact on the solution is minimal under the current conditions, namely, small reduction and long roll gap, which are sensible choices for real cold rolling processes. This outcome is not immediately evident prior to the analysis and could only be realised through mathematical modelling and comparison with FE data.

It is important to note that, while careful FE simulations from Flanagan et al. (2024) are used to validate the model, the model itself also serves to assess the reliability of simulations. This underscores the importance of mathematical models as a tool for validating simulations. In particular, while the stress and strain oscillatory distribution is a direct consequence of equations, commonly used mesh densities for rolling are found to be inadequate to capture them in the roll gap, and significantly higher mesh densities are needed. Moreover, achieving convergence to a steady state and avoiding numerical oscillations, which are common in time-stepping FE simulations, is challenging and can significantly impact the results if not properly managed. In contrast, the current mathematical models are formulated specifically for the steady state, making them reliable tools for validation purposes.

The mathematical model for wire rolling introduced in Chapter 5 provides accurate predictions of lateral spread across different wire diameters, reduction ratios, and friction coefficients, all without the need for fitting parameters. This approach proves to be more reliable than existing phenomenological models in the literature and serves as a robust tool for validating FE results or guiding process design. Also, another example that highlights the necessity for meticulous execution of FE simulations is a set of FE results provided by a collaborator for wire rolling (not included in this thesis). Although the data appeared credible, it showed weaker agreement with the mathematical model than the agreement observed between the model and experimental results. This suggests that the seemingly reliable FE results were, in fact, inaccurate.

All these studies prioritise developing models that capture the essential mechanisms of the rolling process. To achieve this, several factors complicating the dynamics have been intentionally neglected. Yet, the systematic nature of these studies means alternative boundary conditions and material models can be incorporated into the formulation. The following sections outline those used in the current studies and the biases caused, aiming to guide future research in overcoming the identified challenges. This progression could pave the way for utilising analytical models in control systems, fostering a new era of bespoke, energy-efficient, and high-quality manufacturing.

6.1 Sheet rolling

The model and FE results assume plain strain, as otherwise, the numerical cost of 3D FE simulations would have been intractable. The assumption of plane strain is common and experimentally verified away from the edges of wide sheets, although it would break down near the sheet edges. To accurately predict edge phenomena such as bulging or wrinkling in these regions, therefore, the problem must be analysed under a general 3D stress state. Similarly, non-rigid rolls (for example elastically deforming rolls) would add computational expense to the FE model; the assumption of rigid rolls is commonly regarded as valid for all but very thin foil rolling, where the flattening of the rolls limits the thinness of the sheet and requires a separate analysis. In the mathematical model here, the roll shape ($h(z)$) is arbitrary and could be adapted to include roll flattening using analytical equations, such as Hitchcock's formula, when an appropriate contact condition in the flat segment is applied to model foil rolling.

Although the perfectly plastic material model provides reasonable agreement with FE results without this assumption, the absence of hardening is often considered detrimental to the model's realism. Incorporating hardening is, therefore, a logical step to address this criticism and enhance the model's practical relevance. This research highlights the mathematical challenges associated with incorporating hardening into the model. The process revealed inconsistencies in the mathematical framework, necessitating certain approximations to achieve a solution. While these approximations align well with FE results in a range valid for cold rolling (relatively small reduction and large aspect ratio), focusing on developing a mathematically consistent approach to model hardening could be a valuable direction for future work.

The von Mises function is used to describe the yielding condition. Alternatively, this could be replaced with an anisotropic yield criterion (e.g., Hill's 1948 yield criterion) with known anisotropy coefficients. In such a case, the solution structure would largely remain unchanged, except for the incorporation of weighted stresses. However, this scenario is of limited scientific significance because it is the rolling process itself which induces anisotropy. To accurately capture the anisotropy effect, it would be necessary for the anisotropy to evolve throughout the process. This would require a model describing how deformation induces anisotropy within the material, thereby adding an additional layer of complexity to the modelling process. It is interesting to note in passing that exactly the same mathematical results are derived if the Tresca yield criterion is imposed instead of the von Mises yield criterion, provided the yield stress for the Tresca criterion is taken to be $\hat{\sigma}_Y = 2\hat{\kappa}$. This is a consequence of the assumption of plane strain and the associated form taken by the stress tensor that results in the von Mises and Tresca criteria becoming identical in this case.

Similarly, while elasticity plays a significant role both before and beyond the roll gap, particularly at the boundaries near the entrance and exit, the good agreement between the elasto-plastic FE and the rigid-plastic mathematical model demonstrates that the large pressures within the roll gap mean the behaviour is plastically-dominated within the roll gap, and the justification of neglecting elasticity is valid. Integrating elasto-plastic behaviour remains a challenging task, although without including elasticity, the models are unable to predict entrance and exit region behaviours and residual stress.

The systematic assumptions of a large aspect ratio, $\hat{\ell}/\hat{h} = 1/\delta$, and a small friction coefficient, μ, which are common in practice, facilitate the asymptotic solution. For small aspect ratios, the solution remains valid for a sheet with a length equal to its thickness. However, this requires a small reduction to satisfy the assumption of $\mathrm{d}h/\mathrm{d}x$ being $O(\delta)$. The challenge in the small aspect ratio range, though, is that the entrance and exit regions constitute a significant portion of the overall length, making it less accurate to neglect elasticity. Employing large friction might result in the shear stress being of the same order as the normal stresses. Therefore, a different solution could be expected compared to the current prediction. The Coulomb law is used as the surface boundary condition, where the surface is assumed to slip along the roll throughout the roll gap unless a single point, which is the neutral point. However, this assumption cannot always be justified and the FE results show a region of sticking around the predicted neutral point. Including a sticking friction model near the neutral point would smooth the shock seen in the mathematical model but not the FE simulations. To account for a sticking region of length $O(\delta)$, the boundary condition in the inner region (Section 3.2.1.3) needs to be adjusted, potentially by constraining the velocity instead of the force.

The final set of assumptions relates to the boundary condition at the entrance. Based on the assumption of rigid material outside the roll gap, if the sheet is to enter rigidly, the velocity profile must be uniform. However, unlike velocity, the assumption of rigid material outside the roll gap is insufficient to determine the force distribution at the entrance. Therefore, an assumed force distribution is proposed, which appears to be reasonable based on comparisons with FE simulations. While homogeneous velocity and linear shear assumptions do not apply to all practical working conditions, they agree with the FE simulations of symmetric single-pass rolling, which do not rely on these assumptions. If the rolling process were asymmetric, or if previous rolling passes were to be considered, different assumptions about the entrance condition of the material may be needed, which would be an interesting direction for future research.

Additional phenomena can be identified to tailor the model to specific applications. This could include relaxing the assumption of symmetry to enable the prediction of asymmetric rolling (extending Minton et al., 2016), and including temperature and recrystallisation effects in order to model hot rolling processes. Including heating and heat flux in the model might allow the prediction of similar oscillatory patterns observed in the heat flux during rolling (Olaogun et al., 2019). Of course, all of these modifications would further complicate the model, making it harder to understand and interpret the fundamental mechanics; therefore, the present model represents a good balance between complexity and understandability, retaining most of the underlying simplicity of slab methods and introducing the wave-like behaviour needed for reasonable comparison with FE simulations.

6.2 Flat rolling of wire

In addition to the challenges related to the material model discussed in the previous section, which are also relevant to wire rolling, the specific assumptions made here introduce unique challenges.

Validation of the results for lateral spread was carried out using a relatively high friction coefficient, dictated by the constraints of the available experimental setup. This raises questions about the validity of certain assumptions in the model, specifically the small friction coefficient and shear stress. Furthermore, a comparison of roll pressure predictions with FE results reveals that the actual pressure distribution does not fully conform to the plane-stress assumption.

Despite these limitations, the model demonstrates great agreement with experimental results in predicting lateral spread. A possible explanation for this lies in the importance of the stress ratio, s_{zz}/s_{yy}, rather than the absolute stress values, in predicting the lateral spread. While the model may underestimate individual stresses, it appears to capture the correct ratio, leading to accurate predictions. This observation requires further investigation to better understand the underlying mechanisms.

Incorporating the first-order correction and multiple scales into the model would be significantly more complex and would need to build upon the leading-order solution, which provides an average representation of pressure. It is anticipated that all normal stress components contribute to such a model. Relaxing the assumption of a small rate of change in width would allow the problem to be modelled under a general stress state. To achieve this, and also to account for the barreling of the edges, the width can be expressed as $b(x, y) = b^{(0)}(x) + \delta b^{(1)}(x, y)$. By considering the lateral spread to be of the same order of magnitude as the length, the normal vector to the edges can be written as $\boldsymbol{s} = \big(-a\mathrm{d}b^{(0)}/\mathrm{d}x - a\delta\partial b^{(1)}/\partial x, -a\partial b^{(1)}/\partial y, 1\big)$, where a is $\hat{b}/\hat{\ell}$, which is $O(1)$. This formulation allows for the inclusion of $\sigma_{zz}(x, z)$ at the leading order, which also necessitates defining the friction boundary condition in both the lateral and longitudinal directions, probably based on related velocity components such as those used in Johnson (1991).

This study opens the door to numerous potential research directions; regarding the split observed during the rolling of brass wire, it is worth investigating whether this issue arises from a manufacturing defect or if there exists a fundamental limit to the rolling process for wires. Similarly, an intriguing area of study is the rolling of clad wire, where a different material is used for the core and outer cladding to optimise properties such as durability, lightness, and conductivity. Another promising research direction motivated by, but not limited to, wire rolling is the investigation of the transition between plane strain and plane stress loading conditions. This requires, first, understanding the fundamental causes of each condition. Key questions include whether, in plane strain, the primary factor retaining the width is lateral friction or the pressure resulting from material stacking towards the edges, and how these factors evolve as the loading condition shifts from the plane strain to the plane stress limit.

6.3 Relevance in industry

Controlling the magnitude and distribution of residual stress is crucial in sheet metal manufacturing. FE simulations of sheet rolling reveal a thin layer of residual stress that appears to align with the oscillatory pattern at the exit—an observation that was previously unknown. Further research could explore this phenomenon through additional FE analyses or by incorporating elasticity in the exit region. The current study has paved the way for such investigations by identifying the presence of residual stress in the first place.

Both the sheet and wire rolling studies emphasise the critical need for rigorous validation of FE simulations. This finding is particularly relevant to industry, as it highlights the risk of obtaining seemingly plausible yet inaccurate results. Further research in this area could enhance the reliability of FE practices in the industry, and it may even be advantageous for Abaqus to update its manual to include an example of accurately conducted FE rolling simulations.

Building on the current understanding of asymptotic modelling in predominantly plastic metal forming, it would be valuable to extend these techniques to other industrial metal forming processes that lack robust analytical models. Potential areas for future research include open-die forging, extrusion, ring rolling, and levelling/decoiling. These processes could benefit from similar mathematical approaches and the expertise employed in this thesis.

Appendices

Appendix A1 Solving for the second-order stresses

In this appendix, the solution is continued to this order of correction with the goal of finding the unknown parameters $A(\xi, z)$ and $D(z)$ from the previous order. It should be noted that this does not completely resolve the second-order stresses, as it will be determined only up to an unknown function $M(\xi, z)$ which would be determined at the next order, $O(\delta^3)$. However, it does give a secularity condition for the previously unknown function $A(\xi, z)$ and $D(z)$.

From the yield function (3.10a), at $O(\delta^2)$, and substituting the known variables from the previous orders, we find that

$$\sigma_{xx}^{(2)} = -p^{(2)} - \frac{1}{2}{\sigma_{xy}^{(1)}}^2 \qquad \text{and} \qquad \sigma_{yy}^{(2)} = -p^{(2)} + \frac{1}{2}{\sigma_{xy}^{(1)}}^2. \tag{A.1}$$

At $O(\delta^2)$, the local balance equations (3.10b) and (3.10c) are

$$\frac{\partial \sigma_{xx}^{(1)}}{\partial z} + \frac{1}{h}\frac{\partial \sigma_{xx}^{(2)}}{\partial n} + \frac{\partial \sigma_{xy}^{(2)}}{\partial y} = 0 \qquad \text{and} \qquad \frac{\partial \sigma_{yy}^{(2)}}{\partial y} + \frac{\partial \sigma_{xy}^{(1)}}{\partial z} + \frac{1}{h}\frac{\partial \sigma_{xy}^{(2)}}{\partial n} = 0. \tag{A.2}$$

By substituting in $\sigma_{xx}^{(2)}$ and $\sigma_{yy}^{(2)}$ from equation (A.1), and $\sigma_{xx}^{(1)}$ from (3.14), we have,

$$\frac{\partial \sigma_{xy}^{(2)}}{\partial y} - \frac{1}{h}\frac{\partial p^{(2)}}{\partial n} = \frac{\partial p^{(1)}}{\partial z} + \frac{1}{2h}\frac{\partial {\sigma_{xy}^{(1)}}^2}{\partial n} \quad \text{and} \quad \frac{\partial p^{(2)}}{\partial y} - \frac{1}{h}\frac{\partial \sigma_{xy}^{(2)}}{\partial n} = \frac{\partial \sigma_{xy}^{(1)}}{\partial z} + \frac{1}{2}\frac{\partial {\sigma_{xy}^{(1)}}^2}{\partial y}. \tag{A.3}$$

These two equations give wave equations for $p^{(2)}$ and $\sigma_{xy}^{(2)}$, forced by $p^{(1)}$ and $\sigma_{xy}^{(1)}$. By substituting $p^{(1)}$ and $\sigma_{xy}^{(1)}$ from equation (3.16) into (A.3), we arrive at

$$\begin{aligned}\frac{\partial \sigma_{xy}^{(2)}}{\partial y} - \frac{1}{h(z)}\frac{\partial p^{(2)}}{\partial n} = & \left[\frac{\partial A}{\partial z}\left(n + \frac{y}{h}\right) + \frac{\partial A}{\partial z}\left(n - \frac{y}{h}\right)\right] - \frac{dD(z)}{dz} \\ & + \frac{1}{2h}\frac{\partial}{\partial n}\left[A\left(n + \frac{y}{h}\right)^2 + A\left(n - \frac{y}{h}\right)^2 - 2A\left(n + \frac{y}{h}\right)A\left(n - \frac{y}{h}\right)\right] \\ & + \frac{y}{h}\left[A'\left(n + \frac{y}{h}\right) - A'\left(n - \frac{y}{h}\right)\right]\left(\frac{dp^{(0)}}{dz} - \frac{\mathrm{d}h/\mathrm{d}z}{h}\right),\end{aligned} \tag{A.4a}$$

$$\begin{aligned}\frac{\partial p^{(2)}}{\partial y} - \frac{1}{h}\frac{\partial \sigma_{xy}^{(2)}}{\partial n} =& \left[\frac{\partial A}{\partial z}\left(n+\frac{y}{h}\right) - \frac{\partial A}{\partial z}\left(n-\frac{y}{h}\right)\right] \\ &+ \frac{1}{2}\frac{\partial}{\partial y}\left[A\left(n+\frac{y}{h}\right)^2 + A\left(n-\frac{y}{h}\right)^2 - 2A\left(n+\frac{y}{h}\right)A\left(n-\frac{y}{h}\right)\right] \\ &+ \frac{y}{h}\left[A'\left(n+\frac{y}{h}\right) + A'\left(n-\frac{y}{h}\right)\right]\left(\frac{dp^{(0)}}{dz} - \frac{\mathrm{d}h/\mathrm{d}z}{h}\right) \\ &+ y\left(\left(\frac{dp^{(0)}}{dz}\right)^2 + \frac{\partial^2 p^{(0)}}{\partial z^2}\right) + \frac{dp^{(0)}}{dz}\left[A\left(n+\frac{y}{h}\right) - A\left(n-\frac{y}{h}\right)\right],\end{aligned} \tag{A.4b}$$

where prime denoting $\partial/\partial\xi$, and $A(n \pm (y/h), z)$ is abbreviated to $A(n \pm (y/h))$ for brevity while the dependence on z is still acknowledged. We solve this as a system of two coupled equations by finding particular integrals for each of the forcing terms of the right-hand-side. Ultimately, we find the solution for $\sigma_{xy}^{(2)}$ and $p^{(2)}$ as

$$\begin{aligned}\sigma_{xy}^{(2)} =& M\Big(n+\frac{y}{h}\Big) - M\Big(n-\frac{y}{h}\Big) + y\left[\frac{\partial A}{\partial z}\Big(n+\frac{y}{h}\Big) + \frac{\partial A}{\partial z}\Big(n-\frac{y}{h}\Big)\right] \\ &+ \frac{y^2}{2h}\Big(\frac{dp^{(0)}}{dz} - \frac{\mathrm{d}h/\mathrm{d}z}{h}\Big)\Big[A'\Big(n+\frac{y}{h}\Big) - A'\Big(n-\frac{y}{h}\Big)\Big] + \frac{y}{2}\frac{dp^{(0)}}{dz}\Big[A\Big(n+\frac{y}{h}\Big) + A\Big(n-\frac{y}{h}\Big)\Big] \\ &+ \frac{1}{2}\Big[A'\Big(n+\frac{y}{h}\Big)A^{\wedge}\Big(n-\frac{y}{h}\Big) - A^{\wedge}\Big(n+\frac{y}{h}\Big)A'\Big(n-\frac{y}{h}\Big)\Big] \\ &+ \frac{y}{2h}\frac{\partial}{\partial n}\Big[A\Big(n+\frac{y}{h}\Big)^2 + A\Big(n-\frac{y}{h}\Big)^2\Big] - y\frac{dD(z)}{dz},\end{aligned} \tag{A.5a}$$

$$\begin{aligned}p^{(2)} =& M\Big(n+\frac{y}{h}\Big) + M\Big(n-\frac{y}{h}\Big) + y\left[\frac{\partial A}{\partial z}\Big(n+\frac{y}{h}\Big) - \frac{\partial A}{\partial z}\Big(n-\frac{y}{h}\Big)\right] \\ &+ \frac{y^2}{2h}\Big(\frac{dp^{(0)}}{dz} - \frac{\mathrm{d}h/\mathrm{d}z}{h}\Big)\Big[A'\Big(n+\frac{y}{h}\Big) + A'\Big(n-\frac{y}{h}\Big)\Big] \\ &+ \frac{y}{2}\frac{dp^{(0)}}{dz}\Big[A\Big(n+\frac{y}{h}\Big) - A\Big(n-\frac{y}{h}\Big)\Big] + \frac{h}{2}\frac{dp^{(0)}}{dz}\Big[A^{\wedge}(n+\frac{y}{h}) + A^{\wedge}(n-\frac{y}{h})\Big] \\ &+ \frac{1}{2}\Big[A'\Big(n+\frac{y}{h}\Big)A^{\wedge}\Big(n-\frac{y}{h}\Big) + A^{\wedge}\Big(n+\frac{y}{h}\Big)A'\Big(n-\frac{y}{h}\Big)\Big] \\ &+ \frac{y}{2h}\frac{\partial}{\partial n}\Big[A\Big(n+\frac{y}{h}\Big)^2 - A\Big(n-\frac{y}{h}\Big)^2\Big] + \frac{y^2}{2}\left(\frac{d^2p^{(0)}(z)}{dz^2} + \left(\frac{dp^{(0)}(z)}{dz}\right)^2\right),\end{aligned} \tag{A.5b}$$

where the term $M\left(n+(y/h)\right) - M\left(n-(y/h)\right)$ represents the complementary solution, which is an as-yet-unknown wave, and $A^{\wedge}$ is the integral of A such that $A^{\wedge\prime} = A$.

Substituting this solution into the friction equation at this order, $\sigma_{xy}^{(2)} \mp \beta p^{(1)} = 0$, results in

$$
\begin{aligned}
&M(n+1,z) - M(n-1,z) + h\left[\frac{\partial A(n+1,z)}{\partial z} + \frac{\partial A(n-1,z)}{\partial z}\right] \\
&\quad + \frac{h}{2}\Big(\frac{dp^{(0)}}{dz} - \frac{1}{z}\frac{\mathrm{d}h}{\mathrm{d}z}\Big)\big[A'(n+1,z) - A'(n-1,z)\big] + \frac{h}{2}\frac{dp^{(0)}}{dz}\big[A(n+1,z) + A(n-1,z)\big] \\
&\quad + \frac{1}{2}\big[A'(n+1,z)A^{\wedge}(n-1,z) - A'(n-1,z)A^{\wedge}(n+1,z)\big] \\
&\quad + \frac{1}{2}\frac{\partial}{\partial n}\left[A(n+1,z)^2 + A(n-1,z)^2\right] - h\frac{\partial D(z)}{\partial z} \\
&\qquad\qquad\qquad \mp \beta\big[A(n+1,z) + A(n-1,z) + D(z)\big] = 0.
\end{aligned}
\tag{A.6}
$$

This equation can be significantly simplified by using the condition (3.19), to give

$$
\begin{aligned}
&2h\frac{\partial A(n+1,z)}{\partial z} + \frac{\partial}{\partial n}\left(A(n+1,z)^2\right) + \left(h\frac{dp^{(0)}}{dz} \mp 2\beta\right)A(n+1,z) \\
&\qquad\qquad - h\frac{dD(z)}{dz} \mp \beta D(z) = -[M(n+1,z) - M(n-1,z)],
\end{aligned}
\tag{A.7}
$$

where $M(\xi, z)$ is the second-order wave-equation homogeneous solution to (A.5) analogous to the first-order wave-equation solution $A(\xi, z)$. We do not need to calculate M, as by the same secularity argument used for $A(\xi, z)$ at first order, to avoid $M(\xi, z)$ growing as a function of n giving the secularity condition $M(n+1, z) = M(n-1, z)$. Therefore, the right-hand side of equation (A.7) is zero. The resulting equation is quoted in (3.25).

Appendix A2 Rearranging the second-order stresses to get Burger's equation

In this appendix, equation (3.25) is rearranged into the form of the standard Burger's equation. By replacing the factor $h\,\mathrm{d}p^{(0)}/\mathrm{d}z$ in (3.25) with its equivalent from (3.21), it gives

$$
\frac{\partial A(\xi,z)}{\partial z} + \frac{1}{2h}\frac{\partial}{\partial \xi}\left(A(\xi,z)^2\right) - \left(\mp\frac{\beta}{2h}(p^{(0)} - 1) - \frac{\mathrm{d}h/\mathrm{d}z}{h}\right)A(\xi,z) = 0. \tag{A.8}
$$

We now aim to combine the first and third terms of (A.8) into a single z-derivative. To this end, we first rewrite the factor multiplying $A(\xi, z)$ as a z-derivative by defining,

$$
\alpha_1(z) = \exp\left\{\int_0^z \Big(\mp\frac{\beta}{2h(\tilde{z})}(p^{(0)}(\tilde{z}) - 1)\Big)d\tilde{z}\right\}. \tag{A.9}
$$

Differentiating $\log(\alpha_1/h)$ with respect to z then shows that

$$
\Big(\mp\frac{\beta}{2h}(p^{(0)} - 1) - \frac{\mathrm{d}h/\mathrm{d}z}{h}\Big) = \frac{\frac{\partial}{\partial z}(\alpha_1/h)}{(\alpha_1/h)}. \tag{A.10}
$$

Replacing (A.10) into the original equation (A.8), this equation can be rewritten as

$$\frac{\partial A(\xi)}{\partial z} - \frac{\frac{\partial}{\partial z}(\alpha_1/h)}{(\alpha_1/h)} A(\xi) + \frac{1}{2h}\frac{\partial}{\partial \xi}\left(A(\xi)^2\right) = 0. \tag{A.11}$$

By dividing (A.11) by α_1/h, the first two terms give a z derivative of $\frac{A(\xi)}{(\alpha_1/h)}$. Thus,

$$\frac{\partial}{\partial z}\left(\frac{A(\xi)}{(\alpha_1/h)}\right) + \frac{\alpha_1}{2h^2}\frac{\partial}{\partial \xi}\left(\left(\frac{A(\xi)}{(\alpha_1/h)}\right)^2\right) = 0. \tag{A.12}$$

Finally, with the following change of variable, Burger's equation is obtained,

$$T = \int^z \frac{\alpha_1}{h(\bar{z})^2}\, \mathrm{d}\bar{z} \quad \text{and} \quad \omega\big(\xi, T(z)\big) = \frac{A(\xi, z)}{(\alpha_1/h)} \quad \Rightarrow \quad \frac{\partial}{\partial T}(\omega) + \frac{1}{2}\frac{\partial}{\partial \xi}\left(\omega^2\right) = 0. \tag{A.13}$$

This is the equation as quoted in (3.28b).

Appendix A3 Solving for the second-order velocities

In this appendix, the solution is continued to this order of correction with the goal of finding the unknown parameters $B(\xi, z)$ from the previous order. This does not completely resolve the second-order velocity, as it will be determined only up to an unknown function $N(\xi, z)$ which would be determined at the next order, $O(\delta^3)$. However, as for the second-order stresses, it does give a secularity condition for the previously unknown function $B(\xi, z)$ which occurs in $v^{(1)}$, allowing to determine $v^{(1)}$ completely.

We begin with equation (3.50), given by

$$\frac{\partial v^{(2)}}{\partial y} + \frac{1}{h}\frac{\partial u^{(2)}}{\partial n} = -\frac{\partial u^{(1)}}{\partial z}, \qquad \frac{\partial u^{(2)}}{\partial y} + \frac{1}{h}\frac{\partial v^{(2)}}{\partial n} = -\frac{\partial v^{(1)}}{\partial z} + 2\lambda^{(1)}\sigma_{xy}^{(1)}. \tag{A.14}$$

Substituting the solutions obtained for $u^{(1)}$, $v^{(1)}$, $\lambda^{(1)}$, and $\sigma_{xy}^{(1)}$ from equation (3.45), (3.47), and (3.16) into (A.14) yields

$$\begin{aligned}\frac{\partial u^{(2)}}{\partial y} + \frac{1}{h}\frac{\partial v^{(2)}}{\partial n} = {} & \left[\frac{\partial B}{\partial z}\left(n + \frac{y}{h}\right) - \frac{\partial B}{\partial z}\left(n - \frac{y}{h}\right)\right] - 2\frac{\mathrm{d}h/\mathrm{d}z}{h^2}\left[A\left(n + \frac{y}{h}\right) - A\left(n - \frac{y}{h}\right)\right] \\ & + y\left(\frac{2}{h}\frac{\mathrm{d}p^{(0)}}{\mathrm{d}z} - \frac{\mathrm{d}h/\mathrm{d}z}{h^2}\right)\left[B'\left(n + \frac{y}{h}\right) + B'\left(n - \frac{y}{h}\right)\right] \\ & + \frac{2}{h}\left[A\left(n + \frac{y}{h}\right) - A\left(n - \frac{y}{h}\right)\right]\left[B'\left(n + \frac{y}{h}\right) + B'\left(n - \frac{y}{h}\right)\right] \\ & - y\left(\frac{h(\mathrm{d}^2h/\mathrm{d}z^2) - 2(\mathrm{d}h/\mathrm{d}z)^2}{h^3} + 2\frac{\mathrm{d}h/\mathrm{d}z}{h^2}\frac{\mathrm{d}p^{(0)}}{\mathrm{d}z}\right),\end{aligned} \tag{A.15a}$$

$$\frac{\partial v^{(2)}}{\partial y}+\frac{1}{h}\frac{\partial u^{(2)}}{\partial n}=-\left[\frac{\partial B}{\partial z}\Big(n+\frac{y}{h}\Big)+\frac{\partial B}{\partial z}\Big(n-\frac{y}{h}\Big)\right]+y\frac{\mathrm{d}h/\mathrm{d}z}{h^2}\left[B'\Big(n+\frac{y}{h}\Big)-B'\Big(n-\frac{y}{h}\Big)\right], \tag{A.15b}$$

where $A(\xi,z)$ is abbreviated to $A(\xi)$ for brevity, and similarly for $B(\xi)$. These equations form a coupled wave equation for $u^{(2)}$ and $v^{(2)}$, forced by $A(\xi)$ and $B(\xi)$. Solving them as a system of coupled equations, by finding particular integrals for each of the forcing terms on the right-hand side, ultimately, results in

$$\begin{aligned}
v^{(2)}=&-\left[N\Big(n+\frac{y}{h}\Big)-N\Big(n-\frac{y}{h}\Big)\right]-y\left[\frac{\partial B}{\partial z}\Big(n+\frac{y}{h}\Big)+\frac{\partial B}{\partial z}\Big(n-\frac{y}{h}\Big)\right]\\
&+\frac{\mathrm{d}h/\mathrm{d}z}{h^2}y\left[A\Big(n+\frac{y}{h}\Big)+A\Big(n-\frac{y}{h}\Big)\right]+y\frac{1}{2}\frac{\mathrm{d}p^{(0)}}{\mathrm{d}z}\left[B\Big(n+\frac{y}{h}\Big)+B\Big(n-\frac{y}{h}\Big)\right]\\
&+\frac{1}{2}y^2\left(\frac{1}{h}\frac{\mathrm{d}p^{(0)}}{\mathrm{d}z}-\frac{\mathrm{d}h/\mathrm{d}z}{h^2}\right)\left[-B'\Big(n+\frac{y}{h}\Big)+B'\Big(n-\frac{y}{h}\Big)\right]\\
&-\frac{y}{h}\left[B'\Big(n+\frac{y}{h}\Big)A\Big(n+\frac{y}{h}\Big)+B'\Big(n-\frac{y}{h}\Big)A\Big(n-\frac{y}{h}\Big)\right]\\
&-\frac{1}{2}\left[B\Big(n+\frac{y}{h}\Big)A\Big(n-\frac{y}{h}\Big)+B'\Big(n+\frac{y}{h}\Big)A^{\wedge}\Big(n-\frac{y}{h}\Big)\right]\\
&+\frac{1}{2}\left[B\Big(n-\frac{y}{h}\Big)A\Big(n+\frac{y}{h}\Big)+B'\Big(n-\frac{y}{h}\Big)A^{\wedge}\Big(n+\frac{y}{h}\Big)\right],
\end{aligned} \tag{A.16a}$$

$$\begin{aligned}
u^{(2)}=&\left[N\Big(n+\frac{y}{h}\Big)+N\Big(n-\frac{y}{h}\Big)\right]+y\left[\frac{\partial B}{\partial z}\Big(n+\frac{y}{h}\Big)-\frac{\partial B}{\partial z}\Big(n-\frac{y}{h}\Big)\right]\\
&-\frac{\mathrm{d}h/\mathrm{d}z}{h^2}y\left[A\Big(n+\frac{y}{h}\Big)-A\Big(n-\frac{y}{h}\Big)\right]+y\frac{1}{2}\frac{\mathrm{d}p^{(0)}}{\mathrm{d}z}\left[B\Big(n+\frac{y}{h}\Big)-B\Big(n-\frac{y}{h}\Big)\right]\\
&+\frac{1}{2}y^2\left(\frac{1}{h}\frac{dp^{(0)}}{dz}-\frac{\mathrm{d}h/\mathrm{d}z}{h^2}\right)\left[B'\Big(n+\frac{y}{h}\Big)+B'\Big(n-\frac{y}{h}\Big)\right]\\
&+\frac{y}{h}\left[B'\Big(n+\frac{y}{h}\Big)A\Big(n+\frac{y}{h}\Big)-B'\Big(n-\frac{y}{h}\Big)A\Big(n-\frac{y}{h}\Big)\right]\\
&-\frac{1}{2}\left[B\Big(n+\frac{y}{h}\Big)A\Big(n-\frac{y}{h}\Big)-B'\Big(n+\frac{y}{h}\Big)A^{\wedge}\Big(n-\frac{y}{h}\Big)\right]\\
&-\frac{1}{2}\left[B\Big(n-\frac{y}{h}\Big)A\Big(n+\frac{y}{h}\Big)-B'\Big(n-\frac{y}{h}\Big)A^{\wedge}\Big(n+\frac{y}{h}\Big)\right]\\
&-\frac{1}{2}y^2\left(\frac{h(\mathrm{d}^2h/\mathrm{d}z^2)-2(\mathrm{d}h/\mathrm{d}z)^2}{h^3}+2\frac{\mathrm{d}h/\mathrm{d}z}{h^2}\frac{dp^{(0)}}{dz}\right)\\
&-\frac{\mathrm{d}h/\mathrm{d}z}{h}\left[A^{\wedge}\Big(n+\frac{y}{h}\Big)+A^{\wedge}\Big(n-\frac{y}{h}\Big)\right]-\frac{h}{2}\frac{\mathrm{d}p^{(0)}}{\mathrm{d}z}\left[B^{\wedge}\Big(n+\frac{y}{h}\Big)+B^{\wedge}\Big(n-\frac{y}{h}\Big)\right]\\
&+\left[\left(B'\Big(n+\frac{y}{h}\Big)A\Big(n+\frac{y}{h}\Big)\right)^{\wedge}+\left(B'\Big(n-\frac{y}{h}\Big)A\Big(n-\frac{y}{h}\Big)\right)^{\wedge}\right],
\end{aligned} \tag{A.16b}$$

where the term $-\left[N\left(n+(y/h)\right)-N\left(n-(y/h)\right)\right]$ represents the complementary solution, which is an as-yet-unknown wave, and $B^{\wedge}$ is the integral of A such that $B^{\wedge\prime}=B$.

Replacing $v^{(2)}$ into the boundary condition (3.42) at the second order, $v^{(2)} = (\mathrm{d}h/\mathrm{d}z)u^{(1)}$, results in

$$\begin{aligned}\frac{dh}{dz}\Big(B(n+1)+B(n-1)\Big) &= -\Big(N(n+1)-N(n-1)\Big)+\frac{1}{h}\frac{\mathrm{d}h}{\mathrm{d}z}\Big(A(n+1)+A(n-1)\Big)\\ &- h\Big(\frac{\partial B(n+1)}{\partial z}+\frac{\partial B(n-1)}{\partial z}\Big)+\frac{1}{2}h^2\left(\frac{1}{h}\frac{\mathrm{d}p^{(0)}}{\mathrm{d}z}-\frac{\mathrm{d}h/\mathrm{d}z}{h^2}\right)\Big(-B'(n+1)+B'(n-1)\Big)\\ &+\frac{h}{2}\left(\frac{\mathrm{d}p^{(0)}}{\mathrm{d}z}\right)\Big(B(n+1)+B(n-1)\Big)-\frac{1}{2}\Big(B(n+1)A(n-1)+B'(n+1)A^\wedge(n-1)\Big)\\ &-\Big(B'(n+1)A(n+1)+B'(n-1)A(n-1)\Big)+\frac{1}{2}\Big(B(n-1)A(n+1)+B'(n-1)A^\wedge(n+1)\Big).\end{aligned} \tag{A.17}$$

This equation can be extensively simplified on the surface utilising the periodicity of functions A and B, using equations (3.19) and (3.48), to obtain

$$\begin{aligned}\frac{\partial B(n+1,z)}{\partial z}-\frac{\mathrm{d}h/\mathrm{d}z}{h^2}A(n+1,z)-\left(\frac{1}{2}\frac{\mathrm{d}p^{(0)}}{\mathrm{d}z}-\frac{\mathrm{d}h/\mathrm{d}z}{h}\right)B(n+1,z)&\\ +\frac{1}{h}B'(n+1,z)A(n+1,z)=-\frac{1}{h}(N(n+1,z)-N(n-1,z))\,.&\end{aligned} \tag{A.18}$$

As argued following (A.7), we need only require that N be bounded in n, and hence that the right-hand side of (A.18) is zero. The resultant expression is the quoted equation (3.51) in Section 3.2.2.2.

Appendix A4 Rearranging the second order velocities to get an advection equation

It is more convenient to numerically solve equation (3.52) if the excitation term on the right-hand side can be included inside the derivatives. Moreover, if the advection speed is the same as Burger's equation for the stresses (3.28b), both equations share the same characteristics, again aiding numerical solution. This is the aim of the rearrangement detailed here.

We start transforming equation (3.52) by multiplying it by h^2/α_1, giving

$$\frac{h^2}{\alpha_1}\frac{\partial}{\partial z}\Big(\frac{B}{(\alpha_2/h)}\Big)+\omega\frac{\partial}{\partial\xi}\Big(\frac{B}{(\alpha_2/h)}\Big)-\frac{\mathrm{d}h/\mathrm{d}z}{\alpha_2}\omega=0, \tag{A.19}$$

where ω is as was defined for the stresses and is given by (A.13). To remove the excitation term, we look at the multiple of ω which solves equation (A.19). Calling this factor $Q(z)$, in this case we can write

$$\frac{h^2}{\alpha_1}\frac{\partial}{\partial z}\Big(Q\omega\Big) + \omega\frac{\partial}{\partial \xi}\Big(Q\omega\Big) - \frac{\omega}{\alpha_2}\frac{\mathrm{d}h}{\mathrm{d}z} \;=\; \frac{h^2}{\alpha_1}\omega\frac{dQ}{dz} + Q\left[\frac{h^2}{\alpha_1}\frac{\partial \omega}{\partial z} + \frac{1}{2}\frac{\partial}{\partial \xi}\Big(\omega^2\Big)\right] - \frac{\omega}{\alpha_2}\frac{\mathrm{d}h}{\mathrm{d}z} \;=\; 0. \tag{A.20}$$

The term in the bracket is zero since ω satisfies Burger's equation (A.13). The remaining terms find $Q(z)$ as

$$\frac{h^2}{\alpha_1(z)}\frac{dQ}{dz} = \frac{\mathrm{d}h/\mathrm{d}z}{\alpha_2(z)} \qquad \Rightarrow \qquad Q(z) = \int^z \frac{\alpha_1(\bar{z})}{\alpha_2(\bar{z})}\frac{\mathrm{d}h(\bar{z})/\mathrm{d}(\bar{z})}{h(\bar{z})^2}d\bar{z}. \tag{A.21}$$

Subtracting (A.20) from (A.19) results in

$$\frac{h^2}{\alpha_1}\frac{\partial}{\partial z}\Big(\frac{B(\xi,z)}{(\alpha_2/h)} - Q(z)\omega(\xi,z)\Big) + \omega(\xi,z)\frac{\partial}{\partial \xi}\Big(\frac{B(\xi,z)}{(\alpha_2/h)} - Q(z)\omega(\xi,z)\Big) = 0. \tag{A.22}$$

With the same change of domain $z \mapsto T$ as (A.13), we finally have,

$$\frac{\partial}{\partial T}\Big(\frac{B}{(\alpha_2/h)} - Q\omega\Big) + \omega\frac{\partial}{\partial \xi}\Big(\frac{B}{(\alpha_2/h)} - Q\omega\Big) = 0, \tag{A.23}$$

which is the expression given in equation (3.53).

Bibliography

Al-Salehi, Firbank, and Lancaster (1973). “An experimental determination of the roll pressure distributions in cold rolling”. *International Journal of Mechanical Sciences*, **15**(9) 693–710. doi: 10.1016/0020-7403(73)90049-0.

Alexander (1955). “A slip line field for the hot rolling process”. *Proceedings of the Institution of Mechanical Engineers*, **169**(1) 1021–1030. doi: 10.1243/PIME˙PROC˙1955˙169˙103˙02.

Alexander (1972). “On the theory of rolling”. *Proceedings of the Royal Society of London. A. Mathematical and Physical Sciences*, **326**(1567) 535–563. doi: 10.1098/rspa.1972.0025.

Allwood, Cullen, Carruth, Cooper, McBrien, Milford, Moynihan, and Patel (2012). *Sustainable materials: with both eyes open*, volume 2012. UIT Cambridge Limited Cambridge, UK.

Allwood, Duncan, Cao, Groche, Hirt, Kinsey, Kuboki, Liewald, Sterzing, and Tekkaya (2016). “Closed-loop control of product properties in metal forming”. *CIRP Annals*, **65**(2) 573–596. doi: 10.1016/j.cirp.2016.06.002.

Beyer, Hauer, and Willner (2015). “Development of a constitutive friction law based on the frictional interaction of rough surfaces”. *Tribology in Industry*, **37**(4) 400.

Bland and Ford (1948). “The calculation of roll force and torque in cold strip rolling with tensions”. *Proceedings of the Institution of Mechanical Engineers*, **159**(1) 144–163. doi: 10.1243/PIME“˙PROC“˙1948“˙159“˙015“˙02.

Brambley and Peake (2008). “Sound transmission in strongly curved slowly varying cylindrical ducts with flow”. *J. Fluid Mech.*, **596** 387–412. doi: 10.1017/S0022112007009603.

Carlsson (1998). “The contact pressure distribution in flat rolling of wire”. *Journal of Materials Processing Technology*, **73**(1-3) 1–6. doi: 10.1016/S0924-0136(97)00091-5.

Cawthorn, Minton, and Brambley (2016). “Asymptotic analysis of cold sandwich rolling”. *Int. J. Mech. Sci.*, **106** 184–193. doi: 10.1016/j.ijmecsci.2015.12.012.

Cherukuri, Johnson, and Smelser (1997). “A rate-dependent model for hot-rolling”. *International journal of mechanical sciences*, **39**(6) 705–727. doi: 10.1016/S0020-7403(97)81242-8.

Chitkara and Johnson (1966). “Some experimental results concerning spread in the rolling of lead”. *Journal of Basic Engineering*, **88**(2) 489–499. doi: doi.org/10.1115/1.3645884.

Collins (1969). “Slipline field solutions for compression and rolling with slipping friction”. *International Journal of Mechanical Sciences*, **11**(12) 971–978. doi: 10.1016/0020-7403(69)90009-5.

Domanti and McElwain (1995). “Two-dimensional plane strain rolling: an asymptotic approach to the estimation of inhomogeneous effects”. *International journal of mechanical sciences*, **37**(2) 175–196. doi: 10.1016/0020-7403(94)00053-M.

Dunne and Petrinic (2005). *Introduction to computational plasticity*. OUP Oxford. ISBN 0198568266.

El-Nikhaily (1979). “Metal flow models for shape rolling”. *Doctoral Dissertation, Technical University of Aachen*.

Erfanian, Brambley, Flanagan, O’Kiely, and O’Connor (2023). “New models for cold rolling: Generalized slab theory and slip lines for fast predictions without finite elements”. In *International Conference on the Technology of Plasticity*, pages 223–233. doi: 10.1007/978-3-031-41023-9˙23.

Erfanian, Brambley, Flanagan, O’Connor, and O’Kiely (2025a). “Through-thickness modelling of metal rolling using multiple-scale asymptotics”. submitted to Eur. J. Mech. A/Solids. doi: 10.48550/arXiv.2408.01347.

Erfanian, Brambley, and Slater (2025b). “Mathematical modelling of wire flat rolling process”. In-preparation.

Erfanian, Slater, and Brambley (2025c). “Modelling lateral spread in wire flat rolling”. doi: 10.48550/arXiv.2504.06300.

Firbank and Lancaster (1965). “A suggested slip-line field for cold rolling with slipping friction”. *International Journal of Mechanical Sciences*, **7**(12) 847–852. doi: 10.1016/0020-7403(65)90037-8.

Flanagan, O’Connor, Erfanian, Music, Brambley, and O’Kiely (2024). “Careful finite element simulations of cold rolling with accurate through-thickness resolution and prediction of residual stress”. submitted to Eur. J. Mech. A/Solids. doi: 10.48550/arXiv.2408.03242.

Fleck, Johnson, Mear, and Zhang (1992). “Cold rolling of foil”. *Proceedings of the Institution of Mechanical Engineers, Part B: Journal of Engineering Manufacture*, **206**(2) 119–131. doi: 10.1243/PIME˙PROC˙1992˙206˙06.

Group and Sparling (1961). “Formula for ‘spread’in hot flat rolling”. *Proceedings of the Institution of Mechanical Engineers*, **175**(1) 604–640.

Hill (1948). “A theory of the yielding and plastic flow of anisotropic metals”. *Proceedings of the Royal Society of London. Series A. Mathematical and Physical Sciences*, **193**(1033) 281–297. doi: A theory of the yielding and plastic flow of anisotropic metals.

Hill (1998). *The mathematical theory of plasticity*, volume 11. Oxford university press. ISBN 0198503679.

Hinch (1991). *Perturbation Methods*, chapter 7, pages 116–143. Cambridge. doi: 10.1017/CBO9781139172189.

Howell, Kozyreff, and Ockendon (2008). *Applied Solid Mechanics*. Cambridge Texts in Applied Mathematics. Cambridge University Press. ISBN 9780521671095.

Idzik, Krämer, Hirt, and Lohmar (2024). “Coupling of an analytical rolling model and reinforcement learning to design pass schedules: towards properties controlled hot rolling”. *Journal of Intelligent Manufacturing*, **35**(4) 1469–1490. doi: 10.1007/s10845-023-02115-2.

Johnson (1987). “Conical extrusion of a work-hardening material: an asymptotic analysis”. *Journal of engineering mathematics*, **21**(4) 295–329. doi: 10.1007/BF00132681.

Johnson (1991). “Shape forming and lateral spread in sheet rolling”. *International journal of mechanical sciences*, **33**(6) 449–469. doi: 10.1016/0020-7403(91)90081-D.

Johnson and Smelser (1992). “An asymptotic formulation of shear effects in two dimensional rolling”. *Journal of Materials Processing Technology*, **34**(1-4) 311–318. doi: 10.1016/0924-0136(92)90122-9.

Johnson, Sowerby, and Venter (2013). *Plane-strain slip-line fields for metal-deformation processes: a source book and bibliography*. Elsevier. ISBN 0080254527.

Kazeminezhad and Taheri (2005). “A theoretical and experimental investigation on wire flat rolling process using deformation pattern”. *Materials & design*, **26**(2) 99–103. doi: 10.1016/j.matdes.2004.06.010.

Kazeminezhad and Taheri (2006). “Calculation of the rolling pressure distribution and force in wire flat rolling process”. *Journal of Materials Processing Technology*, **171** (2) 253–258. doi: 10.1016/j.jmatprotec.2005.06.070.

Kazeminezhad, Taheri, and Tieu (2008). “A study on the cross-sectional profile of flat rolled wire”. *Journal of materials processing technology*, **200**(1-3) 325–330. doi: 10.1016/j.jmatprotec.2007.09.029.

Kennedy (08 1987). “A Method for Analyzing Spread, Elongation and Bulge in Flat Rolling”. *Journal of Engineering for Industry*, **109**(3) 248–256. doi: 10.1115/1.3187126.

Kobayashi (1978). “Influence of rolling conditions on spreading in flat rolling of round wire”. *Journal of the Japan Society for Technology of Plasticity*.

Kumar, Rath, and Kumar (2021). “Simulation of plate rolling process using finite element method”. *Materials Today: Proceedings*, **42** 650–659. doi: 10.1016/j.matpr.2020.11.050.

Lahoti and Kobayashi (1974). “On hill’s general method of analysis for metal-working processes”. *International Journal of Mechanical Sciences*, **16**(8) 521–540. doi: 10.1016/0020-7403(74)90018-6.

Lenard (2013). *Primer on flat rolling*. Newnes. ISBN 9780080994185.

Liu, Hartley, Sturgess, and Rowe (1985). “Elastic-plastic finite-element modelling of cold rolling of strip”. *International journal of mechanical sciences*, **27**(7-8) 531–541. doi: 10.1016/0020-7403(85)90043-8.

MacGregor and Palme (1959). “The distribution of contact pressures in the rolling of metals”. *Journal of Basic Engineering*, **81**(4) 669–679.

MathWorks Inc. (2024). *MATLAB version: 24.1.0.2568132 (R2024a) Update 1*. https://www.mathworks.com.

McCrum (1956). “Progress report on the experimental investigation of spread, load, and torque in hot flat rolling”. Technical Report 10/56, BISRA Report MW/AL, Report.

Minton (2017). *Mathematical modelling of asymmetrical metal rolling processes*. PhD thesis, Apollo - University of Cambridge Repository. doi: 10.17863/CAM.17210.

Minton, Cawthorn, and Brambley (2016). “Asymptotic analysis of asymmetric thin sheet rolling”. *Int. J. Mech. Sci.*, **113** 36–48. doi: 10.1016/j.ijmecsci.2016.03.024.

Montmitonnet (2006). “Hot and cold strip rolling processes”. *Computer methods in applied mechanics and engineering*, **195**(48-49) 6604–6625. doi: 10.1016/j.cma.2005.10.014.

Oh and Kobayashi (1975). “An approximate method for a three-dimensional analysis of rolling”. *International Journal of Mechanical Sciences*, **17**(4) 293–305.

Olaogun, Edberg, Lindgren, Oluwole, and Akinlabi (2019). “Heat transfer in cold rolling process of AA8015 alloy: a case study of 2-D FE simulation of coupled thermo-mechanical modeling”. *The International Journal of Advanced Manufacturing Technology*, **100** 2617–2627. doi: 10.1007/s00170-018-2811-2.

Orowan (1943). “The calculation of roll pressure in hot and cold flat rolling”. *Proc. Inst. Mech. Eng.*, **150**(1) 140–167. doi: 10.1243/PIME˙PROC˙1943˙150˙025˙02.

Pennestrì, Rossi, Salvini, and Valentini (2016). “Review and comparison of dry friction force models”. *Nonlinear dynamics*, **83** 1785–1801. doi: 10.1007/s11071-015-2485-3.

Pesin, Salganik, Trahtengertz, Cherniahovsky, and Rudakov (2002). “Mathematical modelling of the stress–strain state in asymmetric flattening of metal band”. *Journal of Materials Processing Technology*, **125** 689–694. doi: 10.1016/S0924-0136(02)00353-9.

Prabhu, Kulkarni, and Sharma (2020). “Multi-response optimization of the turn-assisted deep cold rolling process parameters for enhanced surface characteristics and residual stress of aisi 4140 steel shafts”. *Journal of Materials Research and Technology*, **9**(5) 11402–11423. doi: 10.1016/j.jmrt.2020.08.025.

Prakash, Dixit, and Lal (1995). “Steady-state plane-strain cold rolling of a strain-hardening material”. *Journal of materials processing technology*, **52**(2-4) 338–358. doi: 10.1016/0924-0136(94)01728-J.

Roberts (1993). “The invariant manifold of beam deformations”. *J. Elasticity*, **30** 1–54. doi: 10.1007/BF00041769.

Roberts (2015). *Model Emergent Dynamics in Complex Systems.* SIAM. doi: 10.1137/1.9781611973563. ISBN 9781611973556.

S Metals.co (2024). “Cold rolled vs hot rolled steel”. https://www.smetals.co.uk/cold-rolled-vs-hot-rolled-steel/. Accessed: 2024-11-17.

Semiatin and Jonas (1984). *Formability and workability of metals: plastic instability and flow localization.* ASM. ISBN 0871701839.

Sims (1954). “The calculation of roll force and torque in hot rolling mills”. *Proceedings of the Institution of Mechanical Engineers*, **168**(1) 191–200. doi: 10.1243/PIME˙PROC˙1954˙168˙023˙02.

Smet and Johnson (1989). “An asymptotic analysis of cold sheet rolling”. *Journal of Applied Mechanics*. doi: 10.1115/1.3176062.

Spittel and Spittel (2009). “Steel symbol/number: DC04/1.0338”. In *Metal Forming Data of Ferrous Alloys — Deformation Behaviour*, pages 162–167. Springer-Verlag. doi: 10.1007/978-3-540-44760-3˙18.

Tarnovskii, Pozdeyev, and Lyashkov (2013). *Deformation of metals during rolling*. Elsevier.

TATA Steel (2024). “Mills”. https://consulting.tatasteel.com/our_expertise/mills/. Accessed: 2024-11-17.

Thakur, Das, and Jha (2022). “Effect of warm rolling process parameters on microstructure and mechanical properties of structural steels”. *Transactions of the Indian Institute of Metals*, **75**(6) 1509–1524. doi: 10.1007/s12666-021-02519-9.

Trzepiecinski and Lemu (2017). “Effect of computational parameters on springback prediction by numerical simulation”. *Metals*, **7**(9) 380. doi: 10.3390/met7090380.

Utsunomiya, Hartley, and Pillinger (2001). “Three-dimensional elastic-plastic finite-element analysis of the flattening of wire between plain rolls”. *J. Manuf. Sci. Eng.*, **123**(3) 397–404. doi: 10.1115/1.1365158.

Valéry Roy, Roberts, and Simpson (2002). “A lubrication model of coating flows over a curved substrate in space”. *J. Fluid Mech.*, **454**. doi: 10.1017/S0022112001007133.

Vallellano, Cabanillas, and Garcia-Lomas (2008). “Analysis of deformations and stresses in flat rolling of wire”. *Journal of materials processing technology*, **195**(1-3) 63–71. doi: 10.1016/j.jmatprotec.2007.04.124.

Wojtyra (2017). “Modeling of static friction in closed-loop kinematic chains—uniqueness and parametric sensitivity problems”. *Multibody System Dynamics*, **39**(4) 337–361. doi: 10.1007/s11044-016-9535-6.

World Steel Association et al. (2020). “World crude steel production—summary”. *World Steel Association: Brussels, Belgium*.

Wusatowski (1969). *Fundamentals of Rolling*. Pergamon Press. ISBN 9780080122762; 0080122760.

Yarita, Mallett, and Lee (1985). “Stress and deformation analysis of plane-strain rolling process”. *Steel Research*, **56**(5) 255–259. doi: doi.org/10.1002/srin.198500631.

Zhang and Ou (2016). “Relationship between friction parameters in a coulomb–tresca friction model for bulk metal forming”. *Tribology International*, **95** 13–18. doi: 10.1016/j.triboint.2015.10.030.